

# Single Molecule Mass Photometry of DNA and DNA-Protein Interactions



Yiwen Li  
St Cross College  
University of Oxford

A thesis submitted for the degree of  
*Doctor of Philosophy in Theoretical and Physical Chemistry*

11<sup>th</sup> March, 2022



## Acknowledgements

My journey of conducting the DPhil study during the past 4.5 years was not all plain sailing. I have been through terrible health conditions, being alone during COVID-19 lockdown, hundreds of failures in experiments, one rejection for publication, etc., which have together helped me build up a strong mind as well as a good immune system to face and overcome challenges and illness. First of all, I would like to acknowledge the generous financial support from CSC Scholarship Council to bring me here to this amazing university and research group.

Countless people have supported my efforts on this work. I would like to first thank my supervisors, Professor Philipp Kukura and Professor Grant Ritchie, for their invaluable and continued guidance and the endless supply of fascinating projects. Their immense knowledge and plentiful experience have encouraged me in all the time of my academic research and daily life. The Kukura Group with all the amazing people has been such a friendly, cooperative working environment, helping me tackle down almost all the difficulties I met with during this work. In particular, I gratefully recognise the help of Manish Kushwah and Gavin Young, who have guided me through all the biological and technical parts of this work. Special thanks to Steve Thorpe and Shawn Meng for building such a powerful TIRFM, and Sam Tusk for his input into the analysis. I also enjoy the pleasure of working with Eric Foley on the project related to surface passivation, as well as my DNA project colleague, Roi Asor, on investigating various DNA-protein interactions.

Lots of the work presented in this thesis would never be able to proceed

---

without the samples and ideas provided by several collaborators. The ZIF-8/L and DNA origami samples provided by Hamish Yeung and Florian Selbach have initiated new directions for exploring MP applications. I would also like to thank David Drechsel and Jan-Michael Peters from the Research Institute of Molecular Pathology in Vienna for their inputs in the cohesin project. Additionally, a special thank should be sent to Weston Struwe, for his help in assembling the *NAR* paper.

With the love, companionship and mental support from the special people and dearest friends, I have been enjoying the fantastic moments while capable of surviving the difficult days during my DPhil. First, I would like to send my special congratulations to Yu Zhou and her newborn little prince, Yu Jiang. The 12-year friendship since I met Yu, Xiaou, and Siyao on the first day of high school has delighted me every moment. Nothing of the physical binds us together, but for the chord of love, acceptance and mutual understandings which have kept us going. I also want to thank Kaori, Nan, Jingyi and Shu for sharing the unforgettable sweet memories during my undergraduate study. Further, my warm and heartfelt thanks go to the wonderful people I met in Oxford, with whom I have celebrated special occasions, travelled around Europe, and tasted delicious food from all over the world. I am so fortunate to meet the most nurturing person - Hang, my best sisters - Yaqiong, Zhen and Shiyan, my favourite girls - An and Noe, as well as the hotpot/TML gang - Tyuki, Martin, Jun, Ken, Masato and Fuga.

Last but not least, I would like to thank my parents, Jun Li and Lilan Gao, for their patience, unconditional support and encouragement over the years.

## **Statement of Originality**

The research described in this thesis was carried out by the author between October 2017 and March 2022 and includes nothing which is the outcome of work done in collaboration, except where specifically indicated in the text. The use of the first person plural is strictly a matter of style in keeping with standard scientific convention.



## List of Publications

The work carried out by the author between October 2017 and March 2022 led to the following publications:

1. **Y. Li**, W.B. Struwe, P. Kukura, Single molecule mass photometry of nucleic acids, *Nucleic Acids Research*, 2020, **48**, e97.
2. **Y. Li**, R. Asor, D. Drechsel, J.M. Peters, P. Kukura, ATP drives loop extrusion by modulating the affinity of cohesin to DNA, in preparation.



## Abstract

Mass photometry (MP) based on interferometric scattering microscopy (iSCAT) is a novel, label-free imaging and quantification approach, which allows for the accurate mass measurement of biomolecules as well as the quantification of protein-protein interactions in solution. In this work, we show that this approach is equally applicable to DNA and DNA-protein interactions.

After illustrating iSCAT's ability to visualise the crystallisation events of non-biological systems, including alkali-metal halides and metal-organic frameworks, we switch to demonstrating the capability of MP to directly measure relative concentrations by molecular counting in complex DNA mixtures. Using a dsDNA ladder, we find a linear relationship between the number of bases per molecule and the associated imaging contrast for up to 1200 bp, enabling us to quantify dsDNA length with up to 2 bp accuracy.

We then present an experimental assay to measure the key interactions responsible for the cohesin assembly, its interactions with DNA, and their modulations by ATPase cycle, providing new insights into studying complex biomolecular assemblies and interactions with the multimeric nature.

Lastly, we introduce surface passivation to control the binding density of biomolecules to cope with increasing measurement complexity, introducing a path to detect low-abundance biomolecules of interest without a pre-purification step, also with the potential to measure low-affinity interactions.

These results together highlight mass photometry as a label-free, rapid, and accurate single molecule method complementary to existing techniques for characterising and quantifying DNA and DNA-protein interactions.



# Contents

<b>List of Abbreviations</b>	<b>v</b>
<b>1 Introduction</b>	<b>1</b>
<b>2 Theoretical Background</b>	<b>5</b>
2.1 Introduction . . . . .	5
2.2 Fluorescence Microscopy . . . . .	6
2.3 Scattering Microscopy . . . . .	10
2.3.1 Dark-Field Microscopy . . . . .	11
2.3.2 Interferometric Scattering Microscopy . . . . .	13
2.3.3 Contrast Enhanced iSCAT via Numerical Aperture Filtering . . . . .	17
2.4 Mass Photometry . . . . .	21
2.4.1 Protein Mass Determination . . . . .	21
2.4.2 Recent Applications . . . . .	21
<b>3 Visualising Nucleation by Interferometric Scattering Microscopy</b>	<b>25</b>
3.1 Introduction . . . . .	25
3.2 Materials and Methods . . . . .	29
3.3 Results and Discussion . . . . .	31
3.3.1 Characterisation of the iSCAT Microscope . . . . .	31
3.3.2 Nucleation in Supersaturated Solution . . . . .	33

3.3.3	Crystallisation of (ZIF)-8 and (ZIF)-L . . . . .	34
3.4	Conclusion and Outlook . . . . .	36
<b>4</b>	<b>Single Molecule Mass Photometry of dsDNA and ssDNA</b>	<b>41</b>
4.1	Introduction . . . . .	41
4.2	Materials and Methods . . . . .	43
4.3	Results and Discussion . . . . .	51
4.3.1	Quantifying DNA Contour Length . . . . .	51
4.3.2	Resolution and Relative Concentration Measurements . . . . .	54
4.3.3	Characterization of Nucleotide Accuracy and Precision . . . . .	57
4.3.4	MP Contrast vs. DNA Shape . . . . .	61
4.4	Conclusion and Outlook . . . . .	62
<b>5</b>	<b>ATP Drives Loop Extrusion by Modulating the Affinity of Cohesin to DNA</b>	<b>67</b>
5.1	Introduction . . . . .	67
5.2	Materials and Methods . . . . .	76
5.3	Results and Discussion . . . . .	81
5.3.1	Intra-subunit Interactions and Pentamer Assembly . . . . .	81
5.3.2	DNA Interactions With 3 Subunits: STAG1, NIPBL, Cohesin Trimer . . . . .	83
5.3.3	DNA Interactions with Sub-assemblies and Full Assembly . . . . .	84
5.3.4	Modulation of all DNA-Protein Interactions by ATP . . . . .	86
5.3.5	ATP Drives Loop Extrusion by Modulating the DNA Affinities of STAG1-Cohesin and NIPBL-Cohesin . . . . .	88
5.4	Conclusion and Outlook . . . . .	91
<b>6</b>	<b>Surface Passivation for Mass Photometry</b>	<b>93</b>
6.1	Introduction . . . . .	93

6.2	Materials and Methods . . . . .	99
6.3	Results and Discussion . . . . .	103
6.3.1	PEG Passivation of Glass Coverslips . . . . .	103
6.3.2	Binding to 30% PEG-NTA Surfaces . . . . .	104
6.3.3	Robust Binding of Streptavidin to 10% Biotin-PEG Sur- faces . . . . .	106
6.3.4	Specific Binding by PEG-biotin-Streptavidin- <sup>BT</sup> tris-NTA	109
6.4	Conclusion and Outlook . . . . .	111
<b>7</b>	<b>Summary and Outlook</b>	<b>113</b>
7.1	Summary . . . . .	113
7.2	Outlook . . . . .	114
	<b>References</b>	<b>117</b>

## Contents

---

# List of Abbreviations

AFM	Atomic Force Microscopy
APTES	(3-Aminopropyl)triethoxysilane
ATP	Adenosine Triphosphate
ATPase	Adenosine Triphosphatase
bp	Base Pairs
BSA	Bovine Serum Albumin
CMOS	Complementary Metal Oxide Semiconductor
cryo-EM	Cryogenic Electron Microscopy
DNA	Deoxyribonucleic acid
dsDNA	Double-stranded DNA
EDTA	Ethylenediaminetetraacetic acid
EM	Electron Microscopy
FOV	Field of View
iSCAT	Interferometric Scattering Microscopy
MOF	Metal-Organic Framework
MP	Mass Photometry
NHS	N-Hydroxysuccinimide
nt	Nucleotides
NTA	Nitrilotriacetic acid
PEG	Polyethylene Glycol
PSF	Point Spread Function
SMC	Structural Maintenance of Chromosomes
SNR	Singal-to-Noise Ratio

## List of Abbreviations

---

ssDNA	Single-stranded DNA
SVA	Succinimidyl-Valerate
TAD	Topologically Associating Domain
TIRFM	Total Internal Reflection Fluorescence Microscopy
Tris	Tris(hydroxymethyl)aminomethane
tris-NTA	trisnitrilotriacetic acid

# Chapter 1

## Introduction

Single molecule methods play an ever more important role in nucleic acid science. From an optical perspective, these have exclusively been associated with fluorescence-based methods due to the superior background rejection capability of fluorescence microscopy.<sup>1,2</sup> Despite the associated strengths, however, such an approach requires fluorescence labelling, and makes quantitative measurements fairly labour intensive as one needs to account for photophysical properties of the fluorophores.

Light scattering on the other hand is an intrinsic property of matter and exhibits a linear scaling with the mass of material when detected in an interferometric fashion. It has been recently demonstrated that ultrasensitive interferometric scattering detection cannot only be used to detect and count individual proteins in solution, but that the associated signal scales linearly with the molecular mass of the detected object, giving rise to a third way of measuring mass, which is called mass photometry (MP).<sup>3</sup> Moreover, mass photometry's ability to count individual molecules can be used to quantify the relative abundances of different biomolecular complexes in solution, providing the mean to quantitatively measure the associated binding affinities and interaction kinetics of complex formation.<sup>4,5</sup>

Despite the wide applicability of MP to study proteins, protein-lipid com-

---

plexes, and glycoproteins,<sup>3</sup> its suitability to study DNA and DNA-protein complexes remains to be tested. The work presented in this thesis builds on the capabilities of an interferometric scattering (iSCAT) microscope to visualise the assemblies of non-biological systems, and expands MP to DNA as well as DNA-protein interactions in solution. This work explores further improvements on the methodology itself by employing surface passivation to obtain mass photometry measurements with controlled binding and unbinding of biomolecules. To achieve these goals, this work covers from inorganic compounds to biomolecules, and the use of iSCAT and MP to answer fundamental questions about their inner workings.

*chapter 2* details the theoretical background of scattering microscopy, with a focus on the advantages over fluorescence microscopy. This chapter continues to discuss the advantages of iSCAT over dark-field and recent technical improvements based on contrast enhancement via numerical aperture filtering. Grounded in the introduction of how an iSCAT microscope can be used for a mass photometry experiment, we include a brief summary of recent MP applications in characterising assemblies and molecular interactions of a variety of biomolecules.

*chapter 3* details the construction of a customised interferometric scattering (iSCAT) microscope and the characterisation of its performance by studying gold nanoparticles, and GroEL proteins as small scattering signals. By observing the crystallisation events of alkali-metal halides and metal-organic frameworks, the capabilities of the iSCAT microscope to detect small movements have been shown, demonstrating the potential of this technique to investigate the kinetics of non-biological systems beyond biomolecules.

*chapter 4* demonstrates the label-free, all-optical detection of ssDNA and dsDNA using mass photometry. By using a prototype mass photometer,

---

we show that mass photometry provides direct information on absolute and relative concentration by molecular counting, as well as demonstrate its ability to determine the number of basepairs/nucleotides of dsDNA/ssDNA with few basepair/nucleotide accuracy. Investigating contrast variations of two DNA origamis of the same mass helps to evaluate MP contrast sensitivity to the structure of biomolecules.

*chapter 5* sets an example of how MP can be used to study biomolecular assemblies as well as DNA-protein interactions. Loop extrusion by cohesin has emerged as a critical pathway for how chromosomes are shaped. Quantifying the key interactions responsible for cohesin assembly, DNA binding, and their modulation by ATP binding and ATPase cycle provides new insight into the mechanism for loop extrusion by cohesin.

*chapter 6* explores the use of surface passivation for mass photometry to control the binding and unbinding of biomolecules to a surface. Mass photometry and total internal fluorescence microscopy (TIRFM) are used to explore different conjugation strategies, including PEG-NTA, PEG-biotin, PEG-biotin-Streptavidin-<sup>BT</sup>tris-NTA, demonstrating the potential and shortcoming of adopting surface passivation to MP.

Finally, *chapter 7* provides a short summary of the contents discussed in this thesis and concludes with an outlook.



# Chapter 2

## Theoretical Background

### 2.1 Introduction

The ability to detect single molecules of DNA and proteins has revolutionised the understanding of how DNA interacts with proteins in fundamental biomolecular processes.<sup>6-9</sup> While bulk studies provide insight into many biomolecular properties, certain characteristics and processes cannot be uncovered by characterising an average biomolecule behaving in a generic manner. In contrast to traditional averaging bulk measurements, single molecule techniques have the advantages of revealing heterogeneous behaviors as well as enabling studies of dynamics in real time. Single molecule methods are particularly important for understanding the biological processes which are carried out by one or a few proteins, such as DNA replication, transcription and recombination.

There are a range of approaches for studying DNA as well as DNA-protein interactions at the single molecule level, such as mass spectrometry, atomic force microscopy and optical tweezers.<sup>10-12</sup> From an optical perspective, a large and growing body of these methods are mostly connected with fluorescence-based methods, because of its high sensitivity. However, one major drawback of this kind of approach is the requirement for fluorescence labelling, which makes quantitative measurements labour intensive due to photo-bleaching and photo-blinking. Such measurements require independent tests of the

stability, functionality of the labelled biomolecules.<sup>13,14</sup> Therefore, label-free detection and quantification would be highly desirable to minimise experimental complexity and potential perturbations.

Label-free detection of single proteins based on interferometric scattering microscopy has been first reported in 2014<sup>15,16</sup> in the context of increasing sensitivity.<sup>17,18</sup> Further improvements to the detection methodology of iSCAT,<sup>19</sup> recently lead to the development of mass photometry (MP), originally introduced as interferometric scattering mass spectrometry (iSCAMS),<sup>3</sup> which enables not only label-free detection and imaging of single molecules, but critically their quantification through mass measurement with high levels of accuracy, precision and resolution. Another important feature of MP is the capability to measure the distributions of biomolecules in bulk solution, from which one can extract binding affinities, kinetics and stoichiometries.<sup>4</sup> These advantages together vote MP in principle a powerful tool to study single DNA molecules and their interactions with proteins.

In this chapter, we present a brief introduction on fluorescence microscopy as the tool for studying biological samples. We then focus on the theoretical background of mass photometry based on interferometric scattering microscopy, with an overview of recent MP applications in biological studies.

## 2.2 Fluorescence Microscopy

Fluorescence is a form of luminescence that is caused by the emission of an electromagnetic radiation.<sup>20</sup> The absorption of a photon excites a molecule from its ground state to a higher energy (high frequency, low stability) state, followed by the emission of the radiation.<sup>21</sup> Different fluorescence detection techniques, such as fluorescence spectroscopy, fluorescence intensity, fluorescence depolarisation, fluorescence resonance energy transfer and fluorescence corre-

lation spectroscopy, are based on this fundamental principle and its relevant modifications.

In traditional epifluorescence microscopy, illumination light is focused through the objective, exciting fluorescent molecules in the sample<sup>22-25</sup> (Figure 2.1A). The photons emitted as a result of this process are collected by the same objective and focused onto a camera for detection. This exposes the sample to both excessive and out-of-focus light, increasing the effective light dose to the imaged sample. Light itself and the radicals released during the fluorescence process are toxic to cells and contribute to sample degradation. Moreover, fluorescence outside the focal plane adds to image noise, reducing total signal to noise and spatial resolution.

Total internal reflection fluorescence (TIRF) microscopy improves both total signal-to-noise ratio (SNR) and spatial resolution through differences in the way illumination occurs (Figure 2.1C).<sup>26</sup> When light traveling through a medium hits another medium with a different refractive index, some of the light will be reflected and some will be refracted. The relative proportions depend on the differences in, amongst other things, the incident angle. If the light is traveling from a relatively high refractive index into a lower refractive index ( $n_1 > n_2$ ), there will be a critical angle  $\theta_c$  beyond which all the light is reflected. When light hits an interface beyond this critical angle ( $\theta_1 > \theta_c$ ), it is completely reflected, which is called Total Internal Reflection (TIR). The excitation laser in TIRF microscopy is presented beyond this critical angle such that it completely reflects off the glass slide.<sup>27</sup> As a result, all light is reflected, and no light penetrates into the sample.

However, within the area where light is reflected, an evanescent wave forms on the other side of the slide, resulting in very shallow illumination of the sample (Figure 2.1B). Because the evanescent wave oscillates with the same

## 2.2. Fluorescence Microscopy

frequency of the reflected light, it still excites any fluorescent molecules within this small area. The area of the evanescent wave is defined by the optics used, although normally a  $\sim 100$  nm optical section is created at the surface.

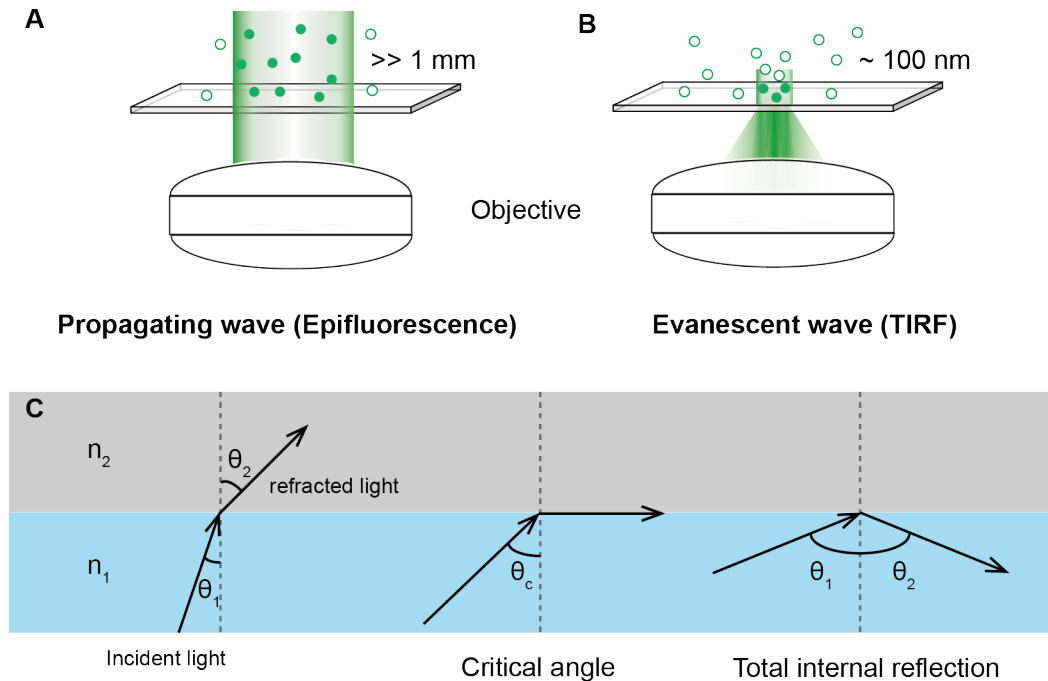


**Figure 2.1:** (A), (B) Difference in illumination from a propagating wave and an evanescent wave. Propagating waves, such as those generated from standard epifluorescence illumination, propagate in a linear manner through the sample and can excite fluorophores  $> 1$  mm in depth. TIRF generates evanescent waves that decay exponentially and only penetrate to  $\sim 100$  nm. (C) Principle of total internal reflection.

The advantage of TIRF for single-molecule fluorescence is that no out-of-focus light is collected, leaving only the fluorescence emission from the volume of the evanescent wave. The SNR is thereby significantly enhanced. TIRF is thus particularly beneficial for studying areas of the sample that are close to the surface, such as molecules immobilised on a coverslip or on the cell membrane. In single-molecule fluorescence microscopy, TIRF is one of the most commonly used imaging techniques for applications such as investigating DNA replication, transcription, and DNA damage repair.<sup>28-30</sup>

TIRF has been used in combination with Fluorescence Resonance Energy Transfer (FRET) for imaging between fluorophores as they interact.<sup>31</sup> Proposed by Theodor Förster in 1960 and confirmed experimentally by Stryer and Haugland in 1967, FRET takes advantage of the principle of non-radiative energy transfer between a donor and acceptor molecule to determine the proximity of the two molecules.<sup>32,33</sup> FRET produces information about fluorophore proximity in the order of 2 - 10nm resolution.<sup>34</sup> This can happen between different molecules within a complex, or between different domains of single molecules. It is often perceived as the shift in relative fluorescence of, or between, the donor and the acceptor. As such, it is highly susceptible to noise and benefits substantially from TIRF's improved SNR. This is particularly essential in low light FRET applications like single-molecule FRET (smFRET). smFRET is an excellent tool for studying the the structure and dynamics of proteins and nucleic acids as well as their interactions. Recent publications in these areas include visualising conformational changes in proteins such as enzymes during their catalytic cycle<sup>35</sup> and monitoring DNA synthesis in real-time.<sup>36</sup>

Despite all the advantages of fluorescence microscopy, the main limitations are associated with the photophysics and photochemistry of fluorescent labels.<sup>37</sup> The number of emitted photons per second is limited by the limited frequency in a fluorophore's excitation-emission cycle, which is defined by the finite lifetime of the excited state. Non-radiative relaxation pathways of a given excited fluorophore reduce the quantum yield, further limiting the number of detectable photons per unit time. Furthermore, the requirement to label the system adds additional experimental challenges, such as toxicity of labelling conditions<sup>38</sup> or disruption of biological mechanisms by probe insertion.<sup>39</sup> In recent years, as alternatives, various single molecule imaging techniques based on light scattering have been introduced to study biomolecules, which resolve

some of the difficulties found in fluorescence microscopy.

## 2.3 Scattering Microscopy

Unlike fluorescence microscopy, whose fundamental limit is based on the number of photons detected per second, light scattering is theoretically only limited by the incident light intensity, because the number of scattered photons simply scales with the number of incident photons.<sup>40</sup> Yet in practice, scattering-based detection has a major disadvantage of higher background over fluorescence, as any refractive index inhomogeneity scatters light. Therefore, it is crucial to find a strategy to remove any unwanted background to achieve single-molecule sensitivity.

Many single-molecule *in vitro* experiments operate near a glass-water interface.<sup>41</sup> If the microscope is designed to measure in reflection, 0.4 % of the incident illumination is reflected when light is directed to the interface. The light that is not reflected will then be scattered by any object at the interface with a different refractive index to the aqueous solution.

In general, the intensity measured at the detector,  $I_{det}$ , depends on any reference background light,  $E_r$ , the scattered electric field,  $E_s$ , as well as their relative phase difference,  $\varphi$ , in the following way:

$$I_{det} = |E_r + E_s|^2 = |E_r|^2 + |E_s|^2 - 2|E_r||E_s|\sin\varphi$$

As shown above, there are three terms that contribute to the detected intensity: (i) the combined reference and background signal  $|E_r|^2$ , (ii) the scattering signal  $|E_s|^2$ , and (iii) the interference term  $2|E_r||E_s|\sin\varphi$ . This relationship suggests two principle ways to optimise the detection of the scattering signals: (i) removal of background to reduce  $E_r$ , leaving only the pure scattering term  $|E_s|^2$ , or (ii) taking advantage of a well-defined reference field to control  $E_r$

and use the interference term,  $2|E_r||E_s|\sin\varphi$ , as the signal of interest. These two methods are classified as dark-field<sup>42</sup> and interference microscopy.<sup>17,43</sup>

### 2.3.1 Dark-Field Microscopy

Minimising background is usually achieved by using dark-field microscopy, where the incident light is separated from the light scattered by the sample. One of the most successful approaches takes advantage of total internal reflection (TIR) at a refractive index gradient either using prism-TIR or objective-TIR (Figure 2.2).<sup>44</sup> A prism is used in the former so that the incident laser light is directed to the sample at a critical angle to be entirely reflected at the water-glass interface. Perforated mirrors and micro-mirrors are used for directing the illumination beam to the objective for the latter, leaving space for the scattering image to be picked off and directed into the imaging path while excluding the illumination light.<sup>45</sup> As a result, an exponentially decaying evanescent field is generated within the sample region with a depth of a few hundred nanometres.<sup>26</sup> A microscope objective collects scattered light from the particles within this evanescence field region, which is then imaged onto a camera. Particles in dark-field microscopy appear as bright spots on a dark background.

With sufficient elimination of all background, the detected intensity should be reduced to:

$$I_{det} = |E_s|^2 = |E_i|^2 |s|^2$$

where  $E_i$  is the electric field of the incident light and  $s$  is the complex scattering amplitude.

Given that the scattering intensity scales with the intensity of the incident light, one should be able to increase signals in dark-field microscopy by higher incident light intensities. Lasers are useful as they provide much higher photon

## 2.3. Scattering Microscopy

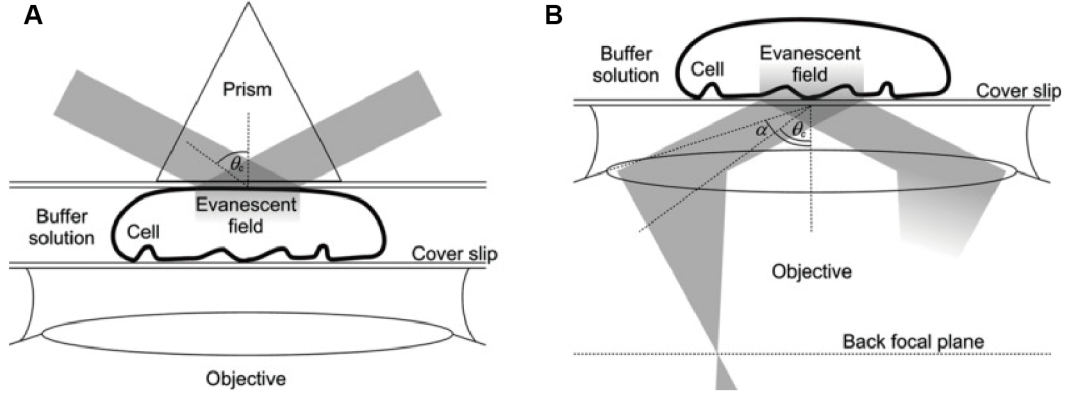


**Figure 2.2:** Prism- and objective-type TIRF. **(A)** In prism-type TIRF microscopy, the evanescent field is created on the opposite side of the sample from the objective lens that collects the fluorescence. The incident angle may have any value between the critical angle  $\theta_c$  and  $\pi/2$ . **(B)** With objective-type TIRF microscopy, fluorescence is collected from the sample on the same side as the excitation light is delivered. The range of incident angles is limited, as described by the numerical aperture of the objective, to angles between  $\theta_c$  and  $\alpha$ . A collimated excitation beam is achieved by focusing it off-axis in the back focal plane. Adapted from Martin-Fernandez *et al.* 2013.<sup>44</sup>

fluxes than traditional incoherent light sources.

Using general Mie theory,<sup>46</sup> the scattering amplitude,  $s$ , can be written as:

$$s(\lambda) \propto \alpha(\lambda) = \varepsilon_m(\lambda)\pi \frac{D^3}{2} \frac{\varepsilon_p(\lambda) - \varepsilon_m(\lambda)}{\varepsilon_p(\lambda) + 2\varepsilon_m(\lambda)}$$

where  $\varepsilon_p$  and  $\varepsilon_m$  are the complex dielectric constants of the particle and the medium,  $D$  is the particle diameter,  $\lambda$  is the wavelength of illumination and  $\alpha$  is the polarisability of the particle. In the small particle limit, the scattering amplitude  $s$  of a spherical particle (diameter  $< 1.6\lambda$ ) scales with the polarisability of the particle,  $\alpha$ .<sup>47</sup> Combining both equations, as the intensity of detected scattered signal,  $I_{det}$ , depends on the square modulus of the scattering amplitude,  $s$ , the signal thus scales with  $D^6$ . This means that the scattering cross section of the particle decreases rapidly with its size, thereby making it difficult to distinguish from the background. In other words, a particle with a 2-fold diameter reduction will result in a 64-fold decrease in the purely scattered

signal.

To maximise the scattering signal, gold nanoparticles (AuNPs) are particularly useful, because they exhibit a strong plasmon resonance in water centred around 530 nm for spherical particles ranging from 10 to 100 nm.<sup>48,49</sup> This resonance occurs when  $|\varepsilon_p(\lambda) + 2\varepsilon_m(\lambda)|$  is minimised, which results in an enhanced polarisability and thus larger scattering amplitudes and cross sections. As a matter of fact, a 40 nm AuNP illuminated at 532 nm scatters in water with nearly the same cross section as a 160 nm silica bead, enabling the use of much smaller labels with the same scattered photon flux. Nanometer-precise tracking on the microsecond time scale has become commonplace with improvements in microscope design, reaching 1.3 nm localisation precision at 55  $\mu$ s temporal resolution using 40 nm AuNPs.<sup>50</sup> A recent development using micromirrors demonstrates high SNR detection of 20 nm AuNPs, which is only limited by the scattering background caused by surface roughness, enabling SNRs on the order of 50.<sup>45</sup> However, even if the majority of background light intensity is suppressed, scattering detection still suffers from background scattering due to sample defects.

### 2.3.2 Interferometric Scattering Microscopy

When compared to most fluorescent dyes ( $< 1$  nm), fluorescent proteins ( $\sim 4$  nm), or quantum dots ( $\sim 10$  nm),<sup>51</sup> a 20 nm gold particle is still a large label. To minimise the effect of the labels on the structure and the function of biomolecules, it is desirable to use smaller labels or image entirely label-free to, for instance, reduce label-induced perturbations. As discussed earlier, the strong scaling of the scattering signal with size makes it technically very difficult to achieve equivalent results with smaller nanoparticles. By contrast, interferometric scattering microscopy (iSCAT) helps to reduce the size-scaling

### 2.3. Scattering Microscopy

---

problem and allow for high signal-to-noise ratio and non-resonant imaging of smaller-sized gold nanoparticles, and even direct detection of native, unlabelled biomolecules.<sup>3,18,52</sup>

Instead of avoiding all background illumination, one can introduce reflected light in a way that the pure scattering term  $|E_s|^2$  is negligible for small scatters. As a result, the main signal now comes from the interference between background and scattered light, with the contrast determined by the ratio of the total detected light,  $I_{det}$ , and the background reference light,  $I_{br}$ :

$$Contrast = \frac{I_{det}}{I_{br}} = \frac{|r|^2 - 2|r||s|\sin\varphi}{|r|^2} = 1 - \frac{2|s|\sin\varphi}{|r|}$$

where  $|r|^2$  is the reflectivity of the interface which provides the reference light, and  $\varphi$  is the phase difference between the scattered and reflected light.

Interference reflection microscopy (IRM) developed by Curtis in 1964,<sup>53</sup> and reflection interference contrast microscopy (RICM) developed by Ploem in 1975<sup>54</sup> first realised this principle. These techniques were originally used to study cell adhesion,<sup>55</sup> reconstruction of inter-facial topology,<sup>56</sup> and phase separation in lipid bilayers.<sup>57</sup> While these studies did not achieve the SNR at the level for nanoparticle detection, laser illumination enabled much higher power densities. In 2009, the first laser-based setup, termed interferometric scattering (iSCAT) microscope, was proved to be able to take non-fluorescence images of single quantum dots<sup>43</sup> and track a virus particle diffusing on a lipid bilayer.<sup>17</sup>

Figure 2.3A shows the fundamental experimental design of an iSCAT microscope.<sup>40</sup> To avoid non-uniform background in iSCAT images due to the emergence of laser speckle, a small laser beam is scanned across the sample instead of illuminating the entire sample by a focused laser beam. Scanned illumination from a collimated laser beam from a diode laser is achieved by

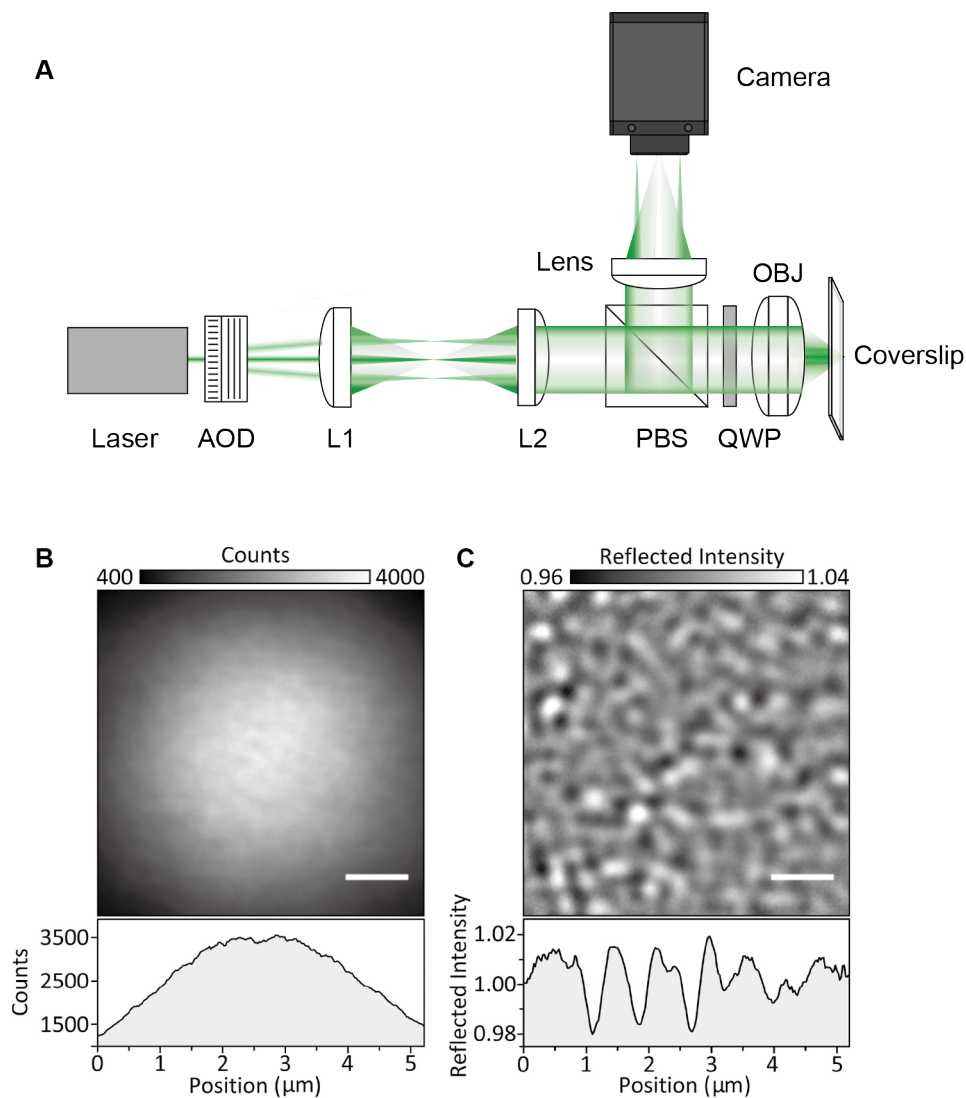


**Figure 2.3:** (A) Experimental setup: The Acousto-optic deflectors (AOD) scan the laser beam. The telescope (L1 +L2) images the plane of the AODs into the back focal plane of the objective (OBJ) and the laser beam is scanned across the sample. The quarter wave plate (QWP) and polarising beam splitter (PBS) separate the imaging and illumination channel. (B) Raw reflection image of a microscope cover glass covered by water upon illumination with a 445 nm laser using a combination of a polarizing beam splitter and quarter wave plate to separate incident from reflected and scattered light. (C) The same image as in B after division by a median image produced while laterally translating the sample. Scale bars: 1  $\mu\text{m}$ . B and C are adapted from Cole *et al.*, 2017.<sup>19</sup>

using a set of acousto-optic deflectors (AODs) and a telescope (L1 + L2).<sup>19</sup> The AODs deflect the beam through both  $\theta$  and  $\phi$  at two offset frequencies (e.g. 79 and 83 kHz) to create a mesh-like pattern. The plane of the AODs is then brought into focus by the telescope on the back focal plane of the objective (OBJ) so that each  $\theta$  and  $\phi$  correspond to an x and y coordinate in the plane of the coverslip, which is perpendicular to the optical axis. A polarising beam splitter (PBS) is used to separate the detection and illumination beam paths. The PBS sends linearly P-polarised illumination through a quarter waveplate (QWP) into the objective. The QWP circularly polarises the light when it enters and leaves the objective, 45 ° at one time. Therefore, the light coming back from the objective is transformed to linear S-polarisation, reflected by the PBS and then detected by the camera.

On an iSCAT setup, the reference field  $|E_r|$  dominates the image captured by the camera (Figure 2.3B). The reflection from the glass-water interface, however, is sample-independent. By flat-fielding the image, one can reveal the smaller sample-dependent scattered signals.<sup>58</sup> This is accomplished by acquiring a stack of N frames during which the sample is translated, and then dividing each consecutive frame by the invariant median of the acquired stack. This eliminates all static features, leaving a flat-field image dominated by the scattering signal from the glass surface roughness (Figure 2.3C). Through the static background subtraction, any changing signals smaller than the glass roughness can be observed from this flat-field image.

The SNR achievable for an ideal iSCAT experiment is only limited by shot noise, which describes the fluctuations of the number of photons detected due to their occurrence independent of each other. The shot-noise-induced background fluctuation as a percentage of the detected signal for a shot-noise-limited experiment is given by  $\sqrt{N}/N$ , where N is the number of detected

photoelectrons per pixel. Therefore, the SNR for a shot-noise limited iSCAT experiment scales with the square root of  $N$ :

$$\text{SNR} = \frac{\text{iSCAT signal}}{\text{background fluctuations}} = \text{contrast} \sqrt{N}$$

More photons can be collected per pixel for a given exposure time and camera well depth by using higher magnifications than are required for the appropriate sampling of a diffraction-limited point spread function (PSF) and then spatially binning pixels together. Frames can be averaged together at the loss of time resolution in a similar way. This raises the SNR to the point where the background glass roughness starts to be averaged into the image by other noise sources such as mechanical drifts. On the other hand, both the biological systems' ability to tolerate high illumination intensities and the camera sensor's full well capacity limit the applied laser intensity. Cameras with high full well capacity can capture higher photon fluxes. However, this method has drawbacks, as most cameras with high full well capacities are expensive and have low quantum efficiencies, making them inefficient at collecting incident light.<sup>19</sup>

### **2.3.3 Contrast Enhanced iSCAT via Numerical Aperture Filtering**

An alternative way to using a high full well camera would be to increase the contrast of a molecule while capturing the same number of photons, so as not to saturate the detector. As suggested in the previous contrast determination, reducing the reflectivity of the glass-water interface,  $r$ , while maintaining the scattering amplitude,  $s$ , will therefore result in an increase in contrast. Partial attenuation of the reference field by numerical aperture filtering helps in this case.<sup>19</sup>

Taking advantage of the fact that most signals from small scatterers close to the glass-water interface are collected at high numerical apertures by the objective,<sup>59</sup> enables reduction of the reflected illumination beam (Figure 2.4). As demonstrated in the previous studies<sup>59,60</sup>, a point source near a refractive index interface radiates the majority of photons into the higher index material in directions associated with a high numerical aperture of the collecting lens (Figure 2.4A). Meanwhile in optical microscope, wide-field illumination is usually achieved by focusing an incident beam into the back focal plane of the imaging objective, which only requires a very low NA. By coupling the illumination light into the low NA of the objective, the reference reflection from the interface will also be localised in the low NA. Then, if one places a partially reflective mirror in the BFP of the objective (Figure 2.4B), it will attenuate the low NA contributions to the image, and thus attenuate the reference field over the scattered field. By adjusting the thickness of the metallic layer on the partially reflective mirror, the degree of attenuation can be tuned to the incident light intensity and camera properties. The reduction in scattered light detection caused by this experimental arrangement, however, amounts to only 11.3 % when using an oil immersion objective with an 8.52 mm diameter back aperture in combination with a 3.5 mm diameter partially reflective mirror (Figure 2.4C)<sup>61</sup>.

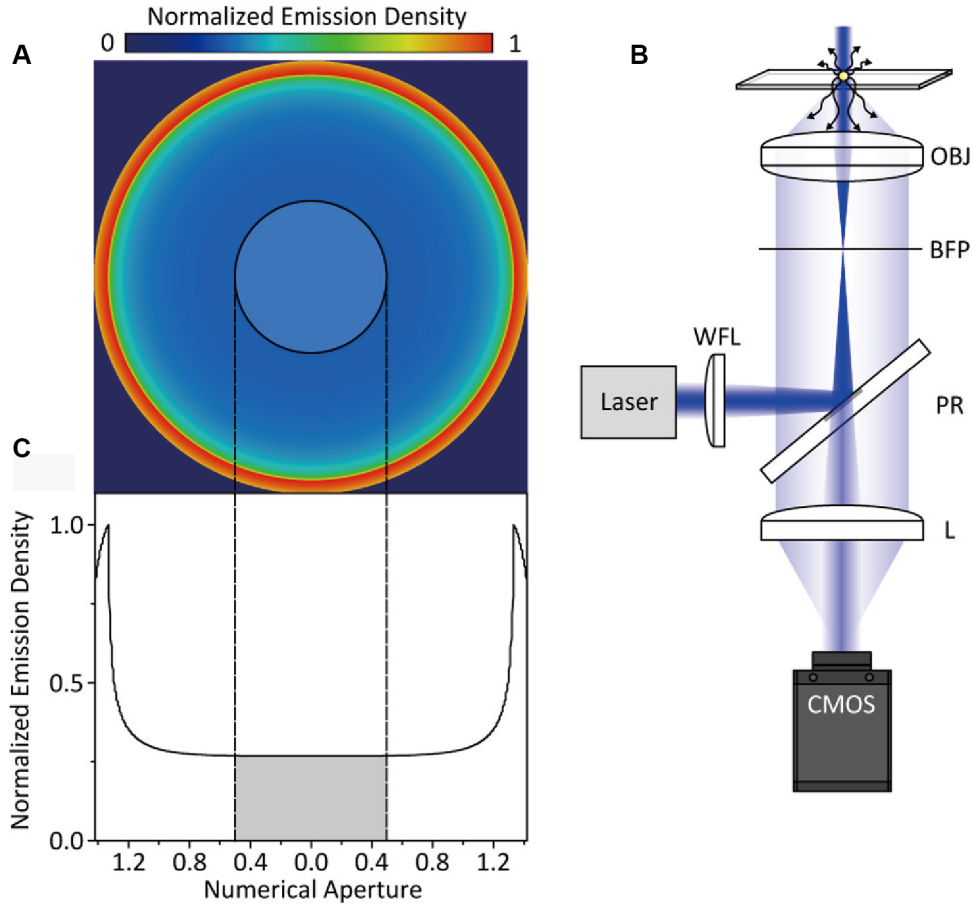


**Figure 2.4:** Concept and experimental realization of numerical aperture-filtered interferometric scattering microscopy (iSCAT). (A) Emission pattern of a nanoscopic scatterer at a glasswater interface emerging from the back aperture of a high-numerical-aperture (1.42) microscope objective for circularly polarised illumination.<sup>59</sup> The semi-transparent circle indicates the region occupied by a partial reflector shown in the experimental setup in B. (B) Schematic of a numerical aperture-filtered iSCAT microscope. A single-mode fiber-coupled diode laser is loosely focused with a wide-field lens (WFL) into the back focal plane (BFP) of an oil immersion objective (OBJ). The partial reflector (PR) couples illumination light in and out of the inverted microscope and attenuates the reflected light before being imaged onto the camera (CMOS) by another lens (L). (C) Emission density as a function of numerical aperture, with the gray area indicating the region attenuated by the partial reflector. Adapted from Cole *et al.*, 2017.<sup>19</sup>

In this manner, the contrast of scattering objects will be selectively enhanced at the expense of the total number of detected photons. In particular, if a partially reflective mirror reduces the reference light  $|E_r|^2$  by 100-fold, the reflectivity term  $|r|$  will be reduced by 10-fold. Therefore, the contrast will

exhibit a 10-fold increase, as shown in Figure 2.5 as compared to Figure 2.3. Note that to generate comparable images, 100-fold longer exposure time is used for Figure 2.5 compared to Figure 2.3, while Figure 2.3 represents the average of 100 consecutive images. In this way, the total number of incident and detected photons is identical for Figure 2.5 and Figure 2.3.

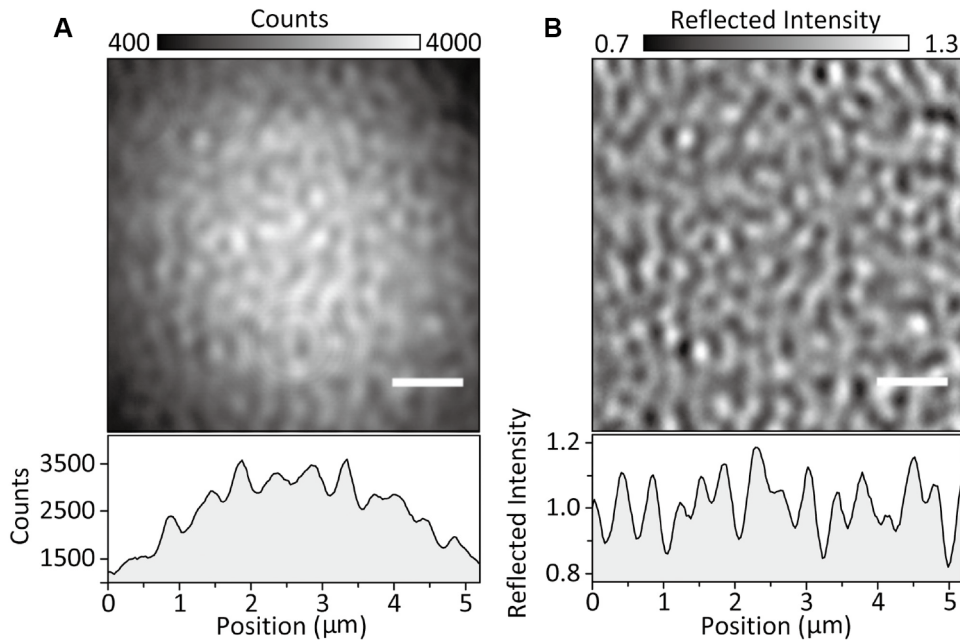


**Figure 2.5:** Effect of a partial reflector on iSCAT contrast. Equivalent iSCAT images to Figure 2.3 B and C with numerical aperture filtering using a 1% transmissive partial reflector. To generate equivalent images, 100-fold longer exposure time was used. (A) A Raw iSCAT reflection image of microscope cover glass covered by water. The contrast of glass roughness is noticeably enhanced as compared to Figure 2.3B and C. (B) The same image after division by a median image produced while laterally translating the sample. Scale bars: 1  $\mu\text{m}$ . Adapted from Cole *et al.*, 2017.<sup>19</sup>

Importantly, the method, by itself, does not improve the SNR because the number of detected photons on the camera decreases. For a 100-fold decrease in incident light on a camera, the shot-noise-induced background fluctuation with the same exposure time and incident light intensity increases by 10, which matches the increase in contrast. However, this allows one to increase the illumination intensity accordingly. The main benefit of this approach is that by using the correct combination of illumination intensity and transmissivity

of the partial reflector, the higher illumination intensity increases the absolute sensitivity of the microscope. Moreover, the camera no longer requires a high full well capability and photons can be captured in a more efficient way.

## 2.4 Mass Photometry

### 2.4.1 Protein Mass Determination

The application of NA filtering, together with improvements in the hardware and data analysis, has resulted in significant advancements in the detection sensitivity, precision, and mass resolution of label-free single-molecule mass measurements (Figure 2.6).<sup>3</sup> As the scattered signal scales with  $D^3$ , or namely the volume of the molecule, for particles of different mass but comparable refractive index, their contrasts scale linearly with their mass.<sup>3,16</sup> This principle can be used to generate mass distributions of proteins in solution since the specific volumes of amino acid sequences and their refractive indices vary only by 1%. For example, the contrast distributions from a sample of bovine serum albumin (BSA) molecules (66 kDa) show well-resolved (19 kDa full width at half-maximum (FWHM)), equally spaced peaks as expected for different oligomeric states of the same protein (Figure 2.6A). In addition, mass measurement of a wide range of proteins has shown a sequence mass accuracy up to 2% (Figure 2.6B). This high level of accuracy greatly simplifies the identification of unlabeled species by mass, allowing for more highly multiplexed detection than fluorescence-based methods which require labelling.

### 2.4.2 Recent Applications

The ability to separate different oligomeric states based on high measurement precision, in combination with its label-free detection, single-molecule sensitivity, mass measurement, solution operation, has resulted in significant adoption

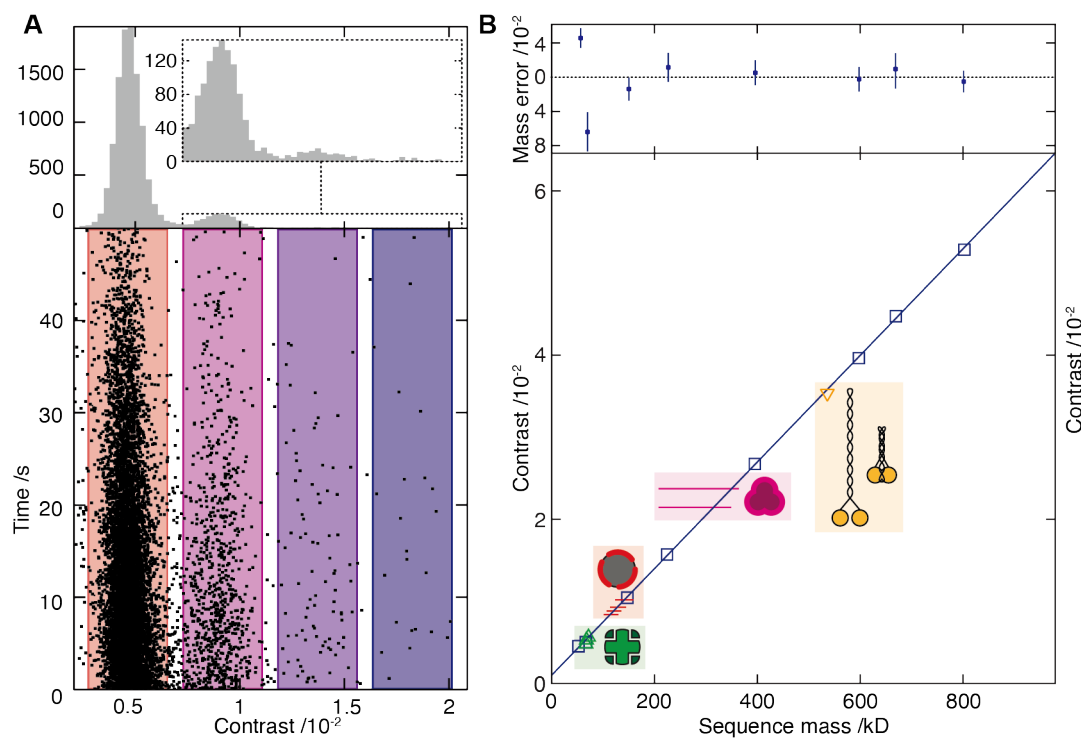


**Figure 2.6:** Mass photometry principle and accuracy. (A) Scatter plot of single-molecule binding events and their scattering contrasts for 12 nM BSA from 14 movies (lower panel). Corresponding histogram ( $n = 12,209$ ) with a zoomed-in view of the region for larger species (upper panel). The reduction in landing rate results from a drop in BSA concentration with time owing to the large surface-to-volume ratio of our sample cell. (B) Contrast versus molecular mass, including for proteins used for mass calibration (black), characterization of shape dependence (yellow), protein-ligand binding (green), lipid nanodisc composition (red), and glycosylation (blue). Mass error (upper panel) is given as a percentage of the sequence mass relative to the given linear fit. Reproduced from Young *et al.* 2018.<sup>3</sup>

of MP since its emergence. This includes applications to membrane proteins, membrane-associated proteins, microtubules, protein kinases, proteasomes and viral capsids.<sup>62-67</sup> Furthermore, Foley *et al.* has introduced dynamic MP in a recent study as a tool for label-free tracking and mass measurement of individual membrane-associated proteins diffusing on a supported lipid bilayer.<sup>68</sup>

Moreover, because of the speed, sensitivity, and relative simplicity of a typical MP experiment, MP is well-suited to sample characterisation for more structure-specific analytical techniques, such as cryo-electron microscopy (cryo-EM) and X-ray crystallography.<sup>69</sup> Sonn-Segev *et al.* has demonstrated this in a recent study by quantifying the heterogeneity of macromolecular complexes. The results obtained are comparable to those gathered from corresponding negative stain EM workflows.

Additionally, MP's ability to count individual molecules can be used to precisely measure the relative abundances of different biomolecular complexes in solution, providing information on the associated binding affinities and interaction kinetics.<sup>4,5</sup> In Soltermann *et al.*'s work, their MP measurements determined the binding affinities over four orders of magnitude at equilibrium for both simple and complex stoichiometries within minutes, as well as the associated kinetics. MP has also been used to quantify binding affinities in FOXP2 oligomerisation and its DNA binding, and for qualitative assessment of affinities between casposase and DNA.<sup>70,71</sup>

Taken together, the wide applicability to different biological systems has demonstrated MP's potential to become a universal tool for studying biomolecular assemblies, interactions and dynamics in a rapid, label-free, single-molecule fashion.

## 2.4. Mass Photometry

---

# Chapter 3

## Visualising Nucleation by Interferometric Scattering Microscopy

### 3.1 Introduction

#### Crystallisation and Nucleation

Crystallisation, as a phase transition, has wide applications in science, such as facilitating purification and separation, and establishing its structure and properties as an ordered solid. The complex process involves two key steps: nucleation followed by crystal growth. Among these two steps, nucleation is less well understood due to its stochastic nature.

Classical nucleation theory developed by Gibbs, Volmer, Becker and Doring assumes that molecules form small clusters in equilibrium by successive bimolecular additions.<sup>72</sup> If a cluster reaches a critical size set by the level of supersaturation, it will not redissolve but continue to grow, which becomes a nucleation point. While classical nucleation theory provides a successful description in many systems, studies on the crystallisation of proteins and colloids have shown results beyond the classical view. The later developed two-step nucleation mechanism proposed by Ten Wolde and Frenkel,<sup>73</sup> suggests that the two order parameters of density and structure develop sequentially

instead of simultaneously. A meta-stable intermediate phase (MIP) forms first from the supersaturated solution, followed by nucleation taking place inside the MIP. Yet this theory still requires a critical size for a crystal to grow, and involves no assumptions on its shape and structure.

## **Non-Photochemical Laser-Induced Nucleation**

It is well-known that nucleation of a metastable sample can be induced by physical perturbations, such as mechanical shock, rapid cooling, and seeding.<sup>74</sup> Employing the action of light is, on the other hand, an intriguing method to study nucleation. In 1869, photochemically induced nucleation was first described, where the incident light had sufficient energy to cause ionisation or to create radicals that subsequently reacted to produce nucleation centres.<sup>75</sup> Almost two decades ago, non-photochemical laser induced nucleation (NPLIN) was discovered accidentally by Garetz *et al.*, when studying the nonlinear optical properties of supersaturated aqueous solutions of urea.<sup>76</sup> It was reported that nanosecond pulses of near-infrared light (1064 nm) could drastically reduce the induction time of urea crystals. The wavelength and the power of the light were not sufficient to induce photoionisation. Preferential formation of crystals along the axis of the electric field of the incident light was observed by examining alignments of the crystalline structures and the polarisation of the incoming laser beam.

Since its emergence, several reports have demonstrated NPLIN on other chemical compounds as diverse as glycine, L-histidine, hen egg white protein and sulfathiazole in different solvents including water, ethanol and agarose gel.<sup>77–80</sup> More recently, NPLIN has been demonstrated to work with potassium halides whose ions in solution are centrosymmetric.<sup>81</sup> Alexander and co-workers have studied NPLIN of a number of metastable systems,<sup>82,83</sup> in particular

the benchmark system of aqueous potassium chloride (KCl).<sup>81,84</sup> The studies demonstrated that samples of KCl with supersaturation ( $S = C/C_{\text{sat}}$ ) in the range 1.05 - 1.10 can be nucleated by a single pulse from a nanosecond laser. Despite the recent observations in NPLIN occurring in different systems, the details of its mechanism remain unrevealed. Methods looking into single crystals which enable real-time characterisation of crystal size, shape, growth and polydispersity are highly desirable.

## Metal-Organic Frameworks

To study the formation of extended materials in general, the metal-organic framework (MOF) is thought of as an ideal model system. MOFs are of increasing industrial interests for gas storage, separation, catalysis etc., owing to their modular, porous structure based on metal nodes and organic linkers.<sup>85,86</sup> Better understanding in MOF nucleation and crystal growth will lead to improvements in synthesis efficiency and potential to design new materials. However, despite the increasing attention, the underlying mechanism of its formation remains poorly understood.

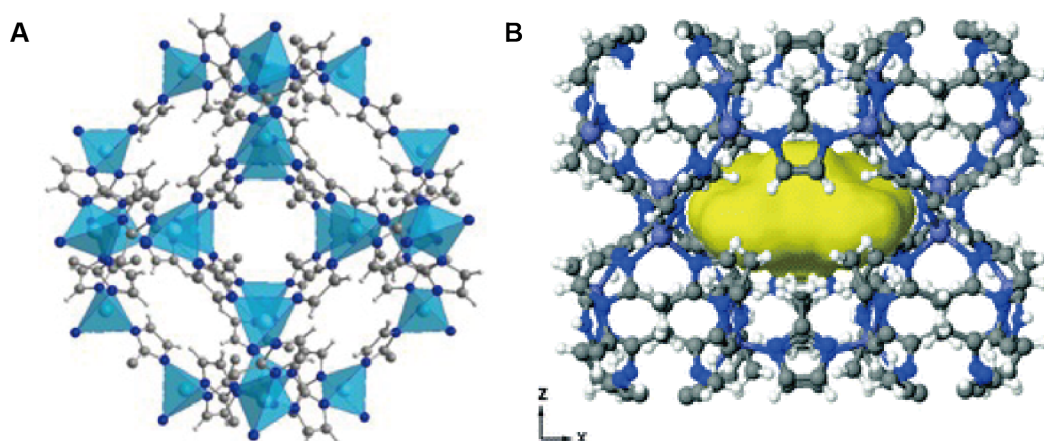


**Figure 3.1:** The structures of ZIF-8 and ZIF-L. (A) The structure of ZIF-8. (B) The structure of ZIF-L viewed along y with an isosurface showing the location and approximate shape of the cavity (yellow). This isosurface was calculated using the program Jmol (Jmol: an open-source Java viewer for chemical structures in 3D. <http://www.jmol.org/>). Adapted from Chen *et al.*, 2013.<sup>87</sup>

Literature on the prototypical Zinc 2-Methylimidazolate (mim) system has shown that its formation is solvent-dependent. In methanol, ZIF-8 ( $\text{Zn}(\text{mim})_2$ ) (Figure 3.1A) rapidly forms as pseudo-isotropic nanoparticles of 40–100 nm in diameter.<sup>88,89</sup> While in water, at low mim:Zn ratios, a related phase, ZIF-L ( $\text{Zn}(\text{mim})_2 (\text{Hmim})_{1/2} (\text{H}_2\text{O})_{3/2}$ ) (Figure 3.1B) forms as flat, lenticular micron-sized particles.<sup>87</sup>

Among these two formations, ZIF-8 synthesis (in methanol) is thought to proceed via a dynamic equilibrium in solution of molecular clusters of the size of 1 nm.<sup>90</sup> However, the assembly mechanism of such clusters is still unknown. Further information about the aggregation of particles, and the growth of thin films on surface, would be substantial.

## Visualising Crystallisation by iSCAT and MP

As explained in Section 2.3, iSCAT has been shown to be sensitive enough to detect single protein molecules,<sup>18</sup> and since any object with a different refractive index to that of its environment will scatter light, iSCAT should enable observations of detailed crystal nucleation and growth on a single crystal level. In this chapter, we use a home-built iSCAT and a commercialised mass photometer to analyse the nucleation and crystallisation events of two different inorganic systems, from NPLIN of KCl solution to crystallisation of (ZIF)-8 and (ZIF)-L. The advantages of studying these two particular systems are (i) one has better temporal and spatial control over the nucleation conditions, (ii) the systems themselves are potentially more theoretically tractable, (iii) there is no photochemical damage to the systems. These advantages enable direct implementation of iSCAT and MP, helping us to provide insights into a new direction of applications of iSCAT and MP beyond biomolecules at the early stage of explorations.

## 3.2 Materials and Methods

### Customised iSCAT Microscope

The custom-made iSCAT microscope is detailed in Figure 3.2. A collimated 200 mW 635 nm diode laser (Lasertack) passes through a telescopic lens system (TL1 + TL2) and a 50  $\mu\text{m}$  pinhole (PH) which spatially filters the beam. A 500 mm lens (L1) focuses the beam into the back focal plane of a high numerical aperture microscope objective (Nikon 60x, 1.42NA). A partially transmissive mask (diameter = 3.5 mm) placed near the back focal plane of the objective couples the illumination light into the microscope and attenuates the light reflected from the interface, leaving the light scattered by nanoscopic objects near the interface (which is radiated mostly into high collection angles) largely unaffected. This enhances the image contrast<sup>19</sup>. The scattered and reflected light is imaged onto a camera (CMOS) (Point Grey Grasshopper 3) with a 400 mm achromatic lens (L3), giving a magnification of 120x and an effective pixel size of 48 nm per pixel.

The sample is mounted on a 3D stage, with a piezo fitted on the Z axis for active focus stabilisation. The high numerical aperture of the objective allows total internal reflection at the glass-water interface. A large collimated beam (660 nm, < 1 mW) is coupled into the microscope objective, which focuses it at the sample. There, the parts of the beam associated with numerical apertures greater than 1.33 undergo total internal reflection. The reflected beam is imaged onto another camera (CAM) (Thorlabs), yielding an image of a bright ring, the radius of which changes with focus and so can be used as a readout of the focus position for active stabilisation. A 638 nm longpass dichroic mirror separates the two channels.

A pulsed laser channel is spatially filtered through a multimode fibre and coupled into the iSCAT microscope through a 600 nm shortpass dichroic mirror,

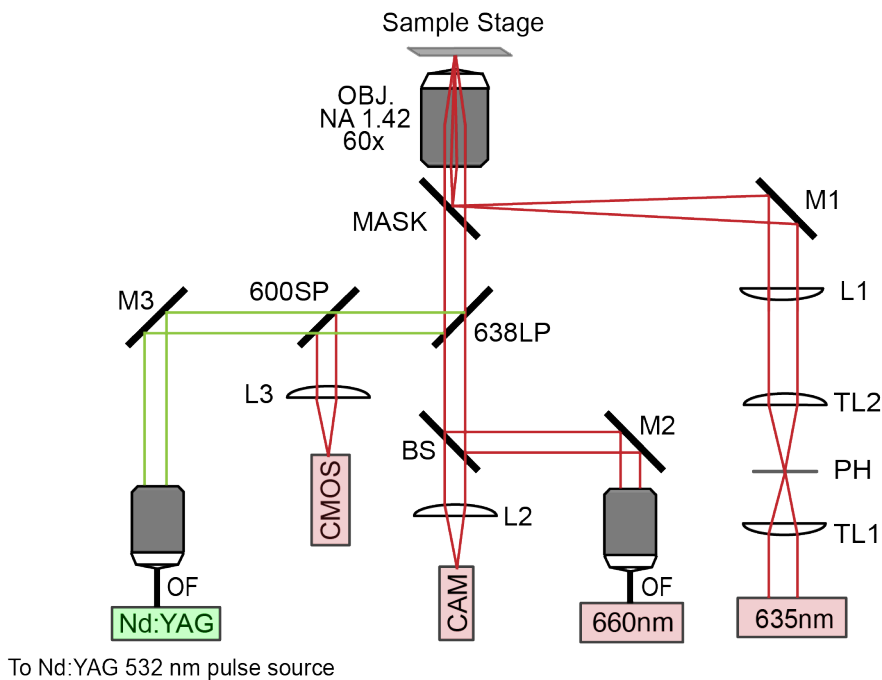


**Figure 3.2:** Experimental setup for iSCAT microscopy. OBJ – objective, M – mirror, TL – telecentric lens, L – plano-convex lens, PH – pinhole, LP – longpass dichroic mirror, SP – shortpass dichroic mirror, OF – optical fibre, BS – beamsplitter.

allowing NPLIN to be initiated. The NPLIN laser source is lined up to the centre of the field of view of the iSCAT channel, which gives the experimental setup the ability to record the first instance of crystallisation in a supersaturated solution.

Movies of 20 nm gold, GroEl and supersaturated KCl solutions were recorded by custom-written Labview software. The movies of GroEl were analysed in a ratiometric fashion by custom-written Labview software. The output h5. file was then analysed in python to generate the histogram and for Gaussian fitting. There was no post processing for the images of the KCl crystals.

For estimating the sensitivity of the customised iSCAT microscope in terms of nanometres, we calculated the radius of the protein based on its molecular mass. If we assume the protein has the simplest shape, a sphere, we can calculate its radius  $R_{min}$ , as the minimal radius of a sphere that could contain

the given mass of protein  $M$ :

$$R_{min} = (3V/4\pi)^{1/3} = 0.066M^{1/3}$$

where  $M$  is in Dalton and  $R_{min}$  is in nanometer<sup>91</sup>.

## Mass Photometry

Solutions of both (ZIF)-8 and (ZIF)-L in methanol and water were prepared by Yeung, H.H. All measurements were performed using the commercially available One<sup>MP</sup> mass photometer (Refeyn Ltd, Oxford, UK). Data acquisition was performed using Acquire MP (Refeyn Ltd, v1.1.3). Movies were recorded at 1 kHz for small rectangular FOV ( $3.8 \times 10.8 \mu m^2$ ) and 200 Hz for larger FOV ( $14.2 \times 14.2 \mu m^2$ ), with exposure times adjusted to maximise camera counts while avoiding saturation. Images were time averaged 5-fold and pixel binned 4 x 4 before saving, resulting in an effective pixel size of 84.4 nm/pixel. All iSCAT images shown in Figure 3.5 and 3.6 other than Figure 3.6C were then processed with a background removal by custom-written Labview program. The background of each movie was generated by averaging the first 100 frames, and then subtracted from each frame. Figure 3.6C is shown as the raw image with no post processing.

## 3.3 Results and Discussion

### 3.3.1 Characterisation of the iSCAT Microscope

To investigate the capabilities of the custom iSCAT microscope, it is important to analyse how small a particle it is possible to image and how sensitively it can detect a small movement. Therefore, imaging of 20 nm diameter gold nanoparticles and GroEL as small scattering signals were tested. 20 nm diameter gold nanoparticles (BBI solutions) were clearly identified on glass on

the image which was flat-fielded for non-uniform illumination intensity (Figure 3.3A). The image of a cleaned glass surface while GroEL molecules bound non-specifically to it out of solution was acquired at an effective frame rate of 10 Hz after averaging 100 frames (Figure 3.3B). In order to detect signals much smaller than the background, the image here was divided by the glass roughness background. The contrast of individual GroEL binding events was extracted by fitting to a model point spread function and such events were plotted in a histogram (Figure 3.3C). The mean contrast and the standard deviation are  $4.4 \times 10^{-3}$  and  $6.9 \times 10^{-4}$ , respectively. Using the molecular mass of 800 kDa and the linear relationship between interferometric contrast and protein mass, the standard deviations of these histograms correspond to a mass of approximately 125 kDa. Assuming the protein has the simplest shape, a sphere, the radius of a 125 kDa protein can be estimated as 3.3 nm,<sup>91</sup> showing that the microscope is capable of detecting early crystallisation events with high sensitivity.

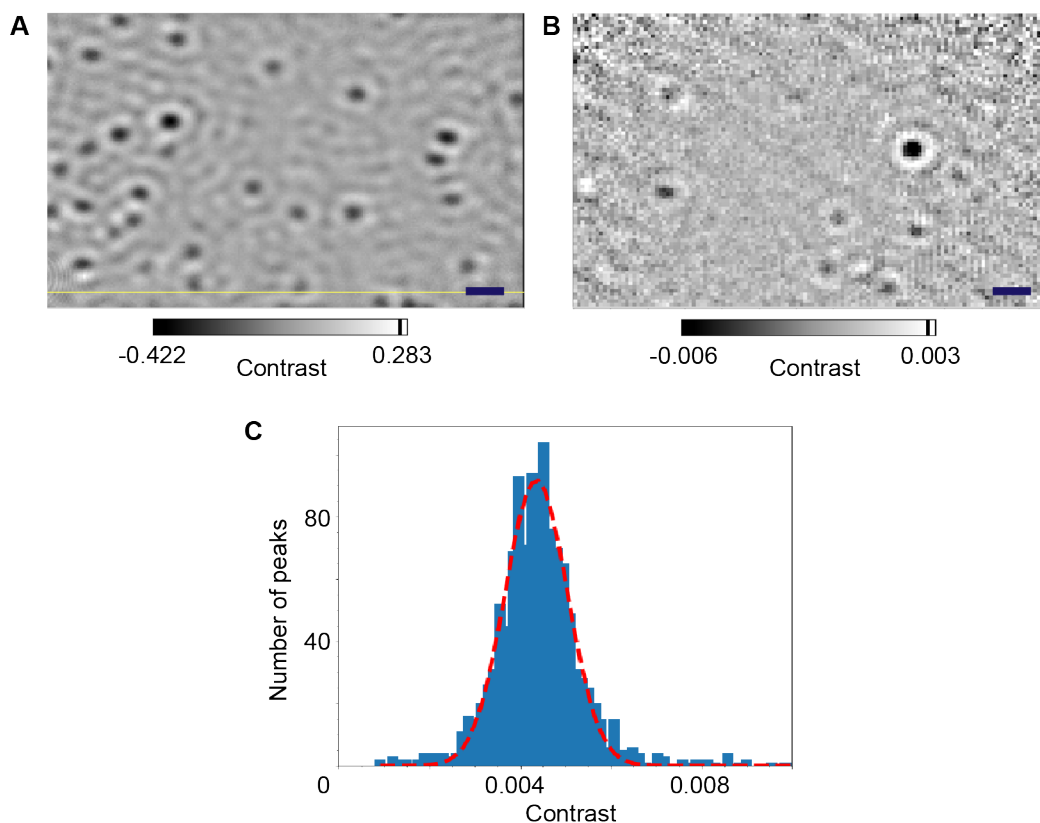


**Figure 3.3:** Performance of the customised iSCAT microscope. (A) Normalised interferometric image of 20 nm gold on clean glass. (B) Ratiometric image of GroEL on clean glass. Scale bars: 1  $\mu\text{m}$ ; (C) Histogram shows interferometric contrast of an 800 kDa GroEL protein imaged on the setup. Red line shows a Gaussian fit to the histogram, with mean contrast and standard deviation of  $\mu = 4.4 \times 10^{-3}$ ,  $\sigma = 6.9 \times 10^{-4}$ .

### 3.3.2 Nucleation in Supersaturated Solution

The advantage of using KCl for studying NPLIN is that one has a better control over the nucleation conditions, and the system is also potentially more theoretically tractable. Here, supersaturated solutions of KCL ( $S = 1.08$ ) were prepared, and their crystallisation was imaged. The supersaturated solution interface was brought into focus and was irradiated with pulsed 532 nm radiation from a Nd: YAG laser (Continuum Surelite SL II-10), with an approximate intensity of  $0.6 \text{ MJ/cm}^{-2}$ , in order to initiate NPLIN.

Uniform crystals and small particles were observed after a single pulse

(Figure 3.4). However, these signals were detected while going through the whole sample instead of being observed near the interface exclusively, which was required for quantitative imaging. It was thus difficult to characterise whether we observed the thermal effects or whether the pulsed laser caused crystallisation at this stage. Still, these results show that iSCAT can be used to study a single crystal of the size ranging from hundreds of nanometres to a few micrometres.

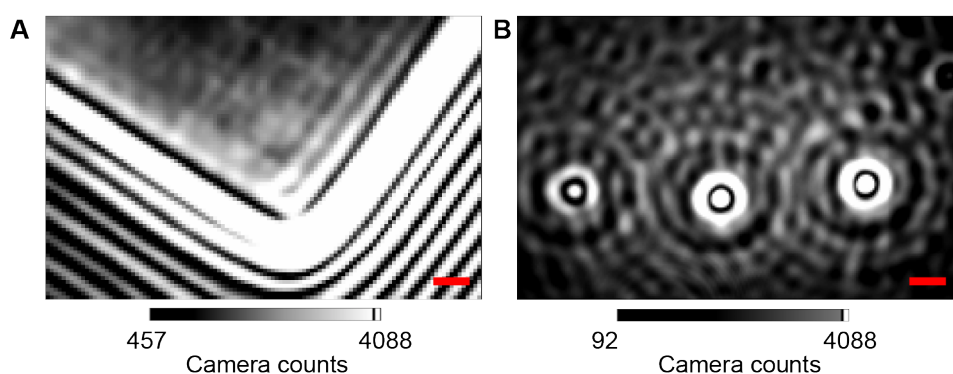


**Figure 3.4:** Interferometric images of KCl crystals after induction by a 532 nm pulsed laser. (A) A uniform and giant crystal. (B) Small crystals on clean glass. Scale bars: 1  $\mu\text{m}$ .

### 3.3.3 Crystallisation of (ZIF)-8 and (ZIF)-L

Measuring (ZIF)-8 in methanol by a commercially available mass photometer provided detailed information across different stages during its formation. Small particles whose sizes were smaller than 200 nm (diffraction limit) formed immediately after mixing and remained in solution throughout the measurement which lasted about 10 minutes. This agrees with the observation found in previous studies, where ZIF-8 nanocrystals form rapidly at room temperature to about 40 nm and grow until 100 nm at 10 mins after mixing.<sup>88</sup> However, the 1 nm metastable intermediate pre-equilibrium species were not detected due to the current limited detection sensitivity. At about 5 mins after mixing, larger particles started emerging in solution and binding irreversibly to the glass

surface (Figure 3.5A). The signals of these particles are slightly asymmetric when compared with the standard PSF, and considered to be larger than the diffraction limit of 200 nm. The size of these particles is therefore estimated as 300 - 400 nm. The growth rate observed by MP can then be estimated as 60 - 80 nm/min. This estimation is close to the previous finding observed by AFM under room temperature, which is found to be at  $\sim 5 \times 10^{-1}$  nm/s ( $\sim 30$  nm/min)<sup>92</sup>. Continued binding of these large particles resulted in layers on the surface (Figure 3.5B). Yet fast evaporation of organic solvent inhibited long-term measurements required for the latter stage of ZIF-8 growth.

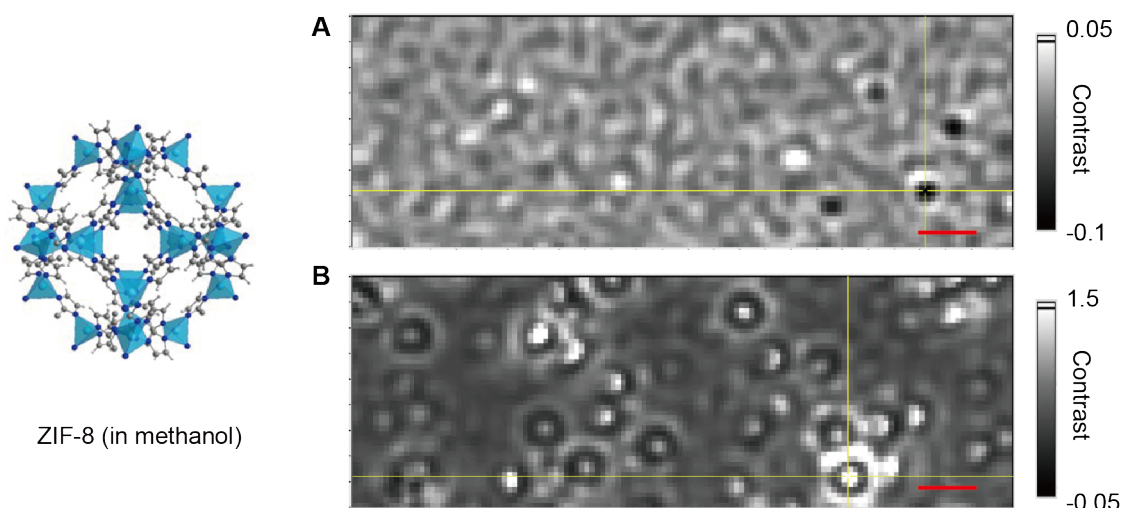


**Figure 3.5:** Crystallisation of (ZIF)-8. **(A)** Small particles ( $< 200$  nm) form rapidly and exist in solution throughout. Larger particles (300 – 400 nm) (as shown at the intersection of the yellow lines) bind irreversibly to glass surface at 5 mins after mixing. **(B)** Continued binding of larger particles forms layers on the surface. Scale bars: 1  $\mu$ m.

By controlling the Hmim/Zn ratio in aqueous solution, a two-dimensional ZIF-L structure was synthesised and measured by MP at room temperature. Particles (300 – 400 nm) appeared and bound to the glass, forming a surface layer at 5 mins after mixing (Figure 3.6A). At about 40 mins later, nonspherical crystals ( $> 400$  nm) emerged and bound to the surface (Figure 3.6B). These crystals are considered to be the reported flat and lenticular micron-sized

### 3.4. Conclusion and Outlook

---

crystals of (ZIF)-L. Finally, anisotropic crystals ( $\sim 1 \mu\text{m}$ ) are detected, as expected for (ZIF)-L crystals visualised by SEM (Figure 3.6C).<sup>87</sup> The resulted growth rate of ZIF-L crystal estimated by MP measurements is approximately at 10 - 25 nm/min, which is slower than the one of ZIF-8 crystal.

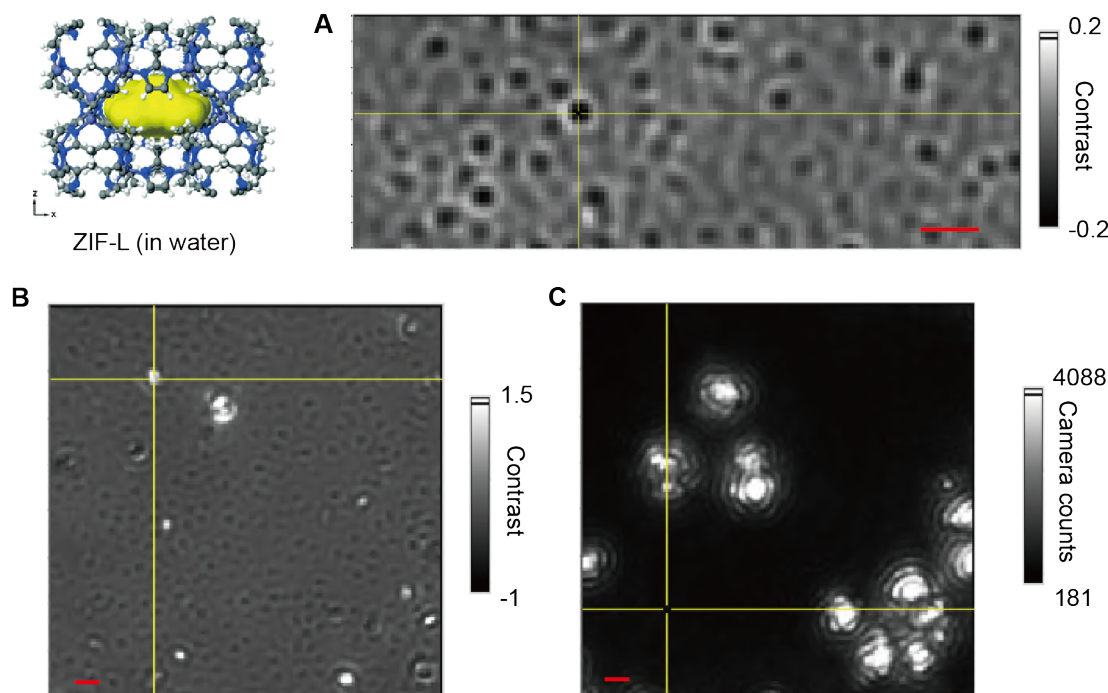


**Figure 3.6:** Crystallisation of (ZIF)-L. (A) From 5 mins after mixing onwards, particles of the size of 300 – 400 nm bind to the glass, and form a surface layer. (B) At longer time ( $\sim 40$  mins), nonspherical crystals ( $> 400$  nm) in solution gradually bind to the glass. These crystals may correlate to the reported flat, lenticular micron-sized particles of (ZIF)-L. (C) Eventually, anisotropic crystals ( $\sim 1 \mu\text{m}$ ) form as expected for (ZIF)-L. Scale bars:  $1 \mu\text{m}$ .

## 3.4 Conclusion and Outlook

Taken together, the customised iSCAT microscope has been shown to be capable of detecting small movements with high sensitivities over a short time period at 1000 fps. Additionally, the commercial mass photometer has been shown to be able to provide information on thin film formation as well as crystal growth. Further experiments looking to test the consistency of surface structures could determine whether the formed particles are crystalline or not. These studies

give an insight into the potential that iSCAT offers to study nucleation and crystallisation events.

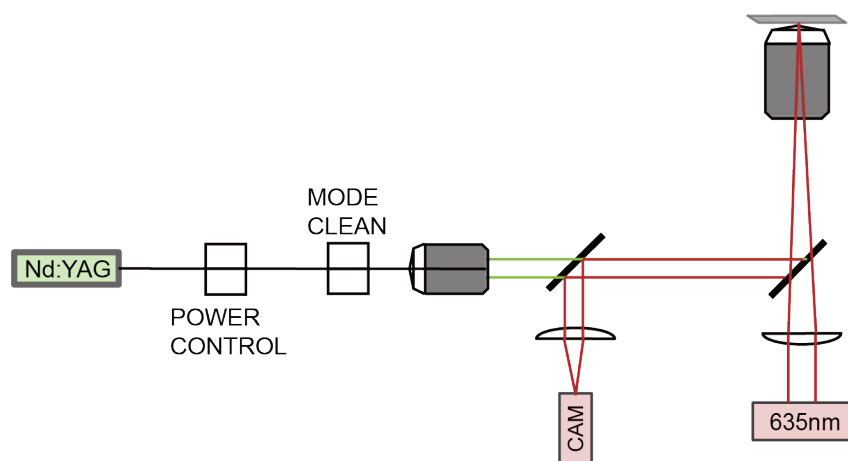


**Figure 3.7:** Improvements such as establishing a precise control over the power output of the laser pulse and using a single-mode fibre to control the location of nucleation spot can be made in the setup design.

Further improvements can be made in the setup design for study NPLIN (Figure 3.7). Instead of using a multimode fibre, applying a single mode fibre or coupling the pulsed laser in open space might actively help with observing the non-photochemical laser induced nucleation events in the first instance. The multimode fibre cannot focus tightly such that the nucleation might happen anywhere in solution instead of inside the field of view. While on the other hand, a single mode fibre with diffraction limited focus helps to set power such that the threshold is only exceeded within the beam focus in which it can control where nucleation happens. Besides, during the course of experiments, it was difficult to establish a precise control over the power output of the laser pulse. It is recommended to develop a better optical set-up, which utilises the combination of wave-plates and polarisers. A fine control over the power will also allow to precisely study the dependency of peak intensity on the efficiency of NPLIN.

Further to this, the effect of differing supersaturation, pulse length and power

### 3.4. Conclusion and Outlook

---

on the rate and direction of crystallisation should be probed to understand the mechanism of NIPBL. An addition of gold nanoparticles to the surface of the glass coverslip around which crystallisation of a supersaturated solution is initiated will not only provide data for the interaction of the crystal growth with the nanoparticles, but also allow potential surface enhanced Raman scattering (SERS) of the crystal to be studied.

With regard to measuring the crystallisation of (ZIF)-8 and (ZIF)-L by a commercial mass photometer, MP has shown to be able to detect the early stage of nucleation, to investigate thin film formation on a surface as well as to follow the latter stages of crystal growth. Even though the observed kinetics is still rough at this stage, the preliminary findings have found to match some of the results given by other techniques, such as static light scattering, X-ray diffraction (XRD) and wide-angle X-ray scattering.<sup>89,93,94</sup> However, it still remains a great challenge to quantify the crystal growth rate at the early stage due to fact that particles are smaller than the diffraction limit (200 nm). Further to this, for future experiments, modifications of the glass surface are favoured for slowing down the rate of nucleation and allowing reversible attachment of the particles onto the surface. This may help to eliminate the problem of focusing when measuring (ZIF)-8 in methanol, and to allow more representative observations of (ZIF)-L crystallisation in bulk solution by reducing the formation of a surface layer. In addition, with a larger FOV and longer timescales, one should be able to capture more information about the formation of an-isotropic (ZIF)-L crystals.

Overall, this chapter can be considered as an inspiration for iSCAT and MP to study the mechanism of matter beyond biomolecules. However, this strand of work requires a fairly good control of the system to be studied, also with the technical improvements within the setup to cope with the problems

such as the heating of the objective, the evaporation of the organic solvent and the difficulty in precisely determining the growth rate. Additionally, the development from iSCAT to MP based on its ability to quantify the mass of water-soluble molecules and produce dynamic data has drawn more attention to studying biomolecular interactions. Therefore, the research illustrated in this chapter was drawn to an early close and the work of this thesis was then switched to studying DNA and DNA-protein interactions. Still, through building the microscope and conducting preliminary data analysis, a solid understanding in the underlying mechanism and the fundamental operation of iSCAT and MP has paved the way to explore MP's applications to studying DNA and DNA-protein interactions.

### 3.4. Conclusion and Outlook

---

# Chapter 4

## Single Molecule Mass Photometry of dsDNA and ssDNA

Parts of this chapter are reproduced with permission from the following publication: Y. Li, W. B. Struwe and P. Kukura, Single molecule mass photometry of nucleic acids, *Nucleic Acids Research*, 2020, **48**, e97<sup>95</sup>

The 155mer of ssDNA samples were prepared and provided by the Tom Brown group at University of Oxford. The ssDNA scaffolds were provided by the Hendrik Dietz group at The Technical University of Munich. The DNA origamis were provided by the Philip Tinnefeld group at Ludwig-Maximilians-Universität München. All the data discussed in the results section were acquired and analysed by myself. The above publication was compiled and edited by all of the listed authors, including myself.

### 4.1 Introduction

Single molecule analysis has been widely applied to studying DNA structure, function and interactions.<sup>96</sup> Next generation sequencing heavily relies on single-molecule methods, especially those using single molecule fluorescence<sup>1,2</sup> or nanopore-based approaches.<sup>97,98</sup> Similarly, single molecule methods are now

extensively used in a variety of incarnations to study DNA–protein interactions,<sup>99</sup> with both DNA and proteins visualised by fluorescence labelling to reach single molecule sensitivity.<sup>100</sup>

Label-free detection and quantification would be highly desirable in this context because of the reduced experimental complexity and minimal potential perturbations. While visualisation of single DNA molecules has been possible for decades using non-optical methods, such as electron microscopy<sup>101</sup> and atomic force microscopy,<sup>102</sup> which can also be used to study mechanical properties,<sup>103</sup> label-free optical detection has remained a considerable challenge.

As referred in Sections 2.3 and 2.4, Mass photometry enables not only label-free detection and imaging of single molecules, but critically their quantification through mass measurement with high levels of accuracy, precision and resolution at a lower detection limit on the order of 40 kDa. Another important feature of MP is the capability to measure the distributions of proteins in bulk solution, from which one can extract binding affinities, kinetics and stoichiometries. While biomolecules have broadly comparable optical properties in the visible range of the electromagnetic spectrum<sup>104,105</sup>, important properties in the context of interferometric measurements, such as polarisability, refractive index and effective density, of DNA and proteins are still very different. To study DNA–protein interactions by MP, one would expect to measure and quantify DNA and protein molecules simultaneously with a mass accuracy sufficient for many application. Therefore in this chapter, we set out to investigate to which degree the capabilities of MP translate to nucleic acids, which would enable not only their detection, imaging and analysis, but also provide a universal route to studying DNA–protein interactions at the single molecule level.

## 4.2 Materials and Methods

### Sample Preparation

Solvents and chemicals were purchased from Sigma Aldrich unless otherwise noted. Milli-Q water and high-grade solvents were used for all experiments. A double-stranded DNA ladder consisting of 100, 200, 400, 800, 1200 and 2000 base pairs was purchased from Invitrogen (Cat. No. 10068013). A 100 bp dsDNA ladder consisting of 13 individual chromatography-purified DNA fragments in the range of 100–2000 bp was also purchased from Invitrogen (Cat. No. 15628050). Circular single-stranded DNA samples with 4536, 6048, 7249, 8064 bases were prepared as previously described.<sup>106</sup> Samples were kept in TE buffer (10mM Tris, 1mM EDTA) and no denaturing agent was used during measurements.

Single stranded DNA (155-mer) was synthesized on an Applied Biosystems 394 automated DNA/RNA synthesizer using a standard 0.2  $\mu$ M phosphoramidite cycle of acid-catalysed detritylation, coupling, capping and iodine oxidation. Stepwise coupling efficiencies and overall yields were determined by the automated trityl cation conductivity monitoring facility and was >98.0%. Standard DNA phosphoramidites and additional reagents were purchased from Link Technologies Ltd, Sigma-Aldrich, Glen research and Applied Biosystems Ltd. All beta-cyanoethyl phosphoramidite monomers were dissolved in anhydrous acetonitrile to a concentration of 0.1 M immediately prior to use with a coupling time of 50 s. Cleavage and deprotection were achieved by exposure to concentrated aqueous ammonia solution for 60 min at room temperature followed by heating in a sealed tube for 5 h at 55°C. Purification was carried out by denaturing 8% polyacrylamide gel electrophoresis, without any dye. In brief, formamide (500  $\mu$ l) was added to the DNA sample (500  $\mu$ l in water) before loading to the gel, bands corresponding to the full length were excised

## 4.2. Materials and Methods

---

and the DNA was isolated using the ‘crush and soak method’. The excised polyacrylamide pieces were broken down into small pieces then suspended in distilled water (25 ml). The suspension was shaken at 37°C for 18 h, then filtered through a plug of cotton wool. The filtrate was concentrated to ~2 ml, then desalted using two NAP-25 columns followed by one NAP-10 column. The desalted eluent was lyophilised prior to use.

Two different shaped DNA origami structures with the same molecular weight at 4.5 MDa were prepared and provided by Florian Selbach at LMU. The rod-like shaped DNA origami (12HB) with a length of around 200 nm and a diameter of 10 nm was folded as reported elsewhere.<sup>107</sup> The brick-shaped DNA origami (GATTA-Beads) with a diameter of around 20 nm was purchased from GATTAquant GmbH. No additional modifications were performed on both DNA origamis after folding. To acquire clean sample solutions with high quality for MP measurements, PEG precipitation was used to purify DNA origamis.<sup>108</sup> In particular, both DNA origami samples were mixed with the same amount of 12% PEG buffer (12% (w/v) PEG-8000, 1× TAE, 12 mM MgCl<sub>2</sub>, 500 mM NaCl) and centrifuged at 16,000×g for 45 mins at 4 °C. The supernatants were removed before adding the initial amount of 1× TE buffer containing 14 mM MgCl<sub>2</sub> to the pellets. All buffers were filtered before use.

Prior to MP measurements, 231 nM (0.1175 µg/µl) dsDNA stock solutions were diluted 25-fold in 5 mM Tris, 10 mM MgCl<sub>2</sub>, pH 8. The 100 bp dsDNA ladder stock solutions (0.5 µg/µl) were diluted 200-fold. Single-stranded DNA stock solutions (167 nM for 4536 nt, 125 nM for 6038 nt, 100 nM for both 7249 nt and 8064 nt) were diluted 10-fold in the same buffer. 7.79 µM 155 nt single-stranded DNA stock solutions were diluted 1000-fold. Standard protein marker solutions were diluted 10-fold in the same buffer. Both DNA origamis were diluted down to 12.5 nM during the measurements. Samples were kept at

room temperature during analysis.

### **Surface Functionalisation - APTES protocol**

While the general operating principle behind MP remain the same for DNA as the ones for proteins, the main difference between measuring the two is that due to negatively-charged backbone, DNA does not bind irreversibly to unmodified glass slides. To observe DNA binding to glass by MP, altering the charge of glass surface is necessary. In this chapter, (3-aminopropyl)triethoxysilane (APTES) functionalisation based on Nicholas *et al.*'s protocol was used to add a positive charge to the surface (Figure 4.1).<sup>109</sup> To obtain covalent binding of APTES to the surface, the  $O^-$  groups are first exposed on the glass surface by oxygen plasma cleaning before APTES is physisorbed onto the surface. APTES then forms a siloxane bond with the exposed  $O^-$  groups and, when heated to 100 °C, with neighbouring APTES molecules. Finally at physiological pH, the amine group carried by APTES is protonated to  $NH_4^+$  groups, providing a positive charge to the glass surface.

In practical, microscope coverglass (24 × 50 mm # 1, 5 SPEZIAL, Menzel-Glaser) and (3-aminopropyl)triethoxysilane (APTES)-functionalised coverslips were prepared as described previously.<sup>3,109</sup> Briefly, coverslips were cleaned by sequential sonication in 2% Hellmanex (Hellma Analytics), water and isopropanol for 10 min. For making APTES coverslips, the cleaned coverslips were then brought to plasma cleaning with oxygen (Diener electronic Zepto) for 8 min, after which they were immersed in 200 ml 2% APTES solution in anhydrous acetone for 1 min with agitation before rinsing in 200 ml anhydrous acetone. Finally, the coverslips were incubated at 110 °C for 1 h and cleaned by sonication in isopropanol (10 min) and water (5 min) before drying under a nitrogen stream.

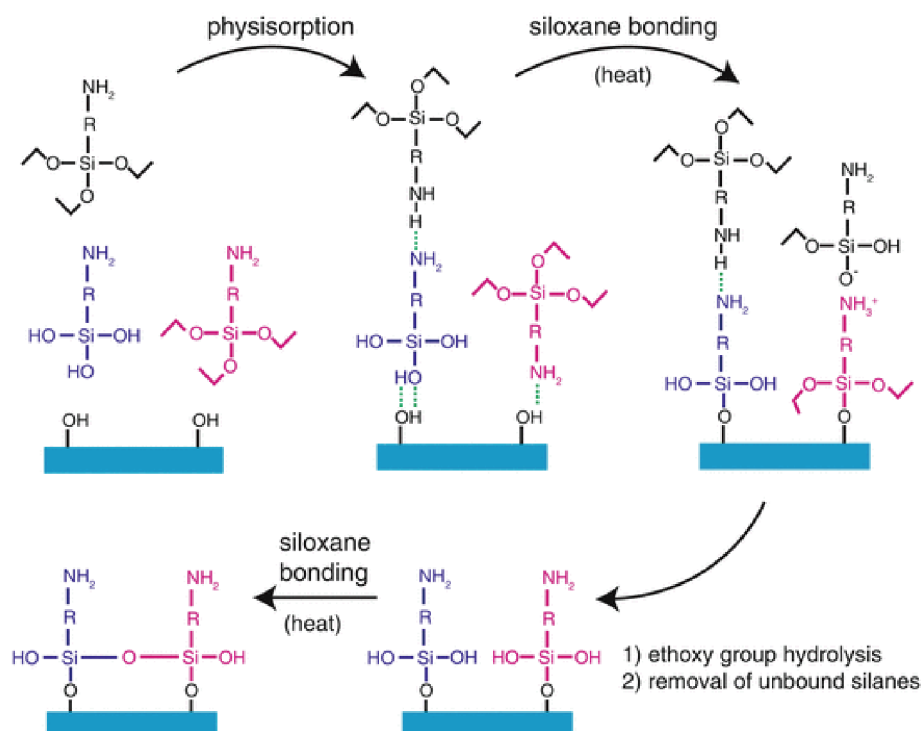


**Figure 4.1:** APTES functionalisation of glass. An appropriately cleaned glass surface containing a high density of silanol groups is exposed to aminosilane in nearly anhydrous acetone, yielding a diverse mixture of free silanes and silanols in solution, which then physisorb onto the surface via hydrogen bonding and/or ionic interactions (several configurations in addition to the ones shown are possible). The addition of heat drives the formation of siloxane bonds between the physisorbed silanes/silanols and the glass surface by supplying energy and removing condensation products (water and ethanol) by evaporation. This reaction is catalysed by the terminal amine group. Rinsing in ethanol and water removes any remaining physisorbed aminosilane deposits and leads to hydrolysis of remaining ethoxy groups on the bound silanes, converting them to silanols. A final heating/drying helps these silanol groups form intramolecular siloxane linkages (siloxane bonds may also form via reaction of adjacent ethoxy and silanol groups, as during the initial bonding to the surface). This conceptual scheme does not illustrate several concurrent pathways that also lead to stable binding of aminosilanes to the glass surface (e.g., aminosilane oligomerization in solution, followed by physisorption and binding to the surface). The final product of this treatment is a glass surface densely covered in covalently attached amines. Adapted from Nicholas *et al.*, 2014.<sup>109</sup>

## Mass Photometry

### Setup and instrument settings

Mass photometry was performed using a home-built microscope as previously described<sup>3,19</sup> and illustrated in Section 2.4. Instrument settings were as follows:

Laser wavelength: 520 nm, laser power: 300 mW, frame rate = 955 Hz, exposure time = 998  $\mu$ s, temporal averaging: 5-fold, pixel binning:  $4 \times 4$ , field of view:  $3.5 \times 10 \mu\text{m}^2$ . This leads to an effective frame rate of 191 Hz and an effective pixel size of 84.4 nm. All measurements were performed using flow chambers made by microscope cover glass and double-sided tape with 15  $\mu$ l sample per analysis. Flow chambers were first filled with a buffer blank to position the coverslip into the optimal focus position. Samples were then added to one side of the flow chamber and introduced by capillary flow with the aid of tissue paper to draw liquid into the chamber.

### **Data acquisition and analysis**

Data acquisition was started within 15 s of sample addition for a total of 120 s. In total, five replicates were taken for the double-stranded DNA ladder and three replicates for each single-stranded DNA sample. Data acquisition was performed using custom software written in LabView, generating a single movie file (.tdms) for further analysis. Three replicates were taken for the standard protein marker and five replicates were taken for the 100 bp double-stranded DNA ladder.

All acquired movies other than the DNA origami ones were processed and analysed using Discover MP v1.2.4 (Refeyn Ltd). The analysis procedure involved two fitting parameters for identifying landing events: (i) Threshold 1 related to a given particle contrast amplitude relative to the background and (ii) Threshold 2 related to the radial symmetry of the detected point spread function (PSF) of the same particle.

Analysis parameters for dsDNA and ssDNA samples are shown in Table 4.1. Threshold 1 was set to 1 to quantify smaller DNA (100 bp dsDNA and 155 nt ssDNA). In the presence of background due to buffer impurities or other contaminants, Threshold 1 was increased to 3 where necessary, which was

## 4.2. Materials and Methods

---

DNA sample	Number of binned frames, $n$	Threshold 1	Threshold 2
dsDNA ladder	8	1	0.2
ssDNA 155nt	8	1	0.2
ssDNA 4536nt	5	3	0.3
ssDNA 6048nt	5	3	0.3
ssDNA 7249nt	5	3	0.3
ssDNA 8064nt	5	3	0.3

**Table 4.1:** Analysis parameters for dsDNA and ssDNA samples

informed by running buffer blanks. For larger DNA samples, Threshold 1 = 1 provided effectively indistinguishable results to Threshold = 3, since changes in this value only affected the low size regime ( $< 300$  kDa). With Threshold 2, values were set to the default (0.2) and slightly greater values (0.3) were chosen for longer DNA strands to allow for any deformations of the PSF due to species exceeding the diffraction limit, resulting in a slightly asymmetric PSF. In the case of the linear dsDNA ladder, using the same Threshold 2 for analysing 100 and 2000 bp was not ideal, especially considering the size of 2000 bp dsDNA was approaching the diffraction limit. The shape of the PSF of a 2000 bp DNA became asymmetric. However, we found no evidence that the value of Threshold 2 has a measurable effect on the contrast of the landing event, either in DNA or protein measurements.

The output files contained a list of all detected particles within the analysed movie and their corresponding contrast values. The contrasts of all landing events were plotted as a scatter plot along the time axis. A histogram of the number of landing events and the contrasts was then generated. The resulting peaks were fit to a sum of Gaussians and the mean of the fitted peaks was taken as the contrast for each DNA component. The contrast to base pair ratio was determined by a linear fit. Base pair error was given as a deviation of the measured number of base pairs from the nominal number given by the

manufacturer. The contrast to nucleotide ratio and the nucleotide error for ssDNA was determined in a similar manner. The input values used to calculate the estimator bandwidth (`bw_method`) in the violin plots using the python package `matplotlib` (both the base pair error and nucleotide error) were set to 0.32.

Due to the asymmetry in the PSFs of the origamis, especially for the rod one which was 200 nm in length and 10 nm in diameter, the movies of DNA origamis were processed by custom-written Labview software instead of commercial DiscoverMP software. The data analysis workflow involved a thresholding approach, with two main thresholds, T and P. T was applied to the convolved image, resulting in a binary map of pixels with values greater than this threshold. The threshold T used in the origami experiments was set to be 0.008. From here, a particle probability (PP) image can be calculated as described by Yang *et al.*<sup>110</sup> A PP threshold can be set above which pixels are considered as candidate particles for fitting, with a value of 0.3 being typical and used for the analysis here. Then, a fitting routine, which allowed for different x and y widths, as well as a rotation of the PSF during particle capturing, was applied to the candidate particles. The output files contained a list of all detected particles within the analysed movie and their corresponding contrast values, as well as their x and y widths. A histogram of the number of landing events and the contrasts was then generated. The resulting peak was fit to a Gaussian function and the mean of the fitted peak was taken as the contrast for each DNA origami. The x and y widths were assigned to create a joint plot including a scatter plot with marginal histograms.

The estimation for the kernel function of the origami's PSF was done by assuming the PSF as a difference of two 2D Gaussian functions. The relative widths and amplitudes of the two were fixed by the ratio of the diameter of the

partial reflector to the diameter of the back focal plane of the objective, and by the transmission of the mask. The three parameters of  $a$ ,  $w$ , and  $s$ , which correlated to a measure of the mask strength, the width of the jinc function caused by the objective back aperture, and the width of the overarching Gaussian function which modulated the signal of the summed jinc functions, depend on the instrument used. These parameters were determined by measuring the standard protein marker MS1000 on the same mass photometer. Since the units of  $s$  and  $w$  were in pixels, they were multiplied by 84.4 nm per pixel before generating the 2D Gaussian kernel. In the simplest case, the brick-shaped and rod-shaped origamis were assumed to have the same density. Then, the discrete, linear convolution of the shape of the DNA and the gaussian kernel was generated. The estimated intensity of the simulated PSF was found as the PSF height at the PSF centre.

### **Diffusion correction and concentration measurements**

The relative abundance of each DNA fragment in the dsDNA ladder was calculated from the area of each Gaussian peak in the kernel density estimate (KDE) plot,  $a = A\sigma\sqrt{2\pi}$ , where  $a$  is the area,  $A$  is the maximum height at centroid and  $\sigma$  is the standard deviation of the fitted Gaussian. The contrast magnitude achievable with the 100 bp species approached the limit where the instrumental readout in terms of counting molecules is quantitative.

To account for differences in binding rates and thus molecule counts caused by varying diffusion speeds, we applied a correction to the measured mass distributions.<sup>3</sup> We assumed that the binding rate constant scales with the diffusion coefficient, which has been reported to be roughly proportional to  $bp^{-0.72}$  for DNA (i.e.,  $k_i = \alpha * bp^{-0.72}$ , where  $k_i$  is the binding rate constant for DNA component  $i$  and  $\alpha$  is a scaling factor).<sup>111</sup> We assumed that the scaling factor  $\alpha$  is constant for all DNA components. To estimate the scaling factor

$\alpha$ , an exponential function was fitted to the number of landing events vs time resulting in an average binding rate,  $k$ . The scaling factor was calculated as:

$$\alpha = \frac{k}{\langle bp \rangle^{-0.72}}$$

, where  $\langle bp \rangle$  is the average number of base pairs of all the DNA components in solution calculated based on the distribution of each DNA component,

$$\langle bp \rangle = \frac{\sum_{i=1}^N bp_i * a_i}{N}$$

, where  $bp_i$  is the number of base pairs and  $a_i$  the relative abundance measured experimentally of DNA component  $i$ , and  $N$  is the total number of species in solution.

To accurately estimate the proportion of each DNA fragment in solution, it is important to account for landing events that occur between the time when the sample is added ( $t_{addition}$ ) and when data acquisition starts ( $t_0$ ). We accounted for this by fitting the exponential decay of measured binding events from the addition of sample (from  $t_{addition}$ ) to completion of all sample binding ( $t = infinity$ ). Experimentally, we integrated from a given time  $t_0 = 15$  s after addition of sample up to a later time,  $t_{final} = 135$  s, when the acquired movie ended. Relating these two, the corrected intensity was given by:

$$a'_i = a_i \frac{e^{k_i t_0}}{1 - e^{-k_i(t_{final} - t_0)}}$$

, where  $a'_i$  is the intensity of DNA component  $i$  corrected over all time, and  $a_i$  is the experimentally measured abundance. The corrected mass distribution was then renormalised.

## 4.3 Results and Discussion

### 4.3.1 Quantifying DNA Contour Length

The operating principle behind MP is based on accurately measuring the change in reflectivity of a glass-water interface caused by interference between light

scattered by a molecule binding to the interface and light reflected at that interface (Figure 4.2A). To test the applicability of MP to a representative DNA sample, we started with an analysis of a standard low mass dsDNA ladder. A 9 nM solution diluted in the buffer (5 mM Tris, 10 mM MgCl<sub>2</sub>, pH 8) led to distinct molecular binding events with clearly varying molecule-to-molecule contrasts (Figure 4.2A), while frequent unbinding events were observed on non-APTES coverslips (Figure 4.3A), suggesting that appropriate surface charge was required to achieve tight surface binding. The contrast histogram of the landing events on non-APTES coverslips showed very poor resolution (Figure 4.3B). As for signals collected on APTES coverslips, a scatter plot of these signals obtained by quantifying the signal magnitude for each individual binding event exhibited six clear bands, as expected from the ladder used (Figure 4.2C). This separation persisted upon binning into a contrast histogram, with baseline resolution from the second peak onwards. The observed spacing and knowledge of the ladder composition allowed for assignment to different contour lengths by inspection (Figure 4.2B, C). These results demonstrate that MP can detect single DNA molecules without labels with a comparable performance in terms of mass sensitivity and resolution to polypeptides.

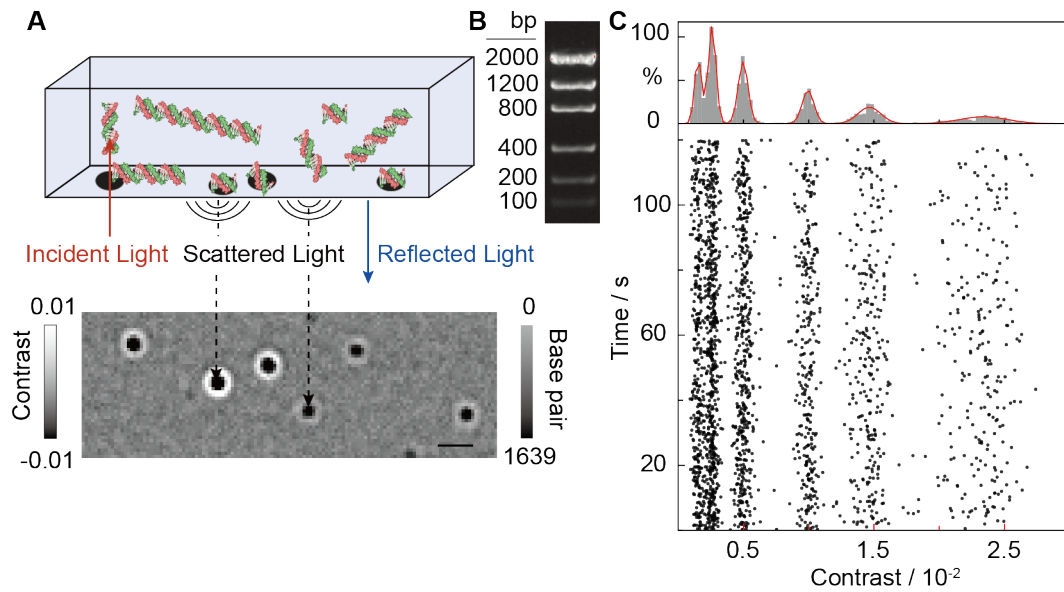


**Figure 4.2:** Quantifying DNA length by mass photometry (A) Working principle of label-free DNA detection and quantification by mass photometry. Individual DNA molecules diffusing in solution bind to an appropriately charged glass surface. Binding events cause changes to the reflectivity of the interface, visualized by a contrast-enhanced interferometric scattering microscope through the interference between scattered and reflected light. Scale bar: 1  $\mu\text{m}$ . (B) Agarose gel image of a low mass dsDNA ladder. (C) Scatter plot and resulting contrast histogram (with corresponding kernel density estimate shown in red) obtained by quantifying the image contrast on a molecule-by-molecule basis for the low mass dsDNA ladder. The close correspondence between the gel and resolvable features in the contrast histogram allows for assignment by inspection.

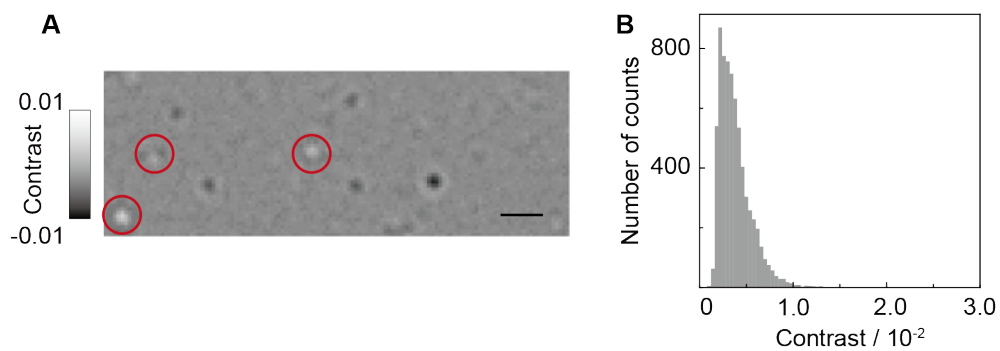


**Figure 4.3:** (A) Image of dsDNA ladder binding to a regular glass coverslip and (B) its associated histogram. The unbinding events are circled red. Scale bar: 1  $\mu\text{m}$ .

### 4.3.2 Resolution and Relative Concentration Measurements

Quantifying the landing frequency should provide direct information on molecular concentration for each species assuming label-free, universal detection of all binding events. Multiple repeats of the ladder experiment exhibited high reproducibility (7.7% RMS) in the total number of detected molecules, despite the simplicity and inherent variability of the measurement due to manual sample addition and timing when recording was started (Figure 4.4A). The relative fluctuations between the peak areas amounted to  $12 \pm 3.3\%$  RMS (Figure 4.4B, blue dots).

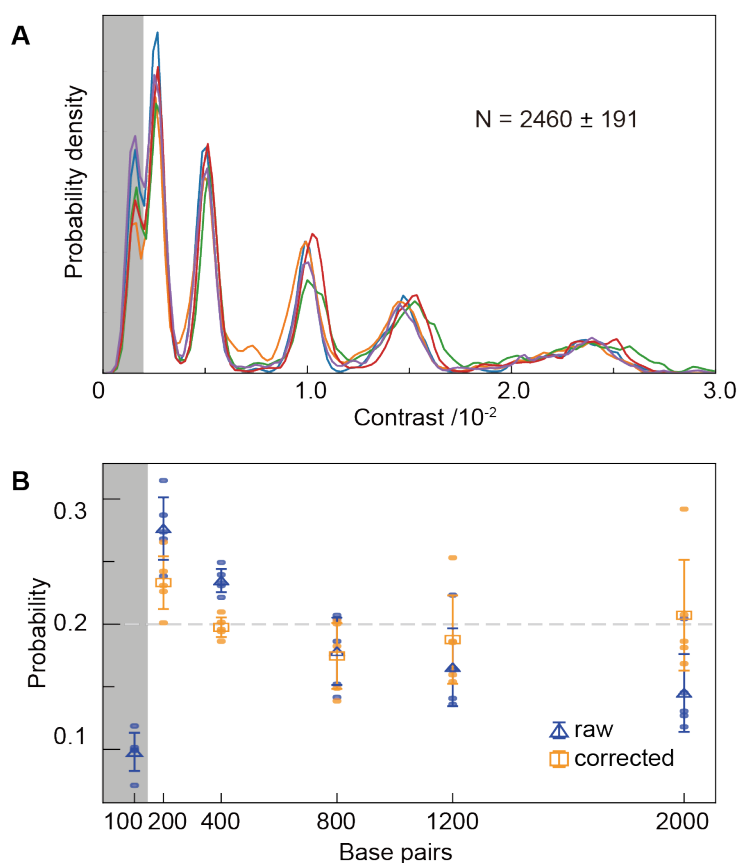


**Figure 4.4:** Achievable concentration precision. **(A)** Reproducibility of individual MP measurements of the same dsDNA ladder sample. The plots were generated from mass histograms using a Kernel Density of width  $2.1 \times 10^{-4}$ . **(B)** Extracted mole fractions before and after correction for length-dependent diffusion.

Despite the fact that the ladder contains an equimolar mixture of molecules, we observed clear variations in peak areas with a drop towards larger species. The landing frequency of molecules with the surface, and thus detection rate, however, is not only a function of solution concentration, but also diffusion coefficient, which decreases considerably with contour length.<sup>111</sup> Our qualitative observation of a decrease in binding events with contour length agreed with this expectation.

To account for these differences, we needed to relate the number of molecules that have bound during our finite measurement window to the number we would have observed for an infinite observation time where all molecules would be depleted from solution by surface binding (Figure 4.5A). Since smaller molecules diffuse more quickly, more of them will be removed from solution initially, resulting in a concentration difference once the measurement was started, after sample application, compared to the original solution.<sup>3</sup> We therefore applied a correction factor to account for sampling occurring before and after the recorded measurement. The duration of the measurement itself also influenced how the correction is applied, such as with longer movies, which will change the balance towards longer DNA (Figure 4.5B, C). Correcting for this behaviour increased the amount of large relative to small molecules (Figure 4.4B, orange dots), in this case resulting in effectively equimolar concentrations for all species of contour length 200 bp or larger. The lower than expected concentration of 100 bp species was most likely caused by non-unity detection efficiency as discussed previously.

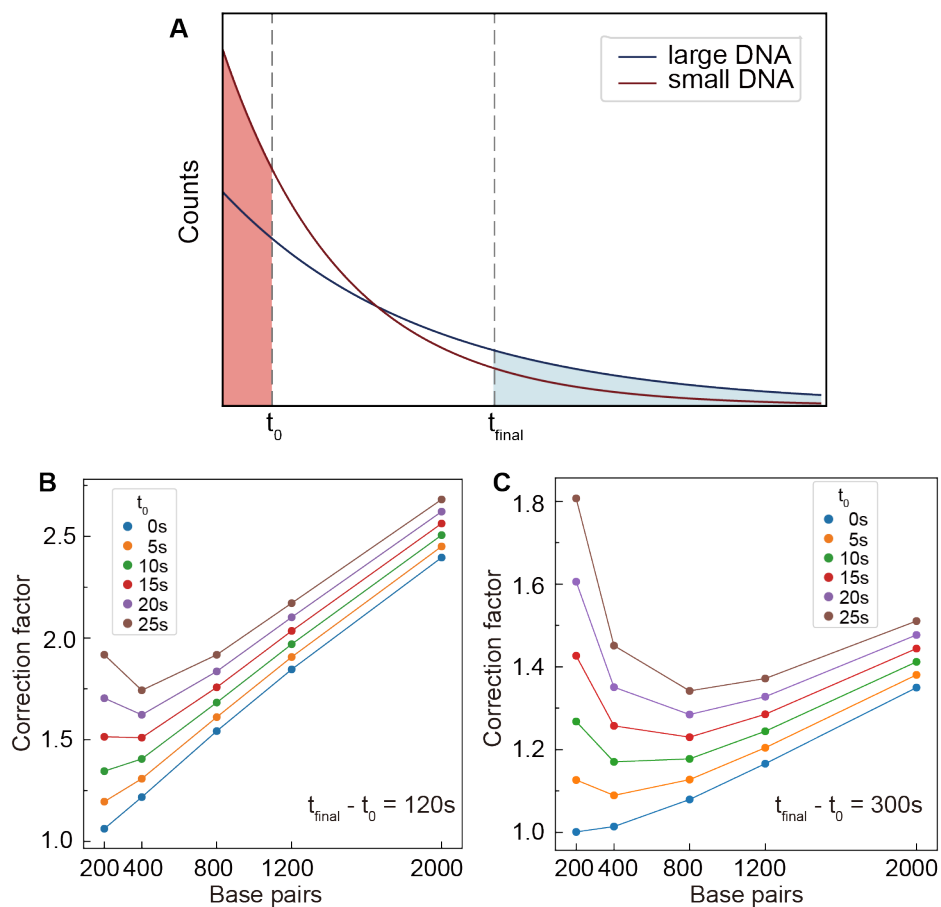


**Figure 4.5:** Comparison of diffusion correction as a function of strand length. **(A)** Exponential decay of the binding frequency for both large DNA strands and small DNA strands starting nominally at the same concentration. The later the mass photometry recording begins ( $t_0$  is larger), more small particles are lost before the measurement starts (i.e. the red area becomes larger), resulting in larger correction factors for short vs long DNA. By contrast, in longer movies ( $t_{final} - t_0$  is larger), one would collect more long DNA strands relative to the short ones (blue area gets smaller), resulting in a relatively smaller correction factor for large DNA. **(B)** Correction factors when  $t_{final} - t_0$  is 120 s.  $t_0$  ranges from 0 s to 25 s. **(C)** Correction factors when  $t_{final} - t_0$  is 300 s.  $t_0$  ranges from 0 s to 25 s.

Careful inspection of the obtained mass distribution in Figure 4.4A revealed a clear variation in peak width with molecular size, with lower widths for small species and much larger widths for large species compared to globular proteins producing similar imaging contrast (Figure 4.6A). These results point towards a variability in contrast for dsDNA possibly due to binding events occurring with different conformations, and thus effective density and polarisability,

which determines the magnitude of the detected signal in an interferometric measurement<sup>18</sup>. Another possible explanation for the observed differences in peak widths for similar optical contrast may be due to molecules occupying different areas on the surface in a way that becomes significant ( $> 50$  nm) for our interferometric measurement in the light of the diffraction limit (200 nm), and the comparatively high spatial confinement of oligomeric proteins ( $\ll 50$  nm). We would expect this effect to become relatively more pronounced for longer DNA molecules in the light of the persistence length of DNA ( $\sim 150$  bp,  $\sim 50$  nm). This expectation is in line with our observations that the peak widths increase significantly with the lengths of DNA, especially for DNA larger than 800 bp. Additionally, as several properties of DNA under torsional constraint, in particular aspects of DNA supercoiling, are known to strongly depend on salt concentration<sup>112,113</sup>, we expect that the peak width will also be affected by the salt concentration. Similarly, the reduced width for small species ( $< 400$  bp) can be explained by a comparatively lower degree of disorder in terms of structure and thus polarizability given the structural rigidity of DNA on short length scales compared to globular proteins binding non-specifically to a glass surface. Such variability in surface adhesion agrees with observations of DNA conformations on mica surfaces observed by AFM (Figure 4.6B)<sup>114, 115</sup>.

### 4.3.3 Characterization of Nucleotide Accuracy and Precision

The observed peak spacing roughly matched the spacing expected for a direct proportionality between the MP contrast and the number of base pairs. To quantify this correlation, we repeated these measurements 5 times, finding almost perfect correspondence ( $R^2 = 0.9998 \pm 0.0001$ ) for all species up to 1200 bp, with a slightly lower than expected contrast for the largest (2000 bp) species (Figure 4.7A). Given that the repeats were performed on different substrates,

### 4.3. Results and Discussion

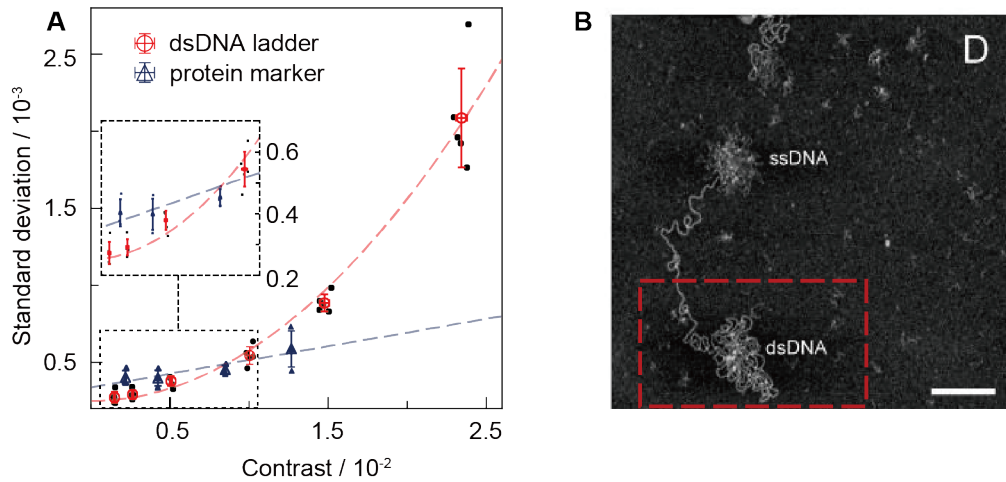


**Figure 4.6:** Resolution. (A) Comparison of contrast resolution between dsDNA and a globular protein mixture of comparable imaging contrast for the same instrument. (B) AFM image of heated Lambda dsDNA on mica modified by APTES. Scale bar: 250 nm. B is adapted from Adamcik *et al.*, 2006.<sup>115</sup>

these results demonstrate the high repeatability of the measurement, in line with our original results on globular proteins.<sup>3</sup> The resulting conversion from imaging contrast to contour length amounts to  $1.22 \pm 0.02 \times 10^{-5}$  /bp (i.e., contrast-to-mass ratio:  $1.88 \pm 0.03 \times 10^{-5}$  /kDa) for dsDNA. Applying this conversion factor to each individual measurement allowed us to determine the average base pair error, which amounted to  $1.8 \pm 13$  bp up to 1200 bp, with slight variations as a function of molecular size (Figure 4.7B). Characterizing another commercial dsDNA ladder showed a contrast-to-bp ratio of  $1.20 \pm 0.02 \times 10^{-5}$  /bp (i.e., contrast-to-mass ratio:  $1.85 \pm 0.03 \times 10^{-5}$  /kDa), which was within the experimental error of our initial measurements (Figure 4.7C,D). At this stage, it is unclear to which degree the observed error is indeed representative of the limits achievable by MP or whether they are caused by sequence-specific variations in molecular mass or molecular polarizability, which we could not account for given that the sequence of the ladder components was unknown.

Repeating the same process with ssDNA revealed a similar linear relationship between the number of bases and the imaging contrast, without noticeable

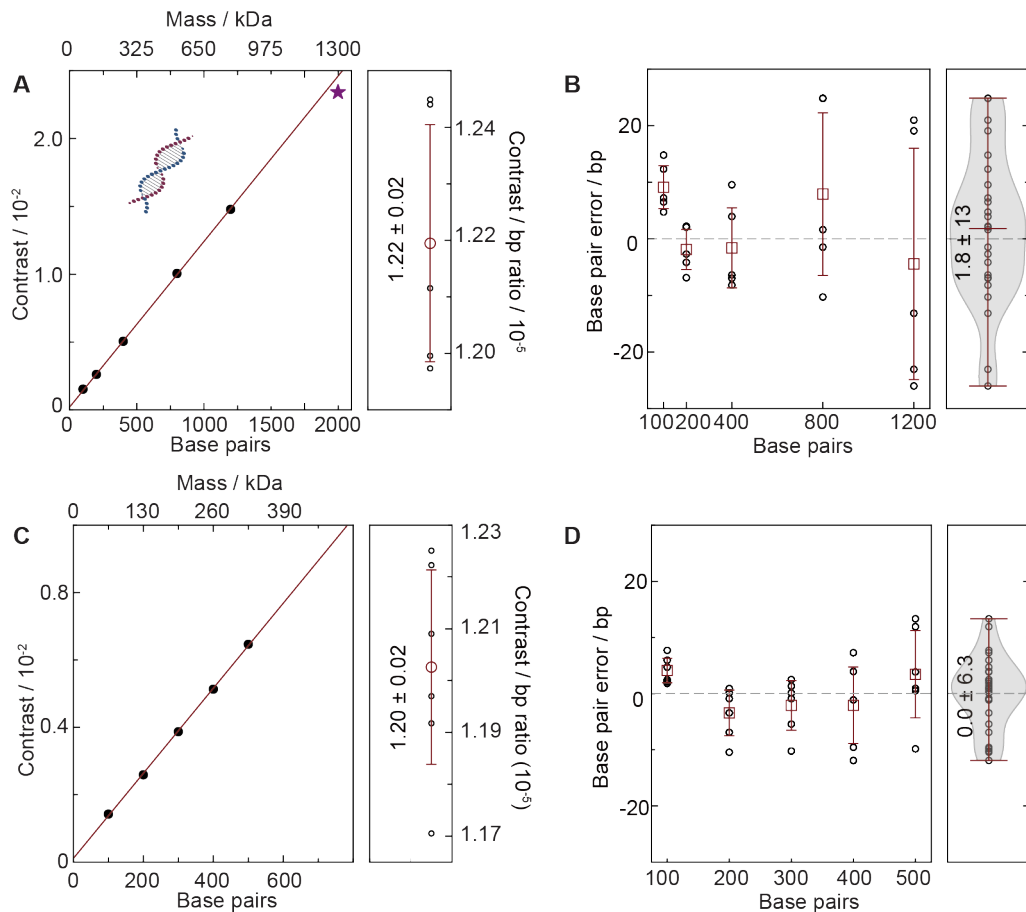


**Figure 4.7:** Characterization of nucleotide accuracy and precision for dsDNA. **(A)** Correlation between imaging contrast and number of basepairs. The 2000 bp data point (star) was omitted for the calibration due to the molecular size becoming comparable to the diffraction limit (200 nm). **(B)** Resulting base pair accuracy for independent measurements using the average contrast-to-bp conversion. **(C, D)** Equivalent measurements for a second 100 bp dsDNA ladder. Peaks were observed at 100 bp, 200 bp, 300 bp, 400 bp and 500 bp. Larger species in the ladder were not detected because their concentrations in the ladder were too low in comparison.

### 4.3. Results and Discussion

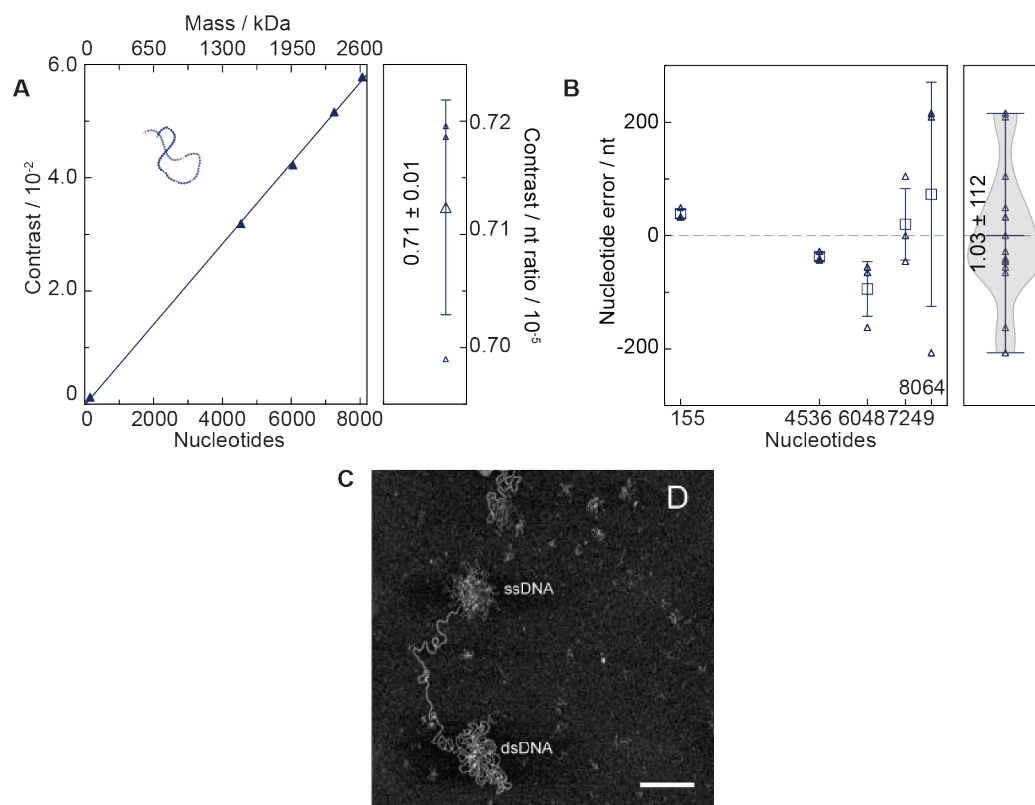


**Figure 4.8:** Characterization of nucleotide accuracy and precision for ssDNA. **(A)** Correlation between imaging contrast and nucleotides. **(B)** Resulting nucleotide accuracy for independent measurements using the average contrast-to-nt conversion. **(C)** AFM image of heated Lambda dsDNA adsorbed on the surface of mica in the presence of 5 mM  $\text{Mg}^{2+}$ . Scale bar: 250 nm. C is adapted from Adamcik *et al.* 2006.<sup>115</sup>

deviations for larger species (Figure 4.8A). The associated average nucleotide error of  $1 \pm 112$  nt was much larger (Figure 4.8B), although this is may have been partially caused by the requirement to run separate experiments for each species, rather than mixtures as for dsDNA due to insufficient sample purity. Converting the contrast-to-nt ratio ( $0.71 \pm 0.01 \times 10^{-5}$  /bp) to contrast-to-mass ratio for of ssDNA resulted in  $2.18 \pm 0.03 \times 10^{-5}$  /kDa, which was slightly larger than dsDNA. This was likely because of a higher effective density of ssDNA in the presence of  $\text{Mg}^{2+}$  arising from increased flexibility or polarizability in the absence of basepair hybridization (Figure 4.8C).<sup>115</sup> The lack of non-linear contrast behaviour even for very long ssDNA molecules was likely due to the

fact that ssDNA becomes highly compacted under the buffer conditions used, ensuring essentially uniform densities for all studied species irrespective of the number of bases in contrast to dsDNA, where the contour length of DNA played a non-negligible role.

#### 4.3.4 MP Contrast vs. DNA Shape

Analysing the MP results of the two DNA origamis of the same mass (4.5 MDa) by custom-written Labview software which allowed for flexibility in x and y widths and the rotation of the PSF during particle capturing, we found differences in their contrasts. The contrast of the brick-shaped origami was found to be 1.27 times higher than that of the rod-shaped one (Figure 4.9A).

To understand whether this contrast difference was actually due to the shape variation, we simulated the kernel function of the PSF based on the longest axis of each origami, and by assuming the same density of the two. Given that the rod-shaped origami is 200 nm long and the bricked-shaped one is 20 nm long, the PSF intensity of the brick-shaped one, which is found as the PSF height at the PSF centre, is 1.16 times larger than that of the rod-shaped one (Figure 4.9B). This estimation agrees with the experimental result. In addition, the peak of the 2D Gaussian function used to fit the PSF of the brick origami is slightly narrower than that of the rod one along the length of the molecule (Figure 4.9B). This also matches the observation that brick-shaped origami has narrower distribution in its x and y widths (Figure 4.9C) than the ones of rod-shaped origami (Figure 4.9D). At this stage, one could only tell that the PSF affected by the shape of the molecule can make a difference in the contrast of the sample. However, due to the size of the rod-shaped origami almost exceeding the diffraction limit (200 nm), it is difficult to conclude whether the contrast variation is caused by distinct optical

#### 4.4. Conclusion and Outlook

---

properties of molecules that have different shapes, or to predict the exact levels of sensitivity of MP contrast to structural details.

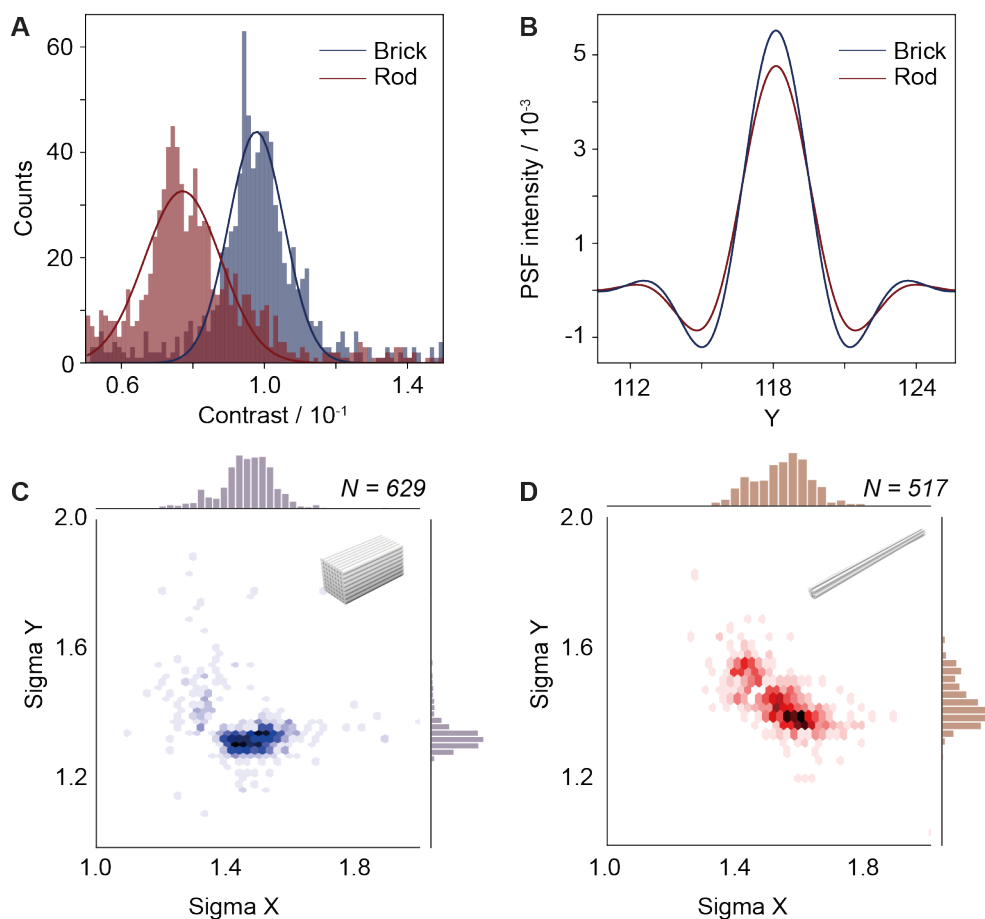


**Figure 4.9:** MP Contrast vs. DNA Shape. (A) Contrast histograms and gaussian fittings of two DNA origamis of the same mass (4.5 MDa). (B) Simulated PSF estimation for both origamis based on their longest axis. (C), (D) The joint plots show the scatter plots and histograms of x and y widths of brick-shaped and rod-shaped origamis' PSF. The insets illustrate the structures of the brick-shaped and the rod-shaped origami, which have their longest dimension at 20 nm and 200 nm, respectively. N indicates the number of events detected at the selected contrast range.

## 4.4 Conclusion and Outlook

Taken together, these results establish mass photometry as a novel analytical approach for studying nucleic acids, with a range of potential future analytical applications, albeit with some intrinsic limitations. Base pair resolution will

likely never reach that achievable with electrophoretic methods, but the solution operation of MP provides much potential for combination with such approaches in the future to improve the resolution beyond what can be achieved by manual sample addition. The ultimately achievable basepair accuracy is generally subject to the underlying mechanism responsible for the optical contrast we measure, which is the molecular polarisability. This, in turn, depends on the optical properties of the scatterer, as well as that of its environment, which can become complex especially on the nanoscale. As a result, it is in principle possible that errors would arise due to factors such as the level of guanine-cytosine content, whether DNA is nicked, supercoiled, or circular, as well as effects due to variations in secondary structure. All of these factors may indeed limit the performance of MP for how accurately unknown samples can be characterized, which will require a more in-depth study encompassing a much broader set of samples.

Notwithstanding these limitations, there remain a number of unique advantages of MP for studying nucleic acids and their interactions. We have demonstrated the relative concentration measurements based on molecular counting with comparable precision to UV-absorption based approaches, but with the specific advantage of operation at low concentrations (nM) and minimal sample requirements, currently only limited by our sample delivery approach. The observed base pair accuracy of 2 bp is comparable to unreferenced capillary electrophoresis, and could be in principle improved further by using appropriate internal standards. Furthermore, mass photometry has proven surprisingly robust to even quite significant variations in molecular identity, while showing fairly little sensitivity to structure, such as quantifying changes in the number of lipids in lipid nanodiscs.<sup>3</sup> Our observation of comparable contrast-to-mass ratios between proteins ( $2.35 \pm 0.01 \times 10^{-5}$  /kDa) and DNA

#### 4.4. Conclusion and Outlook

---

(ss:  $2.18 \pm 0.03 \times 10^{-5}$  /kDa, ds:  $1.88 \pm 0.03 \times 10^{-5}$  /kDa) confirms this rough assessment (Figure 4.10), meaning that DNA and polypeptides can be simultaneously quantified with a mass accuracy sufficient for many applications aimed at protein-DNA interactions, in particular when separate calibrations are available. It is also and has so far been largely insensitive to molecular structure, e.g. when comparing molecules of very different shapes such as largely spherical proteins with antibodies.<sup>4</sup> While it is difficult at this stage to predict the exact levels of sensitivity of MP contrast to structural details, the linearity of contrast with the number of nucleotides presented herein is in line with the accuracy limits of MP ( $\sim 2\%$  of object mass) irrespective of molecular shape or conditions.

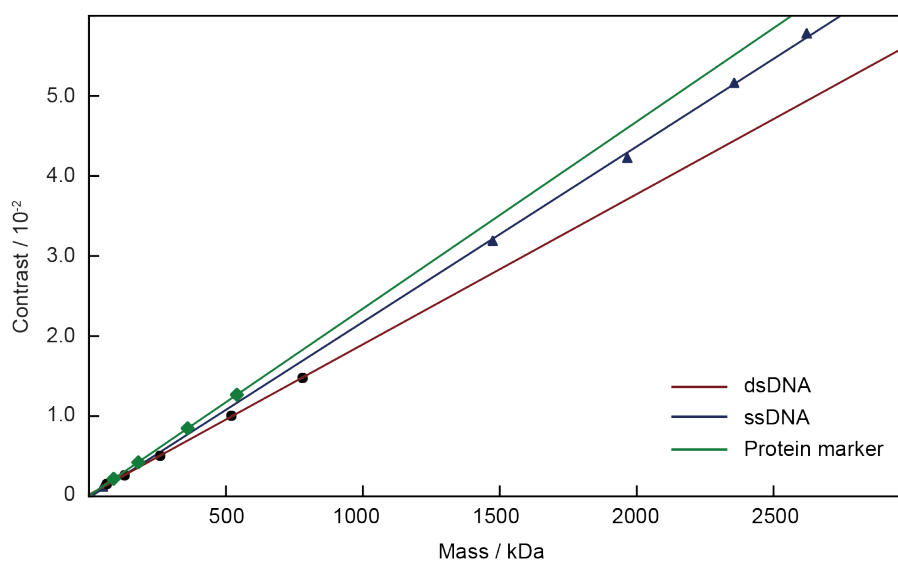


**Figure 4.10:** Correlation between imaging contrast and molecular mass.

Given the single molecule nature of MP, coupled with its intrinsic compatibility for visualizing and quantifying proteins, and suitability for combination with single molecule fluorescence imaging,<sup>58</sup> MP is likely to become a powerful addition to the existing toolbox of single molecule methodologies aimed at

quantifying and studying nucleic acids and their interactions.

#### 4.4. Conclusion and Outlook

---

# Chapter 5

## ATP Drives Loop Extrusion by Modulating the Affinity of Cohesin to DNA

### 5.1 Introduction

The small size of the cell and the large size of genome suggest that genomic DNA has to exist in a highly folded state. In a human cell, 2 m of DNA is highly compacted in the approximately 10  $\mu\text{m}$  nucleus into a nucleoprotein structure called chromatin, which is hierarchically folded into several layers of higher-order structures.<sup>116</sup> Apart from the physical confinement of the genetic information into such a small volume, the condensation and spatial organisation of DNA are highly regulated across space and time, and have impacts on all DNA-based processes: transcription, replication and DNA repair.<sup>117</sup> DNA condensation is achieved by DNA-protein interactions, which can bend DNA, bridge between distant sections or create inner loops. At the molecular level, folding begins with wrapping of DNA around core histones, forming a nucleosome fiber (10 nm fiber).<sup>118,119</sup> Recent reports using high-throughput chromosome conformation capture (Hi-C) and chromosome conformation capture carbon copy (5C) methods to investigate the three-dimensional architecture of genomic DNA within cells proposed higher order structures of interphase chromatin, which were

termed as the “topologically associating domains (TADs)”.<sup>120</sup> Studies suggest that these TADs contribute to gene regulation and recombination.<sup>120–122</sup> The folding behavior of genomic DNA is supported by an active extrusion process, which is mediated by structural maintenance of chromosomes (SMC) protein complexes.<sup>123,124</sup> SMC complexes, including condensin, cohesin and SMC5-SMC6 complexes, are DNA and chromosome binding ring-shaped ATPases (adenosine triphosphatase), which are found in all kingdoms of life.<sup>125</sup>

### **Cohesin as a Member in the Family of SMC Complexes**

Cohesin was initially discovered for its ability to physically connect replicated DNA molecules<sup>126,127</sup> (Figure 5.1B). Cohesin promotes sister chromatid cohesion following DNA replication by topologically entrapping two DNA segments.<sup>128,129</sup> In addition, recent single-molecule studies combined with the use of biochemical reconstitution have shown that in the presence of the NIPBL-MAU2 complex, cohesin can extrude DNA into loops with high speed at kilobases per second, in a manner that depends on cohesin’s ATPase activity<sup>130,131</sup> (Figure 5.1C). In contrast to topological loading, cohesin is able to extrude DNA loops if all three cohesin ring interfaces are covalently closed,<sup>130</sup> suggesting that loop extrusion does not involve topological DNA entry into the cohesin ring.

The human cohesin complex usually consists of 5 subunits: SMC1, SMC3, Scc1, STAG1 and NIPBL (Figure 5.1A). SMC1 and SMC3 together form a heterodimer via a hinge domain while on the other side, both subunits contain head domains, which can bind and hydrolyse two molecules of ATP. The hinge and head domain are separated by a coil domain. Binding of a kleisin protein, Scc1 (also known as RAD21 or Mcd1), to this dimer, links the SMC head domains, thereby stabilising the SMC interaction and generating a large (~ 40 nm), ring-like trimer. The kleisin N-terminus of Scc1 reversibly engages

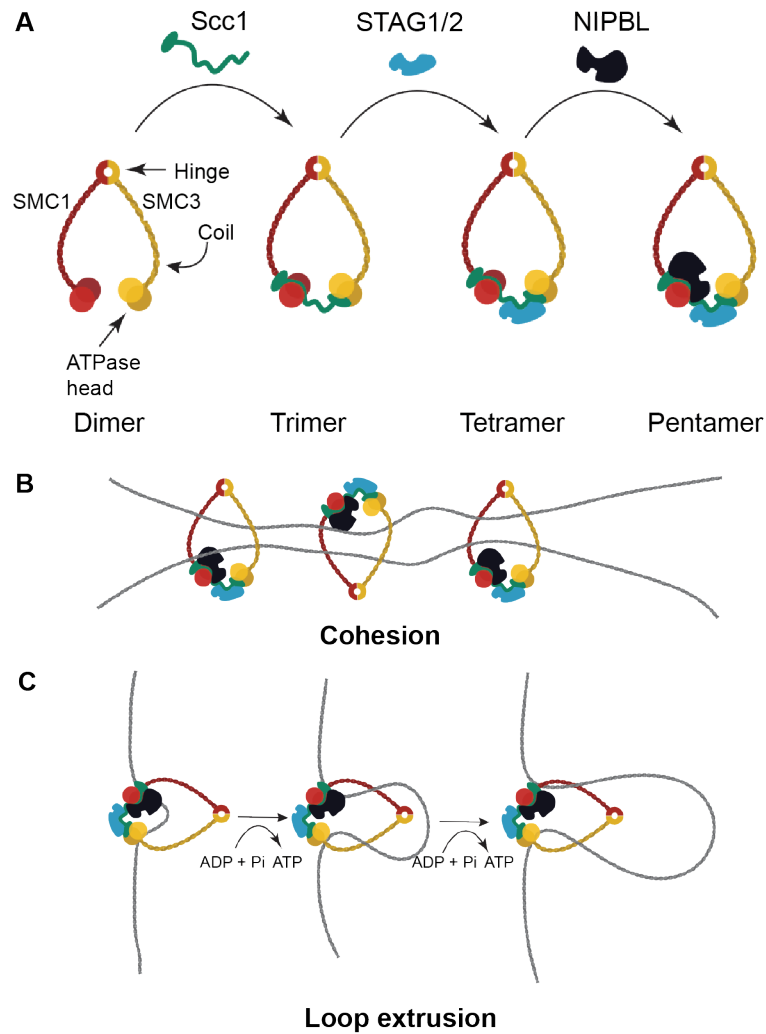


**Figure 5.1:** (A) Architecture of human cohesin complexes. (B) Sister chromatid cohesion. (C) DNA loop extrusion.

with the SMC3 coiled coil next to the ATPase head, forming the kleisin N-gate through which DNA enters the cohesin ring.<sup>132</sup> The kleisin C-terminus in turn binds to the SMC1 head domain. STAG1/2 (also known as SA1/2, or Scc3) binds tightly to this trimer to form a stable tetramer, the predominate species isolated from cells. NIPBL (also known as Scc2), together with its binding partner MAU2 (also known as Scc4), transiently associates with kleisin between the kleisin N-gate and STAG1. Once cohesin loading onto DNA is complete, NIPBL-MAU2 is replaced by a related HEAT repeat subunit, Pds5.<sup>133</sup> Because of its transient role, NIPBL-MAU2 is often thought of as a cofactor, called

“cohesin loader”.<sup>134</sup>

### **Models of Loop Extrusion by Cohesin**

Despite the key roles in sister chromatid cohesion and chromosome organisation, the mechanism by which cohesin rings are loaded onto DNA and extrude DNA loops are still unclear. To extrude DNA into loops, one might expect that cohesin contains multiple DNA binding sites, to be able to reel in DNA while simultaneously holding onto both arms of the forming loop. There are five DNA binding sites found in the human cohesin complex, including the hinge domain, two SMC head domains, STAG1 and NIPBL. Recent cryogenic electron microscopy (cryo-EM) structures show that all these DNA binding sites of cohesin can interact with DNA in a DNA-bound state (gripping state).<sup>132,135</sup>

If cohesin uses its DNA binding sites to reel DNA into loops, the subunits containing these sites may change conformations and DNA affinities during loop extrusion. Experiments performed by electron microscopy (EM) and atomic force microscopy (AFM) show that SMC complexes can exist in a number of different conformations.<sup>136</sup> Open-ring conformations of cohesin and condensin, in which the coiled coils are separated, have been observed with either disengaged or engaged ATPase heads.<sup>123,137</sup> Rod conformations, in which the coiled coils are aligned, as well as bent conformations, in which the coiled coils are folded and the hinge domain is proximal to ATPase heads, have also been observed previously in various SMC complexes.<sup>138–140</sup>

Several models have been proposed to explain how SMC complexes extrude DNA loops.

In the “walking” or “tethered inchworm” model,<sup>142,143</sup> the hinge domain serves as the anchor, and the two HEAT subunits (NIPBL and STAG1) are recognised as DNA binding elements, which perform a scissoring motion while

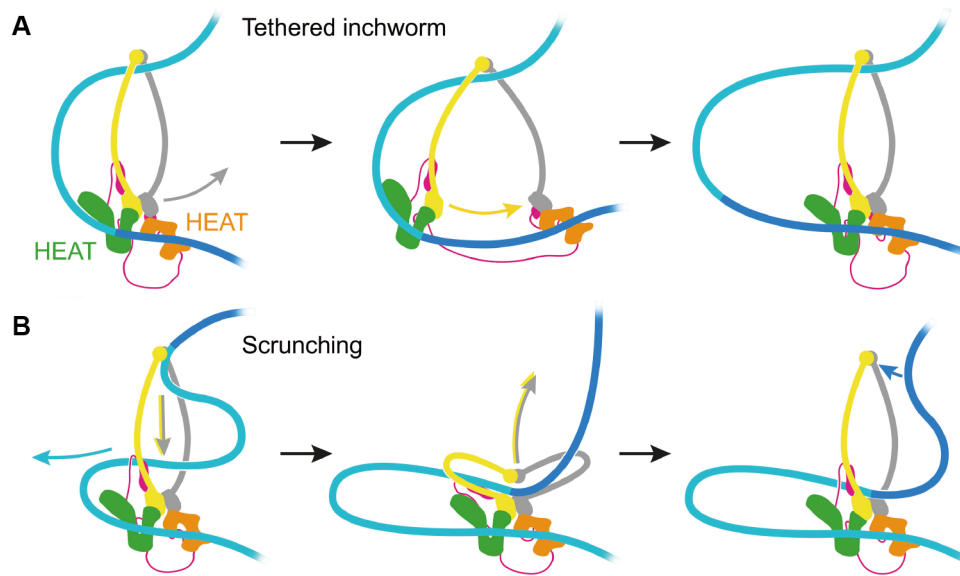


**Figure 5.2:** Models for loop extrusion by SMC complexes. **(A)** The tethered inchworm model, in which the two HEAT-repeat subunits (HEAT) step along the DNA. **(B)** The scrunching model suggests that the hinge captures DNA and hands it over to the heads to enlarge the loop. Adapted from Higashi and Uhlmann, 2022.<sup>141</sup>

remaining connected by a flexible kleisin linker (Figure 5.2A). During the ATP hydrolysis cycle, DNA affinities of the HEAT subunits are thought to alternate, leading to the two heads stepping along the DNA, similar to how cytoskeletal motor proteins move along microtubules. Loop extrusion has been observed with cohesin and condensin that contain HEAT subunits connected by flexible kleisins, but not with prokaryotic or SMC5–SMC6 complexes which contain two conjoined Kite DNA binding elements instead of HEAT subunits.<sup>144,145</sup> The difference in eukaryotic and prokaryotic SMC complexes is consistent with the idea of HEAT subunits as the moving elements. However, while in the presence of microtubules, *D. melanogaster* kinesin and yeast dynein can hydrolyse up to 25 and 38 ATP molecules per second,<sup>146,147</sup> yeast condensin and human cohesin hydrolyse only up to two molecules of ATP per second in the presence of DNA.<sup>130,148</sup> Single-molecule translocation rates also differ by around one order of magnitude.<sup>149</sup> Furthermore, the polarity of the microtubule

determines the directionality of kinesin translocation, which cannot be the same for the translocation of SMC complexes along the phosphate backbone of DNA. Therefore, even though SMC complexes indeed move along DNA during extrusion, the reaction mechanism is likely different from the one used by microtubule motors.<sup>136</sup>

Based on the observation that SMC complexes can exist in bent or scrunched conformations, where the hinge and ATPase heads are in close proximity, the “scrunching” model is proposed (Figure 5.2B).<sup>150</sup> Thermal fluctuations between DNA binding sites at the head and hinge form the basis for loop formation and extrusion. The model predicts DNA is captured by the hinge in the unfolded state, and released in the ATP-bound state because folding of the coiled coils might alter the conformation of the hinge and thus might affect its affinity for DNA.

A variant scrunching mode, “swing and clamp” model is proposed on based on the analysis by protein engineering and mutagenesis in conjunction with single-molecule experiments (Figure 5.3).<sup>151</sup> Bauer *et al.* have identified DNA binding sites and large-scale conformational changes that are required for loop extrusion as well as how these are coordinated. Their results suggest that DNA is translocated by a spontaneous 50 nm swing of cohesin’s hinge, which hands DNA over to the ATPase head of SMC3. Upon binding of ATP, DNA is clamped by NIPBL. During this process, NIPBL “jumps ship” from the hinge toward the SMC3 head and might thereby couple the spontaneous hinge swing to ATP-dependent DNA clamping. Although essential for loop extrusion, the molecular function of STAG1 in this process has not been determined in this particular model. Furthermore, DNA translocation has not been measured or visualised directly in the study, and it remains unknown how DNA is transferred from the SMC3 head to the SMC1 head upon ATP hydrolysis and

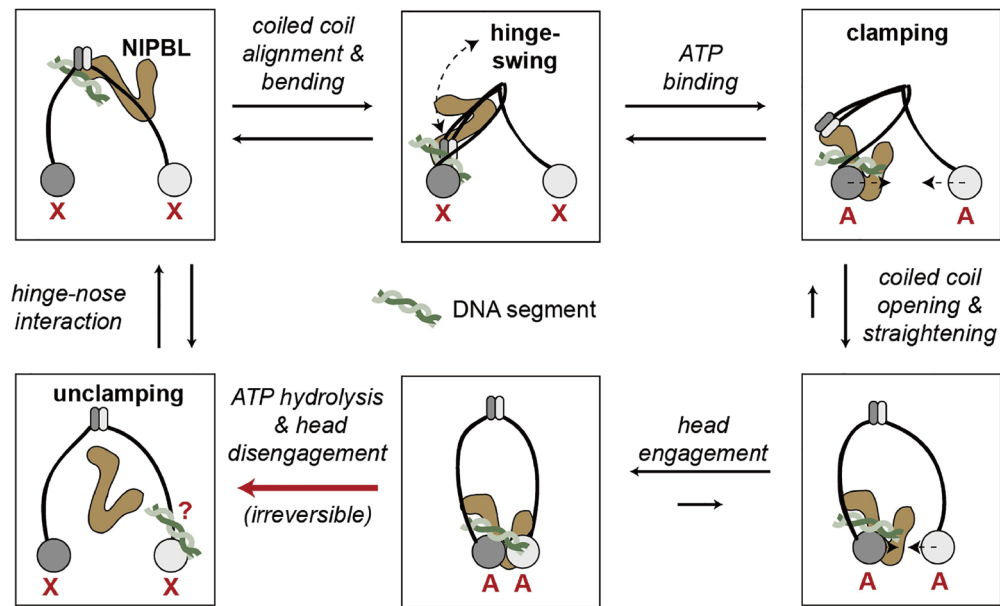


**Figure 5.3:** “Swing and clamp” model of DNA translocation. In the nucleotide free state (“X”), NIPBL interacts via its nose with the hinge. Bending moves the hinge together with NIPBL to the SMC3-head. Upon ATP-binding (“A”), the body of NIPBL forms a clamp with the SMC3 head, inducing the engagement of the heads. The hinge dissociates from the nose and the coiled coils stretch. The engagement of the heads triggers ATP hydrolysis and results in dissociation of the clamp and disengagement of the heads, resetting cohesin for the next cycle. The proposed pathway of a DNA stretch from the hinge to the SMC3 head is indicated. At the end of one cycle, the DNA segment may be transferred to the SMC1 head. Adapted from Bauer *et al.*, 2021.<sup>151</sup>

head disengagement.

It is also possible that DNA is translocated into the opposite direction (i.e., from the ATPase heads toward the hinge), as has been proposed in the “Brownian ratchet model” (Figure 5.4).<sup>152</sup> In this model, there are two DNA binding modules, one as the “NIPBL-head module” and the other as the “STAG1-hinge” module.<sup>152</sup> After DNA arrives in the gripping state without passing the kleisin N-gate, upon ATP hydrolysis, the NIPBL-head module turns into the DNA slipping state, but the kleisin path prevents DNA from passing between the ATPase heads. The STAG1-hinge module uncouples from the NIPBL-head module, but now its diffusion-driven swinging motion cannot steer DNA through the head gate. The only way for the STAG1-hinge module

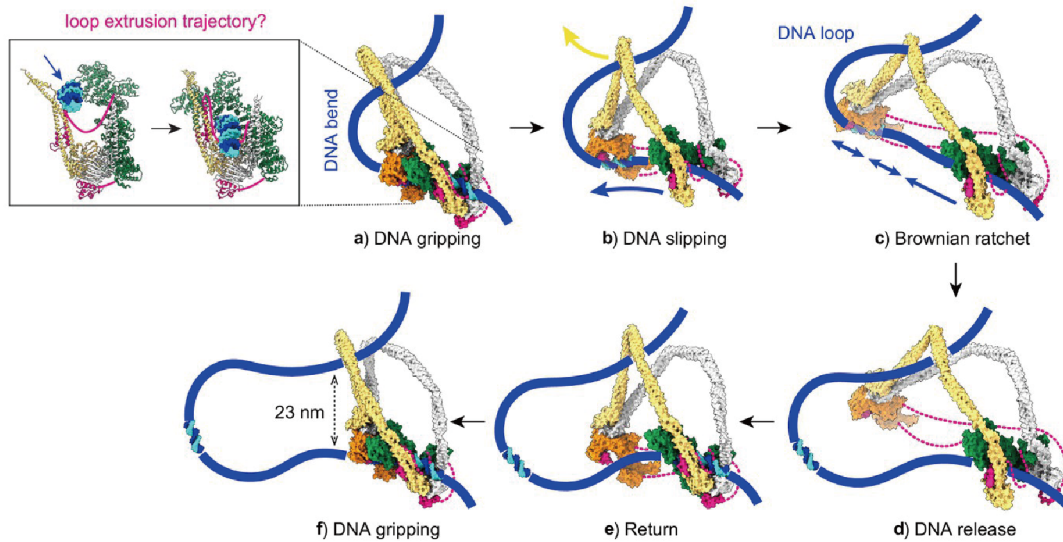


**Figure 5.4:** “Brownian ratchet model” for loop extrusion. (a) DNA arrives in the gripping state without passing the kleisin N-gate. (b) ATP hydrolysis leads to SMC head gate opening, but the kleisin path prevents DNA passage. The swinging motion of the STAG1-hinge module instead turns the DNA bend into a loop, while DNA slips along the NIPBL-head module. (c) Loop growth depends on the stochastic Brownian motion of the STAG1-hinge module. (d) The low DNA affinity of the STAG1-hinge module results in DNA release. (e) The STAG1-hinge module returns to form a new DNA gripping state upon nucleotide binding. (f) The next loop extrusion cycle begins. The in- and outbound DNAs are constrained by cohesin at a distance of  $\sim 23$  nm, in line with recent measurements of the condensin neck size when engaged in loop extrusion.<sup>150</sup> Adapted from Higashi *et al.*, 2021.<sup>152</sup>

to launch its swinging motion is to further bend the DNA, turning it into a loop, while DNA slips through the NIPBL-head module. The directed diffusive motion of the STAG1-hinge module has created a Brownian ratchet, allowing DNA motion only in one direction. The lower affinity of the STAG1-hinge module leads to release of DNA, while there is a time when there is only loose cohesin-DNA contact with the NIPBL-head module. Next, the ATPase heads can re-engage in the presence of ATP and the next gripping state can assemble. One question about this model is that no evidence has shown for stable interactions between the hinge and STAG1.<sup>151</sup> Another open question is whether DNA indeed fails to pass the kleisin N-gate before the initiation of loop extrusion.

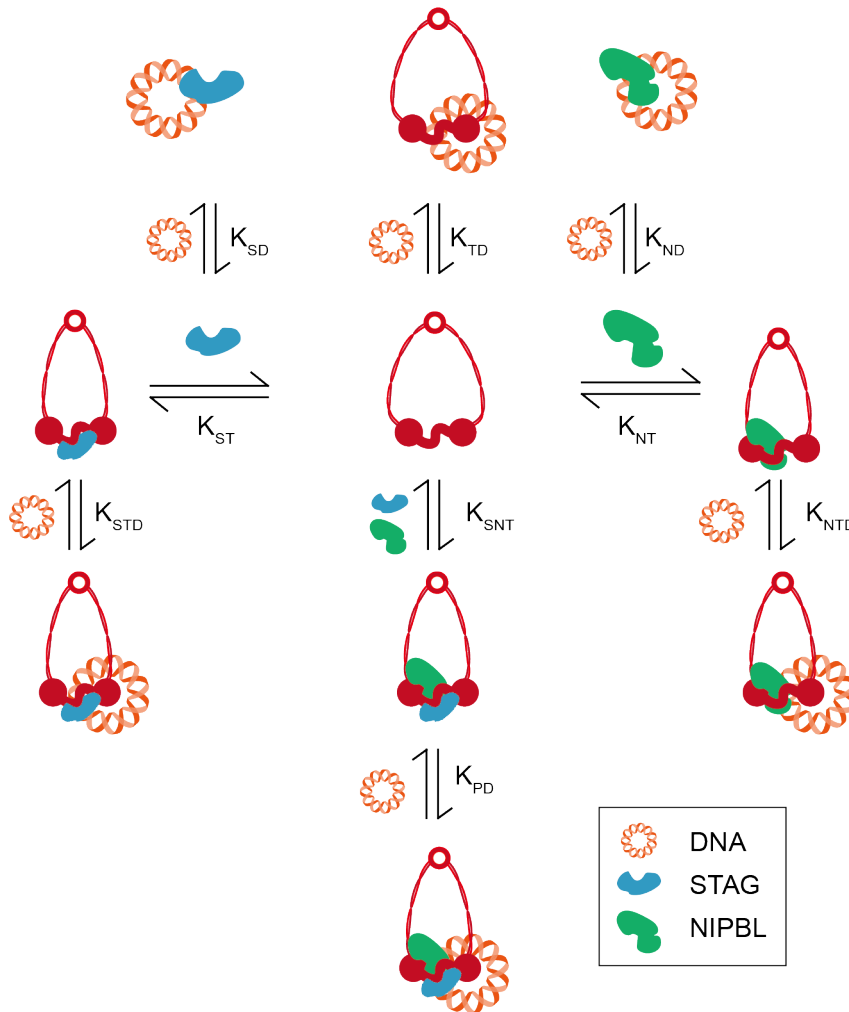


**Figure 5.5:** Biomolecular interactions capable of loop extrusion underlying the minimal cohesin complex. In this chapter, we examine this complex system from the intra-subunit interactions, DNA-protein interactions with the 3 subunits, to sub-assembly and full assembly interactions with DNA. Moreover, we study the effects of ATP binding/hydrolysis on all interactions to understand how ATP hydrolysis drives DNA loop extrusion by cohesin.

Although these models can account for some experimental observations, each has its own limitations and needs to be further tested. To understand the mechanism of loop extrusion, structural studies will be important to identify the DNA binding sites on cohesin that are necessary for loop extrusion, to solve the structures of cohesin complexes at various stages of the process and to visualise and measure the conformational changes during loop extrusion. On the other hand, studies looking into DNA affinities of individual subunits and

subcomplexes, and how they are modulated by ATP binding and hydrolysis would be another possible way to resolve the mechanism for loop extrusion by cohesin. However, the hetero-oligomeric and multimeric nature of the active complex makes it extremely challenging to reveal the associated molecular dynamics and mechanism. Therefore, in this chapter, we develop an experimental assay by using mass photometry to quantify the key interactions responsible for cohesin assembly, DNA binding, and their modulation by ATP binding and hydrolysis in a label-free environment and at the single molecule level (Figure 5.5).

## 5.2 Materials and Methods

### Minicircle DNA Expression and Purification

Supercoiled, closed-circle DNAs were prepared and provided by David Drechsel at Research Institute of Molecular Pathology, Vienna (IMP) using the ParA resolvase recombination system.<sup>153,154</sup> Briefly, upon induction of two enzymes (ParA and ITev) encoded on the plasmid, the ParA resolvase excised the target minicircle from the parental plasmid and the ITev endonuclease cleaved the vector backbone leading to its degradation. Lab scale production of MiniCircle (MC) DNA was performed in standard shaking flasks (Erlenmeyer) cultures. For good aeration, the culture volume should not exceed one third of the total flask volume. The cells were cultured at the respective temperature (either 28 °C or 37 °C) by continuous shaking (200 rpm). For cloning the MC constructs, plasmids were transformed into DH5alph cells and grown at 28 °C in the presence of kanamycin and 1% glucose. For expression of MCs, plasmids were transformed into BL21 or NEB Express cells. After maxi-prep, the DNA MCs showed some contamination and so PEG precipitation followed by T5 Endonuclease Clean-up of minicircle DNAs were carried out in order to increase

the purity. The resulting 302 bp minicircle DNA has a diameter of 33 nm.

## **Protein Expression and Purification from SF9 Insect Cell Cultures**

All protein constructs were prepared and provided by the Jan-Michael Peters Group at IMP as previously described.<sup>130,151</sup>

Baculoviruses for protein expression in Sf9 insect cells were generated as described.<sup>155,156</sup> Cultures were harvested after 48 – 60 h expression at 27°C, washed in PBS, frozen in liquid nitrogen and stored at -80 °C.

All protein purification was performed at 4°C. Cells were lysed by douncing 25 times in five pellet volumes of Lysis Buffer (50 mM NaPO<sub>4</sub> pH 7.6, 500 mM NaCl, 5% glycerol, 0.1% TWEEN, 10 mM imidazole) supplemented with 3 mM beta mercapto ethanol (bME), 1 mM benzamidine, 1 mM phenyl-methyl-sulfonyl fluoride (PMSF) and 1x EDTA-free protease inhibitor cocktail (PIC, Roche). Insoluble material was removed by centrifugation (35 min, 40000 xg, 4 °C) and the supernatant was incubated for 3 h at 4 °C with 5 mL of Toyopearl AF-chelate-650M resin (Tosoh Bioscience) pre-charged with Ni<sup>2+</sup> ions. Beads were collected by centrifugation, washed three times each with 50 mL Lysis-buffer supplemented with additional 5 mM imidazole but lacking bME and protease inhibitors and transferred to a glass column. Bound protein was eluted with 5 × 5 mL Ni-NTA Elution Buffer (50 mM NaPO<sub>4</sub> pH 7.6, 150 mM NaCl, 5% glycerol, 300 mM imidazole). The eluate was incubated for further 3 h at 4 °C with 5 mL of equilibrated FLAG-M2 agarose resin (Sigma).

For STAG1 purifications, cells were lysed by douncing with 25 strokes in 5 pellet volumes of Lysis Buffer (20 mM Tris pH 7.5, 500 mM NaCl, 20 mM imidazole, 3 mM bME), supplemented with 1x PIC, 1 mM PMSF and 1 mM benzamidine. Insoluble material was removed by centrifugation (35 min, 40000 xg, 4 °C) and the supernatant applied to 1.5 mL NiNTA-agarose (QIAGEN)

## 5.2. Materials and Methods

---

for 1.5 h at 4 °C. Beads were collected by centrifugation, washed three times with 50 mL Lysis buffer and transferred to a glass column. Bound protein was eluted with 4 × 2.5 mL of NiNTA elution buffer (20 mM Tris pH 7.5, 300 mM NaCl, 300 mM imidazole, 3 mM bME). Eluates were concentrated to 500 µL in 100 kDa MWCO spin filters (Amicon), and subjected to size exclusion chromatography using a Superdex 200 Increase 10/300 GL column (GE Life Sciences), equilibrated in Gelfiltration Buffer (20 mM Tris pH 7.5, 300 mM NaCl, 1 mM DTT). Fractions were analyzed by SDS-PAGE. STAG1-containing fractions were pooled, concentrated, snap frozen in liquid nitrogen in small aliquots and stored at -80 °C. Protein concentrations were determined by the Bradford assay.

In the case of NIPBL, the incubations were supplemented with 1 tablet of protease inhibitor cocktail. Beads were collected by centrifugation and washed three times with FLAG buffer (50 mM NaPO<sub>4</sub> pH 7.6, 100 mM NaCl, 5% glycerol, 50 mM imidazole), followed by elution of bound protein with 5 × 5 mL of FLAG-buffer supplemented with 0.25 mg/ml 3xFLAG peptide (DYKDHDGDYKDHDIDYKDDDDK). Eluates were concentrated to ~1 mL in 100 kDa molecular weight cut off (MWCO) spin filters (Amicon), snap frozen in liquid nitrogen and stored at -80 °C. Protein concentrations were analyzed by running samples next to BSA standards (Biorad) on SDS-PAGE followed by Coomassie staining and quantification of protein bands in ImageJ (NIH).

### **Mass Photometry**

All MP measurements were carried out in silicone gaskets (3 mm × 1 mm, GBL103250, Grace Bio-Labs) on microscopy slides that had been cleaned by consecutive sonication in Milli-Q water, isopropanol, and Milli-Q water, followed by the APTES functionalisation as illustrated in Section 4.2.<sup>109</sup> A

gasket was filled with 5  $\mu$ l buffer and the focal position of the glass surface determined and held constant using an autofocus system. 15  $\mu$ l of sample was then added and diluted into the buffer-filled gasket.

As the estimated concentration for each subunit obtained by the previous method was not reliable according to landing events counted in MP measurement, we thus normalised the relative concentration of each subunit using MP. As a result, trimer diluted 100-fold, STAG1 diluted 830-fold, NIPBL diluted 125-fold, and MC302 DNA diluted 210-fold in cohesin stock buffer (12.5 mM NaPO<sub>4</sub> pH 7.6, 25 mM NaCl, 1.25% glycerol, 2 mM MgCl<sub>2</sub>) were found to have the same landing frequencies. Prior to MP measurement, incubation of all protein complexes (1:1 stoichiometry) were performed for at least 20 min at room temperature. Trimer, STAG1, NIPBL and DNA were incubated with a volume ratio at 25:3:20:12 at their stock concentrations, with or without 2 mM ATP. The DNA sample used in the chapter was MC302, except for the result shown in Figure 5.7B where MC604 was used. The concentrated mixture was then diluted to  $\sim$  20 nM before MP measurements.

The data in Figure 5.8B (the result for NIPBL-tetramer + DNA) and Figure 5.10 (the results for STAG1/NIPBL-tetramer-DNA and pentamer-DNA in the presence ATP $\gamma$ S) were acquired on a Refeyn TwoMP mass photometer. All of the other data were acquired on a Refeyn OneMP mass photometer with a  $10.8 \times 2.9 \mu\text{m}^2$  field of view. A sequence of 6000 frames was recorded immediately after dilution at 1 kHz. Each condition was recorded in a separate gasket. Data acquisitions were performed using Acquire MP (Refeyn Ltd, v1.1.3) and processed using DiscoverMP v2.5.0 (Refeyn Ltd.). Contrast-to-mass calibration was performed by analysing a home-made protein standard diluted 10-fold in the same buffer. Contrast peaks corresponding to 90, 180, 360 and 540 kDa were used for calibration. Mass distributions were plotted by Gaussian fitting.

## Dissociation Constant Estimation

In the ideal case, the apparent  $K_D$  value can be calculated from the relative abundances of each species measured with MP<sup>4</sup>. For the 1:1 interaction of subunit A and subunit B, the  $K_D$  value can be obtained as:

$$K_D = \frac{[B]_{unbound} * [A]_{unbound}}{[AB]_{bound}}$$

where  $[B]_{unbound}$ ,  $[A]_{unbound}$  and  $[AB]_{bound}$  are the molar concentrations of free subunit B, free subunit A and the bound complex AB.

To convert the counts measured by MP into molar concentrations, we need to apply a conversion factor,  $f_{conversion}$ . Knowing that  $[A]_{total} = [AB]_{bound} + [A]_{unbound}$ , the conversion factor can be calculated as:

$$f_{conversion} = \frac{[A]_{total}}{counts(AB_{bound}) + counts(A_{unbound})}$$

where  $counts(AB_{bound})$  and  $counts(A_{unbound})$  are the counts obtained from Gaussian fits to the mass histograms.

The molar concentration of each subunit can then be converted to:

$$[AB]_{bound} = counts(AB_{bound}) * f_{conversion}$$

$$[A]_{unbound} = counts(A_{unbound}) * f_{conversion}$$

$$[B]_{unbound} = counts(B_{unbound}) * f_{conversion}$$

Therefore, the  $K_D$  value can be calculated as:

$$K_D = \frac{counts(B_{unbound}) * counts(A_{unbound})}{counts(AB_{bound}) * (counts(A_{unbound}) + counts(AB_{bound}))} * [A]_{total}$$

However, due to the uncertainty about the actual initial concentrations of the samples and the overlaps of the peaks assigned to different species, the  $K_D$

values cannot be evaluated accurately in terms of numbers. Therefore, all  $K_D$  values reported in this chapter were estimated based on the approximate ratios between the unbound species and bound complexes. For example, when no free subunit A (or B) is found when the complex AB forms, we assume that the  $K_D$  value is beyond the current detection limit, with the  $K_D$  value much smaller than 10 nM. On the contrary, if no complex is identified in the MP spectrum, it suggests that the  $K_D$  value is beyond the upper detection limit, with the  $K_D$  value much larger than 100 nM. If the ratio between the complex and the free subunit is about 1:1, then the  $K_D$  value is estimated as the half of the initial concentration (i.e.,  $K_D \sim 10$  nM). If the ratio between the bound complex and the free subunit is about 1:10, then the  $K_D$  value is estimated as 10 times of the initial concentration (i.e.,  $K_D \sim 100$  nM).

## 5.3 Results and Discussion

### 5.3.1 Intra-subunit Interactions and Pentamer Assembly

Before studying cohesin-DNA interactions, it is necessary to understand the self-assembly of the cohesin complex. Here, we reconstituted STAG1/NIPBL-tetramer and pentamer by mixing the associated three subunits in the stock buffer (12.5 mM NaPO<sub>4</sub> pH 7.6, 25 mM NaCl, 1.25% glycerol, 2 mM MgCl<sub>2</sub>) and measured by MP on APTES functionalised coverslips. Both STAG1 and NIPBL bound tightly to the cohesin trimer even in the absence of DNA or ATP (Figure 5.6A, B). For pentamer assembly, in line with loop extrusion experiments where the pentamer is strongly bound, the affinity was also high ( $K_{SNT} \sim 10$  nM) in MP measurements (Figure 5.6C). The remaining peak for STAG1 tetramer found in pentamer assembly could be explained by poor estimation of the protein concentration which resulted in excess amount of

### 5.3. Results and Discussion

STAG1. Overall, in spite of the difficulty to quantify the  $K_D$  further without confidence in the actual concentration of each subunit, it is still clear based on the current findings that the binding of both tetramers and pentamer are strong and their dissociation constants are within the nanomolar range.

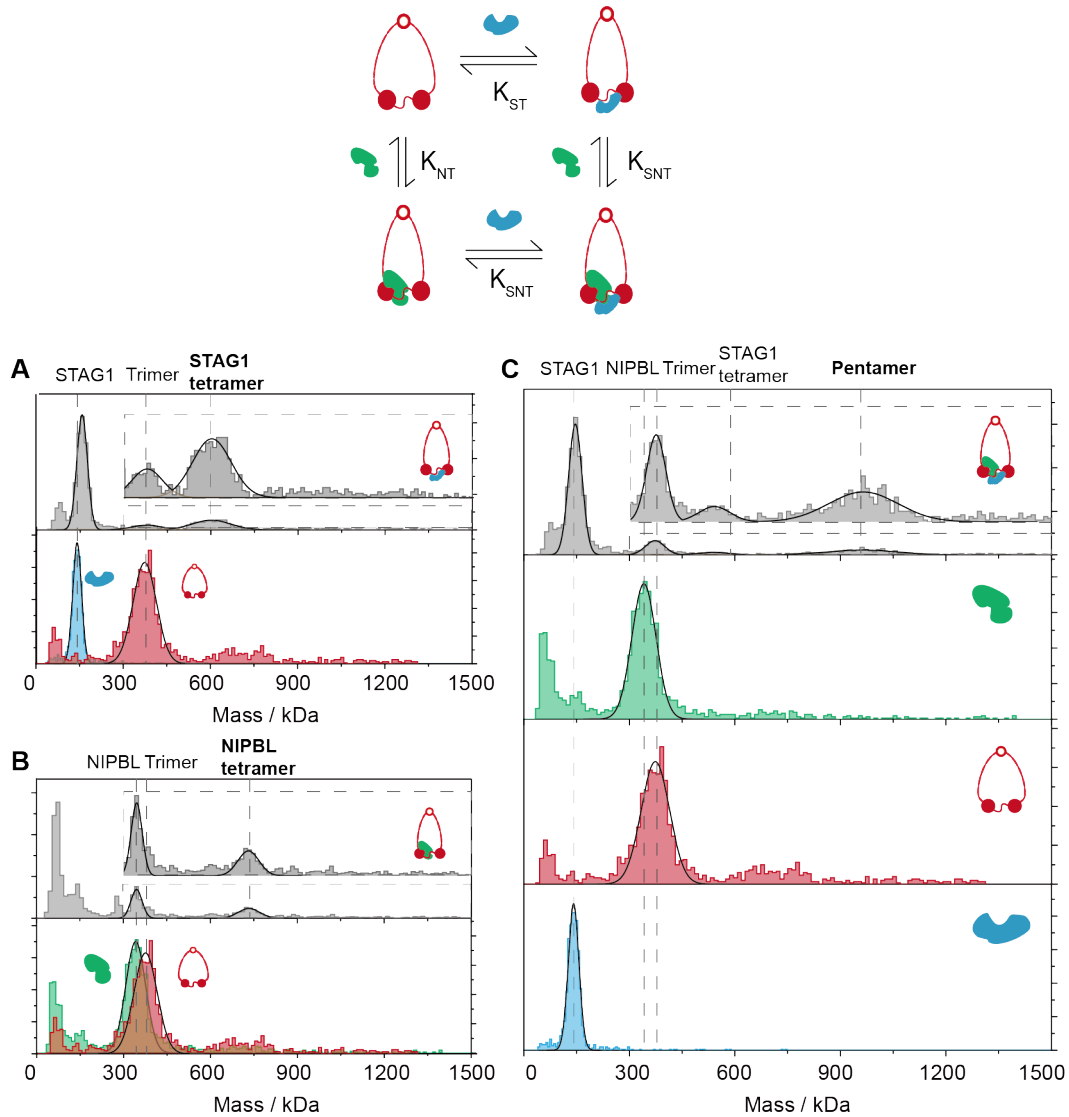


**Figure 5.6:** MP mass distributions of (A) STAG1 (blue), cohesin trimer (red), and the mixture of STAG1-tetramer (grey); (B) NIPBL (green), cohesin trimer (red), and the mixture of NIPBL-tetramer (grey); (C) pentamer (grey) formed by the mixture of STAG1 (blue), NIPBL (green) and cohesin trimer (red).

### 5.3.2 DNA Interactions With 3 Subunits: STAG1, NIPBL, Cohesin Trimer

STAG1, NIPBL and cohesin trimer are all DNA binding proteins. However, their binding affinities to DNA are not fully understood. Therefore, we set out to analyse the individual interaction between each subunit and DNA. To minimise heterogeneity, minicircle DNAs were used to study cohesin-DNA interactions. Due to the variation in refractive index for DNA and proteins, the 302 bp and 406 bp minicircle DNA (196 kDa, 392 kDa) were found at around 150 kDa and 300 kDa, respectively, when using the protein standard MS1000 for mass calibration.

At 20 nM concentration, no interaction between trimer itself and DNA was observed, suggesting the  $K_{TD}$  was much larger than 100 nM (Figure 5.7A). This observation agreed with the result found in Bauer *et al.*'s work where only a tiny shoulder peak was found when mixing the hinge/head domains with DNA at 500 nM and 5  $\mu$ M.

Instead of using MC302, which overlapped with the peak for STAG1 in the MP spectrum, a 604 bp minicircle DNA was mixed with STAG1 to quantify the interaction between STAG1 and DNA. Significant free DNA and STAG1 were seen in the mixture, indicating that STAG1 bound DNA with intermediate strength ( $K_{SD} \sim 100$  nM) (Figure 5.7B). Fluorescence anisotropy experiments also demonstrated that the equilibrium dissociation constant of STAG1 for a DNA substrate with scrambled sequences was approximately at around 100 nM ( $K_D = 104.0 \pm 13.6$  nM).<sup>157</sup> NIPBL bound very tightly to DNA ( $K_{ND} \ll 10$  nM), with no free NIPBL left in solution (Figure 5.7C). While oligomerisation of both STAG1 and NIPBL on DNA were observed, the affinity for STAG1-DNA binding was much smaller than that for NIPBL-DNA. This agrees with previous analysis conducted by electrophoretic mobility shift assay

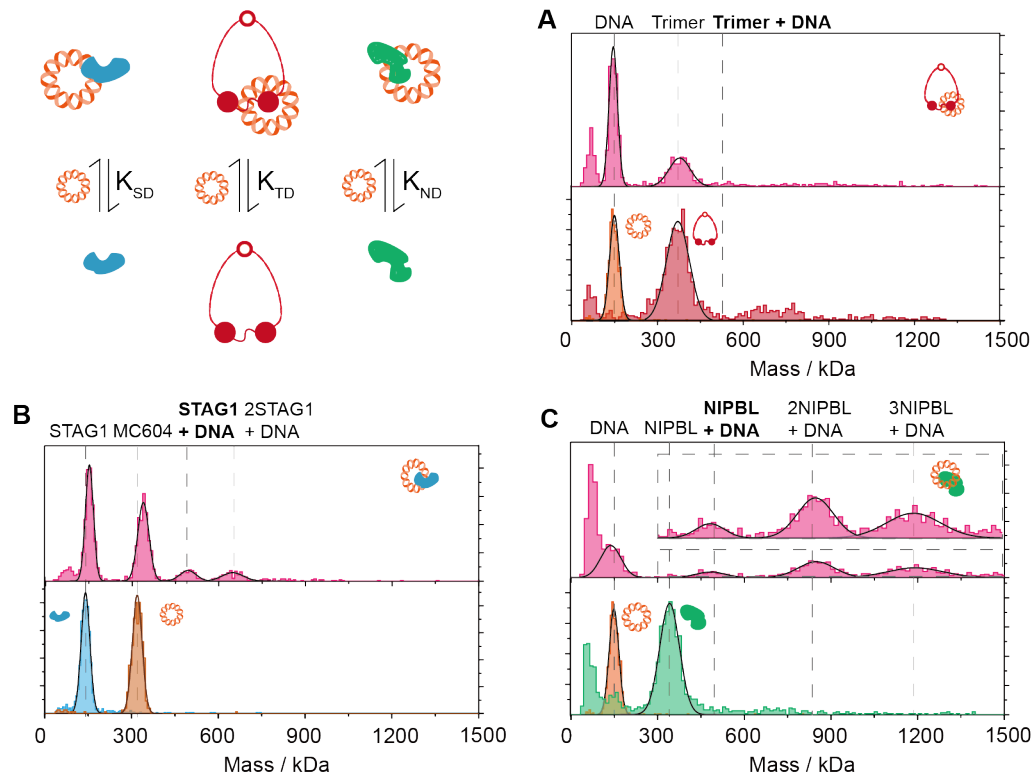


**Figure 5.7:** MP mass distributions of individual subunit: STAG1 (blue), NIPBL (green), cohesin trimer (red) and DNA (orange). Pink histograms and corresponding Gaussian fits show the MP mass distributions of (A) the mixture of trimer-MC302; (B) the mixture of STAG1-MC604; (C) the mixture of NIPBL-MC302.

(EMSA) where NIPBL-MAU2 (Mis4-Ssl3 in fission yeast) bound to DNA with equilibrium dissociation constants of 37 nM,<sup>158</sup> which was 3-fold smaller than that of STAG1-DNA analysed by fluorescence anisotropy experiments.<sup>157</sup>

### 5.3.3 DNA Interactions with Sub-assemblies and Full Assembly

Quantifying the DNA interactions with STAG1-tetramer and NIPBL-tetramer separately provides the potential to understand the role of STAG1 and NIPBL in the cohesin complex during DNA loading. Surprisingly, while previous *in-vitro* study found that cohesin alone (without NIPBL) did not bind or compact DNA even in the presence of ATP,<sup>131</sup> we observed very tight binding of STAG1-tetramer with DNA, with an estimated dissociation constant  $K_{STD}$  much

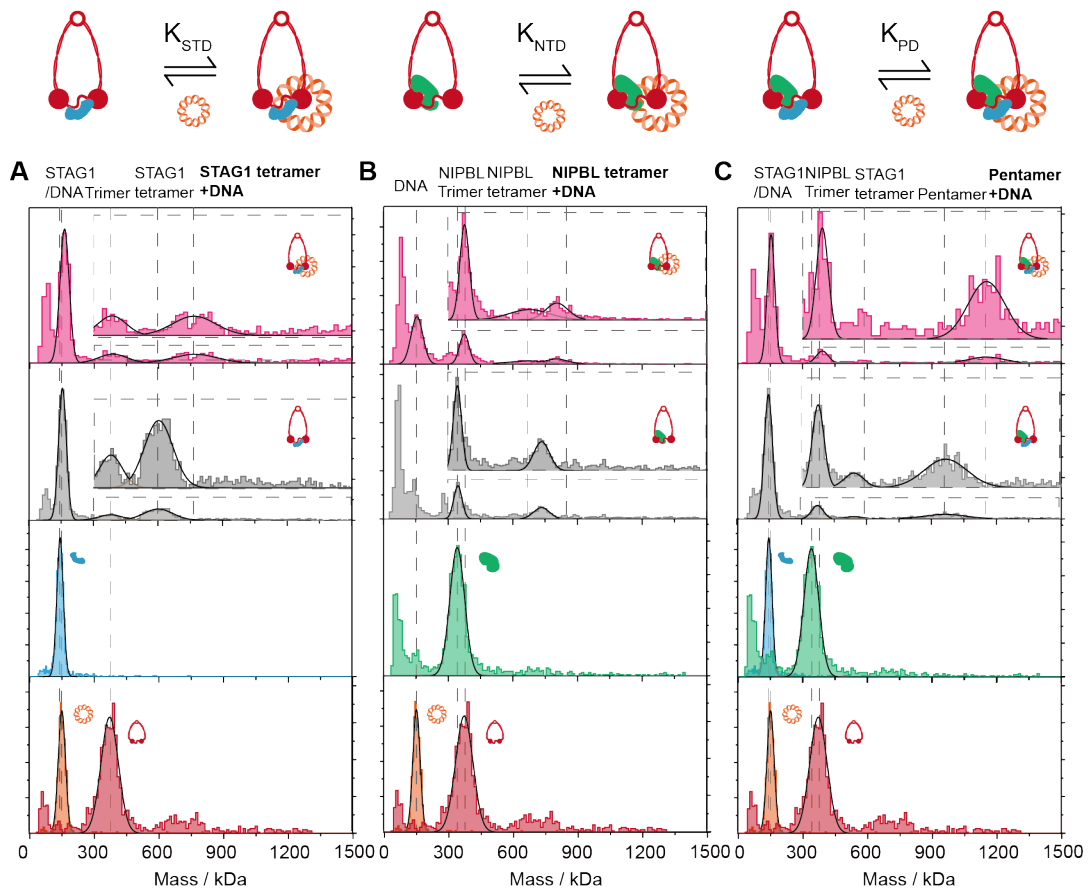


**Figure 5.8:** MP mass distributions of individual subunits: STAG1 (blue), NIPBL (green), cohesin trimer (red) and DNA (orange). Grey/pink histograms and corresponding Gaussian fits show the MP mass distributions of (A) the mixture of STAG1-tetramer in the absence/presence of DNA; (B) the mixture of NIPBL-tetramer in the absence/presence of DNA; (C) the mixture of pentamer-DNA in the absence/presence of DNA.

smaller than 10 nM (Figure 5.8A). This high affinity was possibly due to the AT-hooks at the N-terminus.<sup>159</sup> Different results given by TIRF measurements with aligned arrays of DNA molecules and MP measurements might be caused by concentration variations. While the TIRF study was performed with protein concentration at 1 - 3 nM,<sup>131</sup> MP analysis was conducted at 20 - 30 nM. At a further 10-fold dilution, the tetramer or the tetramer-DNA complex might also dissociate and could not be detected by MP.

For NIPBL-tetramer, the binding to DNA was much weaker when compared with the case of STAG1-tetramer. Free NIPBL-tetramer was observed at

relatively the same ratio of tetramer-DNA in the mixture (Figure 5.8B). The poor resolution of NIPBL-tetramer-DNA result could be explained by: (i) The impurities found in the NIPBL sample resulting in difficulty in identifying the complex in the broad MP distributions; (ii) Oligomerisation of NIPBL on DNA might saturate the structure of NIPBL, leaving no space for cohesin trimer to bind  $n$ NIPBL-DNA. The peak assigned for NIPBL tetramer + DNA could possibly be the peak for 2NIPBL + DNA. It is unclear which is the main reason for this observation at this stage, and further purification of NIPBL to remove contaminants would be mandatory to validate these assumptions.

In the absence of ATP, pentamer bound very tightly to DNA ( $K_{PD} \ll 10$  nM) (Figure 5.8C). However, because the experiment was conducted by simply mixing all the subunits, it was difficult to deduct the orders of the associated interactions. It could be either that the pentamer simultaneously assembles and then binds to the DNA, or free STAG1/NIPBL is needed for recruiting the DNA to the cohesin complex as proposed in a previous study.<sup>135</sup> Further experiments performed in a sequential manner will be ideal to classify the roles of both tetramers as well as each HEAT subunits (STAG1 and NIPBL) (see section 5.4).

#### **5.3.4 Modulation of all DNA-Protein Interactions by ATP**

ATP hydrolysis is required for DNA loop extrusion by cohesin. Understanding how ATP modulates the affinities of individual DNA-protein interactions in the cohesin complex might help us understand how ATP binding and hydrolysis drive loop extrusion. Adding ATP to trimer-DNA or NIPBL-DNA did not change the affinities of either associations (Figure 5.9). The result for NIPBL agreed with the fact that no ATP binding site was found on NIPBL. Whether ATP had any effect on trimer-DNA binding, however, still remained

questionable as the MP measurements were performed at low nanomolar concentration.

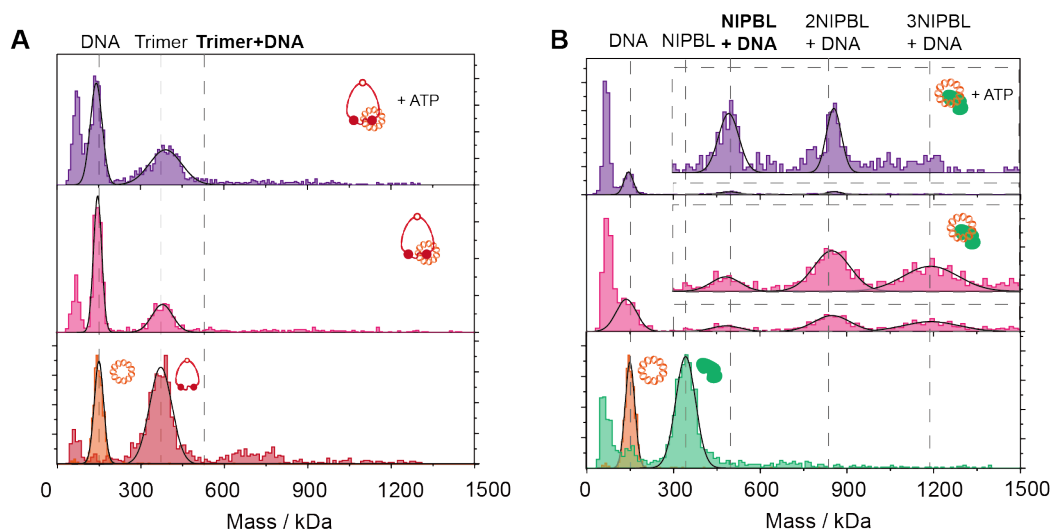


**Figure 5.9:** MP mass distributions of individual subunits: NIPBL (green), cohesin trimer (red) and DNA (orange). Pink/purple histograms and corresponding Gaussian fits show the MP mass distributions of (A) the mixture of trimer-DNA in the absence/presence of ATP; (B) the mixture of NIPBL-DNA in the absence/presence of ATP.

We now consider the consequences of ATP binding and ATP hydrolysis on the DNA interactions with both tetramers and the pentamer. We used ATP $\gamma$ S, the substrate and inhibitor of ATP-dependent enzyme systems, which is hydrolysed very slowly by phosphatases and most ATPases. We assumed that, in our measurement time-frame, there was no ATP hydrolysis but only ATP binding when adding ATP $\gamma$ S to the mixture. Upon ATP binding, DNA was partially released from STAG1-tetramer while no changes were observed for NIPBL-tetramer or pentamer (Figure 5.10 yellow histograms). In contrast, upon ATP hydrolysis, while all complexes stayed intact, DNA was fully released from all sub-assemblies and the full assembly - no complex/subcomplex-DNA peaks were found in the presence of ATP (Figure 5.10 purple histograms). These results together suggest that STAG1-cohesin and NIPBL-cohesin might have different functions during DNA loop extrusion in the ATP hydrolysis

## 5.3. Results and Discussion

cycle.

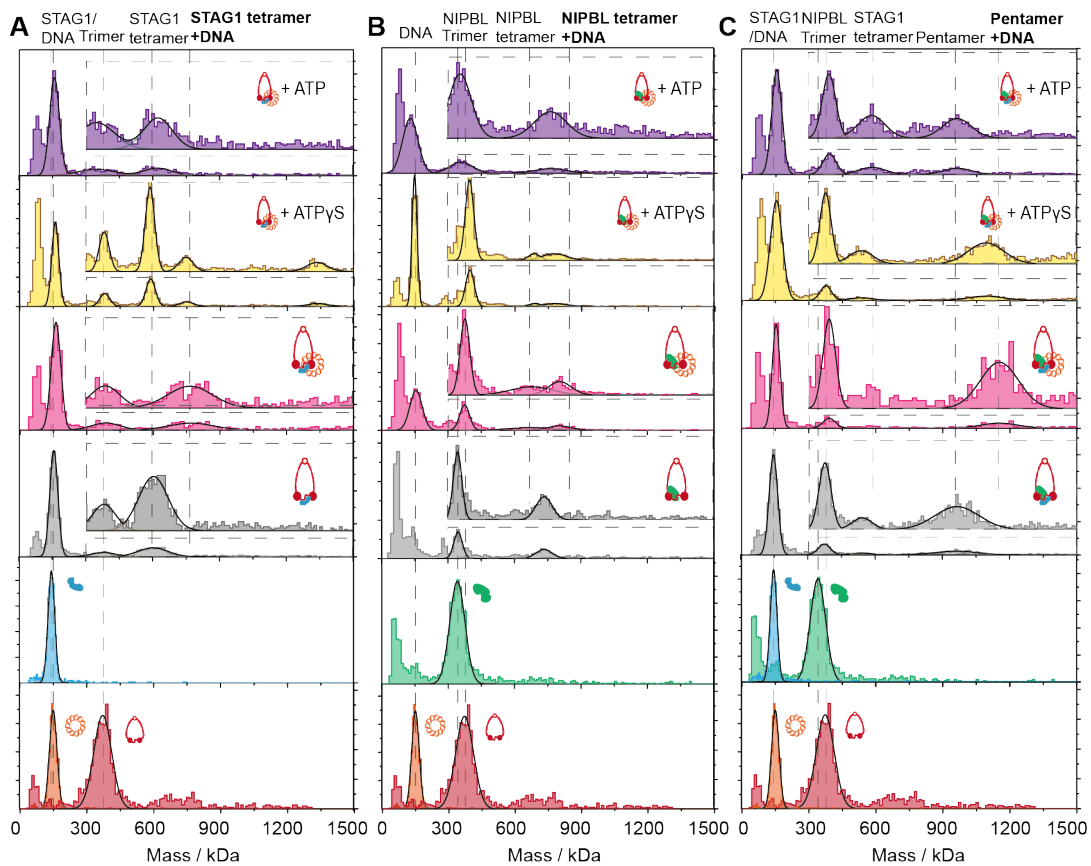


**Figure 5.10:** MP mass distributions of individual subunits: STAG1 (blue), NIPBL (green), cohesin trimer (red) and DNA (orange). Grey/pink histograms and corresponding Gaussian fits show the MP mass distributions of (A) the mixture of STAG1-tetramer in the absence/presence of DNA; (B) the mixture of NIPBL-tetramer in the absence/presence of DNA; (C) the mixture of pentamer-DNA in the absence/presence of DNA. Yellow/purple histograms and corresponding Gaussian fits show the MP mass distributions of subcomplex-DNA interactions in the presence of ATP $\gamma$ S/ATP.

### 5.3.5 ATP Drives Loop Extrusion by Modulating the DNA Affinities of STAG1-Cohesin and NIPBL-Cohesin

NIPBL binds tightly to and multimerises on DNA even in the absence of cohesin, and its affinity for DNA binding is only modulated by ATP in the presence of cohesin. STAG1 binds slightly weaker than NIPBL to DNA but still multimerises on DNA. Both tetramers formed with STAG1 and NIPBL,

as well as the active pentamer complex, bind to DNA strongly in the absence of ATP, while ATP hydrolysis leads to DNA release from all assemblies. ATP binding only modulates the affinity of the STAG1-tetramer to DNA, but has no effect on DNA affinity of NIPBL-tetramer and pentamer. Taken together with previous biochemical and structural studies, our results point towards a mechanism for loop extrusion based on choreographed binding and unbinding of DNA mediated by STAG1 and NIPBL (Figure 5.11), similar to the “tethered inchworm” model.<sup>143</sup>

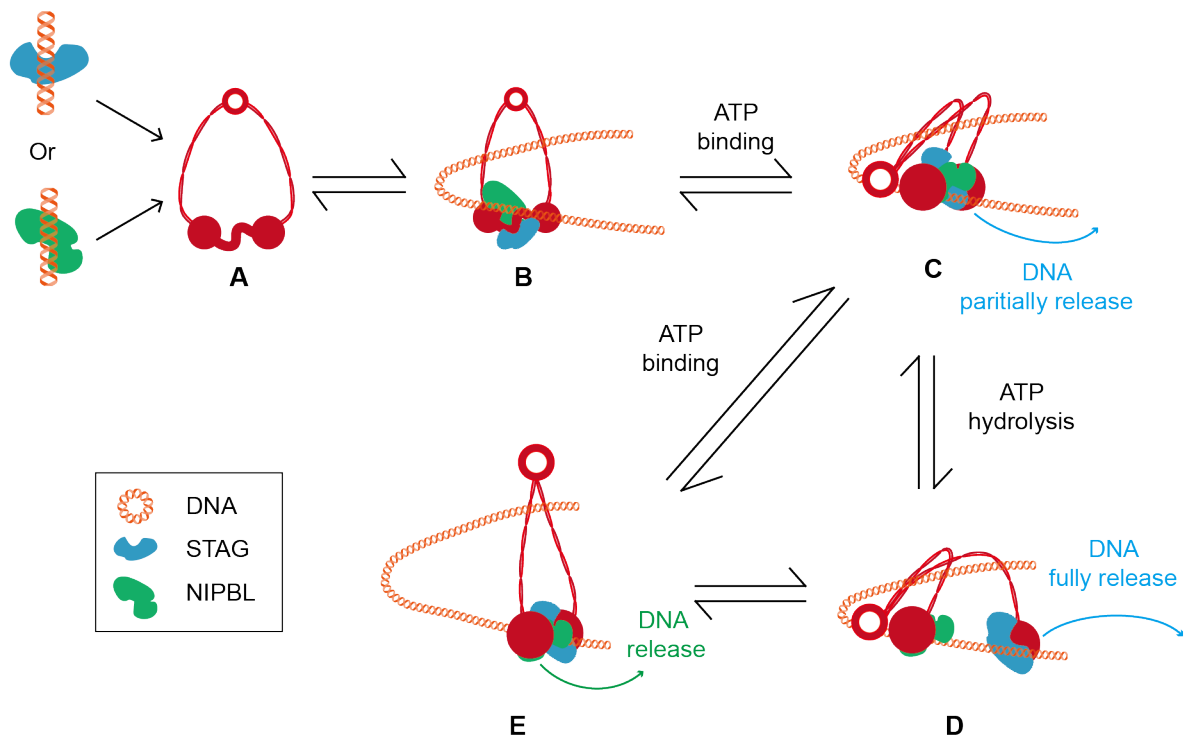


**Figure 5.11:** A model for loop extrusion based on MP results. **(A)** Free DNA is recruited by free STAG1/NIPBL in solution. **(B)** The STAG1/NIPBL-DNA binds to cohesin to form the pentamer-DNA complex. **(C)** ATP binding leads to head engagement and partially releases DNA from the STAG1-head module while the NIPBL-head module holds onto DNA tightly. **(D)** Upon ATP hydrolysis, the two head domains disengage and the STAG1-head module releases DNA first, followed by **(E)** a subsequent release of DNA by NIPBL-cohesin module. The coiled coil is stretched back to straight, resetting cohesin for the next cycle.

The initiation of DNA binding by the cohesin ring is the DNA recruitment by free STAG1/NIPBL, followed by binding of STAG1/NIPBL-DNA to cohesin,

as also suggested in the work conducted by Shi *et al.* and Li *et al.*.<sup>135,160</sup> There are two DNA binding modules found in cohesin: STAG1-cohesin and NIPBL-cohesin, where both HEAT subunits associate with one of the two ATPase heads. The HEAT subunit DNA affinity changes during the ATP hydrolysis cycle such that the force from ATP head engagement is transferred to move DNA, similar to the mechanism suggested in the “tethered inchworm” model.<sup>143</sup> The weakly bound HEAT subunit (likely to be STAG1) releases DNA first, followed by a sequential release by another HEAT subunit (likely to be NIPBL), leading to processive motion of cohesin along DNA. The SMC hinge domain provides a weak, but necessary additional pin point to convert this into loop extrusion, as also suggested in the “swing and clamp” model<sup>151</sup> and the “Brownian ratchet” model.<sup>152</sup>

Our model can be considered as a variant of the “tethered inchworm” model<sup>143</sup>, with a clear distinction between the functions of each HEAT-head modules during the ATPase cycle. No evidence has been found in the “tethered inchworm” model about which HEAT-head module releases DNA first, while our results show that STAG1-cohesin partially releases DNA upon ATP binding. We have also combined our dynamic results with the bend conformation found in the previous structural studies to identify the function of the hinge domain during loop extrusion.

The main difference between our model with the “swing and clamp” model<sup>151</sup> is that we determine the function of STAG1 in this process and successfully observe the dissociation of DNA from the cohesin complex upon ATP hydrolysis. The change in the DNA affinity of STAG1-cohesin upon ATP binding and hydrolysis suggests that DNA translocation during loop extrusion cannot be only controlled by NIPBL alone.

Our results of tight and stable DNA binding of STAG1-cohesin invalidate

the assumption that the lower affinity of the STAG1-hinge module leads to release of DNA while NIPBL-head module loosely contact with DNA during loop extrusion, as suggested in the “Brownian ratchet” model<sup>152</sup>. Additionally, smFRET experiments found in the previous study failed to detect stable interactions between the hinge and STAG1<sup>151</sup>. Therefore, we believe the STAG1 is associated with one of the head domain instead of the hinge domain during DNA binding and loop extrusion.

## 5.4 Conclusion and Outlook

In this chapter, by adopting an MP approach to quantify the key interactions responsible for cohesin assembly, DNA binding, and their modulation by ATP binding and hydrolysis, we identify two important DNA binding modules in cohesin: the STAG1-head module and the NIPBL-head module. The DNA affinities of these two modules are modulated by ATP binding and hydrolysis, which points towards a mechanism for loop extrusion based on sequential hold and release of DNA mediated by STAG1 and NIPBL.

However, there are still lots of improvements that can be done to validate the current results and a number of open questions remained to be addressed for a better understanding in the mechanism. Higher resolution and better statistics might be achieved by improving the purification for NIPBL, measuring the mixture at higher concentration, as well as using the newly released mass photometer TwoMP with bigger FOV. Besides, topological DNA binding by cohesin is expected to be salt resistant<sup>129,134</sup>. Further experiments should repeat the MP assay with circular DNA using high-salt buffer to understand whether the DNA loading is topological or pseudo-topological. In addition, previous studies using linear DNA showed opposite observations as the MP results<sup>134</sup>, where no DNA binding was found for STAG1-cohesin in the absence

of ATP. Further experiments should look into whether the listed DNA-protein interactions are DNA shape or size dependent. To understand what happens at the initial stage, whether it is that the trimer binds to HEAT subunits which bound to DNA, or, the assembled pentamer binds to DNA, one needs to do a mixing experiment where DNA and ATP are added in a sequential manner after the proteins mixture are formed and confirmed by MP. Also, individual affinities of both HEAT subunits to both ATPase heads and the hinge domain should be quantified to confirm the existence of the two DNA-binding modules.

Nevertheless, this chapter sets out a great example of an MP approach to study complex biomolecules with the multimeric nature. Dynamic information obtained by this approach can be utilised to establish new models or to complement the current models proposed based on the findings by other techniques. These results highlight mass photometry as an accurate, rapid, and label-free single molecule method complementary to existing techniques for characterising and quantifying complex biomolecular assemblies and protein-DNA interactions.

# Chapter 6

## Surface Passivation for Mass Photometry

### 6.1 Introduction

Mass photometry has proven to be a powerful tool for studying a wide range of biological phenomena at the nanoscale, ranging from macromolecular assemblies to protein-DNA interactions. As the complexity of the biological system to be measured increases, it is no longer sufficient to use unmodified glass coverslips to which the biomolecules non-specifically bind. Surface functionalisation changes the properties of the glass surface to modify its interactions with biomolecules, allowing for more complicated systems to be investigated. In the case of measuring nucleic acids, altering the surface charge to positive largely increases the affinity of DNA to glass.<sup>95</sup> Another option to modify the surface is to coat the glass with a passivation layer, which prevents non-specific binding of biomolecules to the glass.<sup>161,162</sup>

Surface passivation techniques aim to reduce non-specific protein bindings by blocking the surface with a surfactant which has a low affinity for proteins. For instance, surface treated with bovine serum albumin (BSA) is commonly used for single-molecule nucleic acid studies.<sup>163</sup> Other approaches to coat the surface such as adopting Pluronic F-127<sup>164</sup> and Tween 20,<sup>165</sup> are not favourable

for MP measurements due to their non-covalent nature. These surfactants might leave the glass surface during the experiment because of the exposure to high-power laser, which will also be detected by MP and thus interfere with the measurement.

An alternative covalent pathway is to use a siloxane linker to attach a passivation molecule to the surface. One example with a great passivation performance is to coat the glass with polymer, polyethylene glycol (PEG).<sup>166</sup> This scheme involves a dense packed coating of PEG to the surface which forms a “brush like” coverage. Since it was introduced to single-molecule fluorescence studies, the PEG passivation method has become universally used for single-molecule protein studies.<sup>167,168</sup>

An additional advantage of PEG passivation is that the PEG molecules can be modified with the addition of other molecules that can specifically bind to proteins of interests. For example, conjugating the PEG through a metal-mediated complexation agent, nitrilotriacetic (NTA), enables the surface to bind reversibly with the protein that has the histidine side chain (Figure 6.1A). The rationale comes from immobilised metal ion affinity chromatography (IMAC), which is often employed to purify protein in molecular biology.<sup>169,170</sup> Apart from its application in protein purification, NTA is also used with hexahistidine (His6)-tagged proteins for fluorescent labeling<sup>171,172</sup> and surface immobilisation.<sup>173,174</sup> As illustrated in previous studies, mono-NTA derivatives and His6-tagged proteins have a weak interaction at a  $K_D$  of about 10  $\mu\text{M}$ , but it can be significantly increased to the level of  $K_D \sim 10$  nM by exploiting the multivalency of derivatives with several molecules of NTA.<sup>175,176</sup> More importantly, the association between NTA and histidine is highly tunable thanks to its activation with  $\text{Ni}^{2+}$  ion. Through adding EDTA and imidazole to the bound NTA-Ni-His bridge, the protein can then be released from the

PEG-NTA surface. Given the specific and reversible nature of the PEG-NTA surface, one can control the binding as well as the unbinding of proteins to the surface.

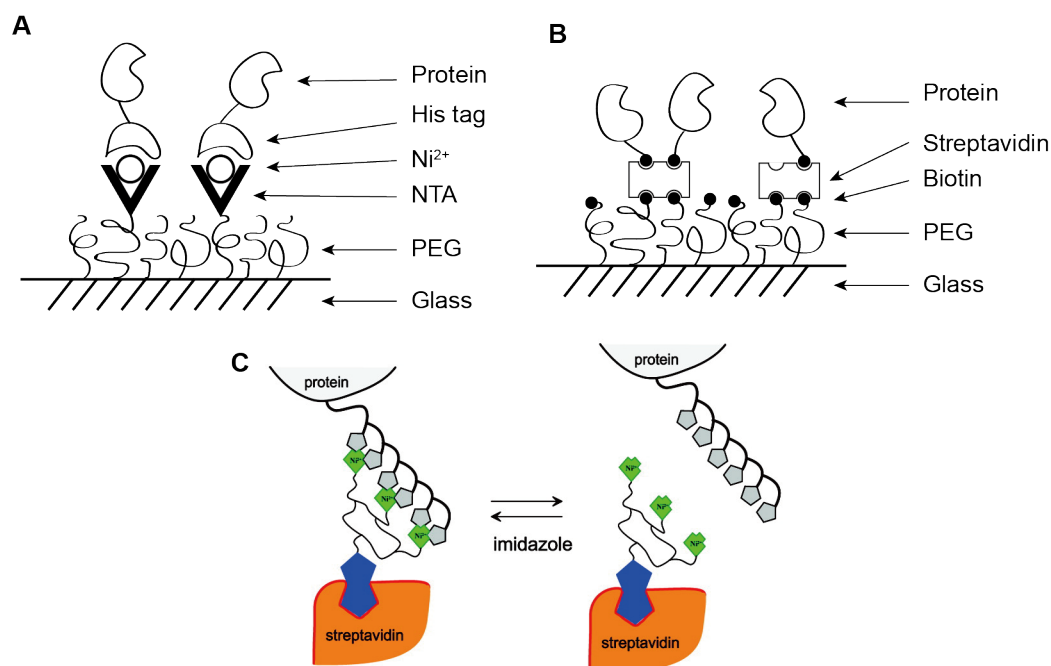


**Figure 6.1:** PEG functionalisation scheme of (A) PEG-NTA surface, (B) Biotin-PEG surface. (C) Principle of the reversible biotinylation of histidine-tagged proteins. C is adapted from Reichel *et al.*, 2007.<sup>177</sup>

Adding a small amount of biotin-PEG to the surface allows proteins with biotin moiety to be specifically bound to the surface via a streptavidin or avidin linker while excluding other non-biotinylated molecules<sup>178</sup> (Figure 6.2B). The high-affinity, selective recognition of biotin-PEG passivation is an extremely powerful tool in developing biological assays. The versatility of the biotin-streptavidin system relies on (i) the robust, quasi-irreversible interaction, (ii) the multivalent nature of streptavidin, which allows sandwich-type assays, and (iii) the compatibility of biotin with chemical conjugation protocols. One critical issue, however, is the selective, site-specific incorporation of biotin into proteins. Though studies have shown efficient approaches for site-specific covalent biotinylation,<sup>179,180</sup> non-covalent, reversible biotinylation would further increase

the versatility of the system, as biotin-streptavidin association can only be reversed under extremely harsh conditions. Therefore, a site-specific reversible biotinylation of proteins through their histidine tags using biotin conjugated to the multivalent chelator, trisnitrilotriacetic acid ( $^{BT}$ tris-NTA), was developed by Reichel *et al.* (Figure 6.2C).<sup>177</sup> In their work, they demonstrated stable binding of  $^{BT}$ tris-NTA to His-tagged proteins, which was readily reversed by addition of imidazole, enabling versatile conjugation schemes in solution as well as at the interface.

Various PEGylation protocols can be found in the literature, and can be generally divided into two main categories - one-step and two-step process, referring to the number of steps involved in attaching the PEG molecules to the surface (Figure 6.2). In the one-step process, PEG-silane is directly attached to the surface via the reaction between the silanol group on the glass surface and the silane group on PEG.<sup>181</sup> While in the two-step process, APTES is first introduced to the glass surface following by the attachment of PEG via the reaction between the APTES's amine group and a functional group on the PEG, e.g. succinimidyl-valerate (SVA),<sup>182</sup> N-hydroxysuccinimide (NHS).<sup>183</sup> Due to the larger size of PEG silane than APTES's steric effects, a sparser coverage of PEG is found in the one-step process compared to the one in the two-step process.

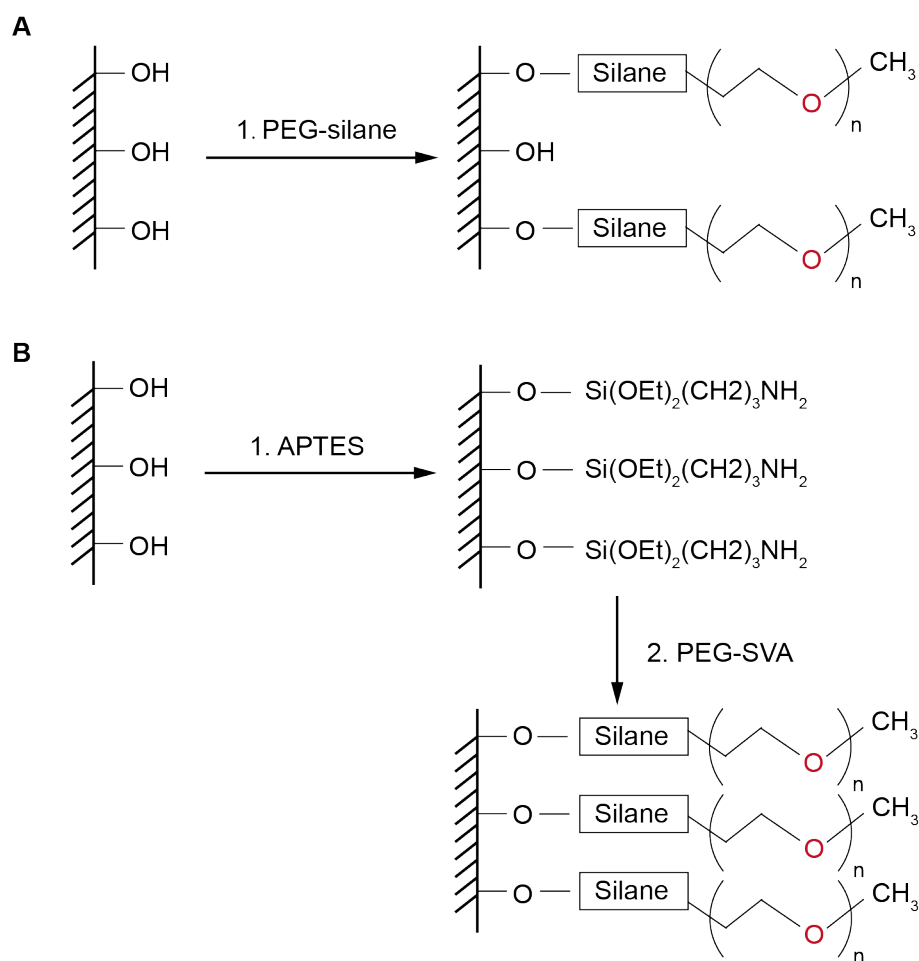


**Figure 6.2:** (A) One-step PEGylation process. PEG-silane is directly attached to the glass surface. (B) Two-step process. APTES is attached to the surface before the it is functionalised with a PEG group via the succinimidyl-valerate group. PEG - polyethylene glycol, APTES - (3-Aminopropyl)triethoxysilane, SVA - succinimidyl-valerate.

With a well-developed reversible landing assay, MP should be able to measure proteins of interest even at low abundance in a mixture, through unbinding from the surface (Figure 6.3). There are three main steps involved in this kind of experiment . (i) In the loading step, a mixture consists of different proteins and complexes is flowed onto the surface, with only protein of interest his-tagged. (ii) In the washing step, buffer wash helps to remove weakly bound untagged proteins. The strongly bound untagged and tagged proteins remain on the surface. (iii) In the final elution step, the surface immobilised with

proteins is washed with imidazole or EDTA to elute the his-tagged proteins. This step is the point at which an MP measurement is actually taken, in the knowledge that all unbinding events are his-tagged protein analyte.

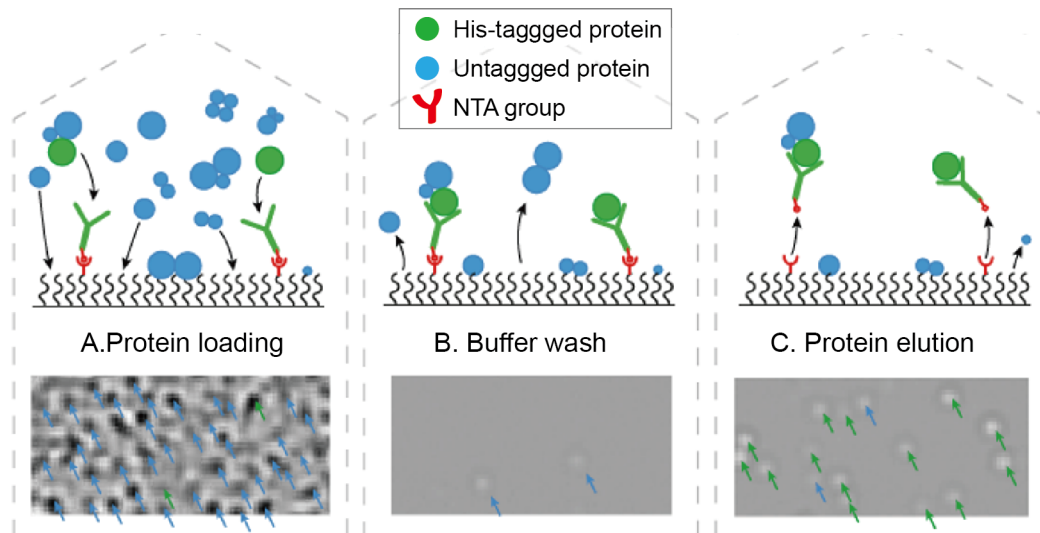


**Figure 6.3:** Scheme of measuring a protein of interest via a reversible landing assay. **(A)** Protein loading: A complex mixture with only one kind of protein is his-tagged is flowed onto the assay. The tagged proteins bind to NTA groups on the surface, while the untagged protein may bind non-specifically. **(B)** Buffer wash: The surface is then rinsed with buffer to remove the weakly bound untagged proteins while strongly bound untagged and tagged proteins remain on the surface. **(C)** Protein elution: The surface is washed with imidazole or EDTA to elute the his-tagged proteins. This is the point at which the MP measurement is actually taken, in the knowledge that the unbinding events are all his-tagged proteins (protein of interest).

To achieve this goal, we examine the effectiveness of different conjugation strategies in this chapter, including PEG-NTA, PEG-biotin, PEG-biotin-Streptavidin-<sup>BT</sup> tris-NTA, in passivating the glass surface as well as specifically binding and orienting proteins of interests, by two different techniques, MP and TIRFM. By adopting the surface passivation techniques to MP, one should be able to control the binding and unbinding of bio-molecules, which allows for the measurements of low-abundance proteins of interest in mixtures even without a pre-purification step.

## 6.2 Materials and Methods

### Sample Preparation

Solvents and chemicals were purchased from Sigma Aldrich unless otherwise noted. Milli-Q water and high-grade solvents were used for all experiments. Apo-transferrin (T2252), anti-transferrin (purchased from Medix Biochemica, 100525), and Alexa Fluor 488 streptavidin (purchased from Invitrogen, S11223) were either received as liquid in their original buffers, or reconstituted in Milli-Q/PBS as concentrated stocks. The concentrated stocks were then diluted in desired buffers (20mM HEPES or DPBS) to desired final concentrations before measurements (details can be found in the Section 6.3). Samples were kept at room temperature during analysis.

For TIRFM measurements, the protein marker MS1000 and anti-transferrin were labelled by using CF532 Dye & Biotin SE Protein Labeling Kits (purchased from Biotium, 92208). The details of the labelling procedures can be found in its manual. In short, 100  $\mu$ L of 1 M sodium bicarbonate pH 8.3 (99954) was added to the 900  $\mu$ L protein solution. 25  $\mu$ L of anhydrous DMSO (99953) was added to the vial of warmed up CF dye at room temperature. The dye stock was then added to and mixed with the protein solution. The protein/dye solution was protected from light by wrapping the vial in aluminium foil and then incubated for 1 hour at room temperature with gentle rocking. After incubation, the reaction solution was purified by centrifuging three times with a filtration vial (99956) and 1X PBS (99955) until the fluorescent color of the solution became very light to remove the unconjugated free dye from the labelled protein. Finally, an appropriate amount of 1X PBS was added to the filter sample reservoir to re-suspend the protein at the desired concentration.

### Surface Passivation

mPEG-SVA MW 5000 and Biotin-PEG-SVA MW 5000 were purchased from Laysan Bio. NTA-PEG-NHS MW 5000 (PG2-NSNT-5k) was purchased from Nanocs. All PEG reagents were aliquoted after arrival and stored at  $-20^{\circ}$ . PEGylated slides were prepared based on the protocol produced by Chandradoss *et al.*<sup>184</sup> Briefly, the coverslips were treated with the APTES protocol (see Section 4.2) with the following modifications. The coverslips were swirled in APTES for 2-3 mins and then dried in the oven for 2 hours. After removing from the oven, the slides were cooled at room temperature and sonicated in acetone for 10 mins, followed by rinsing in milli-Q and blow drying with nitrogen gas. The PEG aliquots were defrosted for 10 mins at room temperature before being dissolved in 50 mM MOPS-KOH (pH = 8.0) buffer at 100 mg/ml. Biotin-PEG was mixed with the mPEG-SVA solution at 10% while NTA-PEG was mixed with the mPEG-SVA solution at 30%. The solution was centrifuged for 30 seconds to remove bubbles. 60  $\mu$ L of PEG solution was pipetted to an APTES-treated coverslip and sandwiched with another APTES coverslip on top of the other. The sandwiched coverslips were placed in a humidity chamber and left in the dark environment overnight. The slides were then separated followed by rinsing with water and blow drying with nitrogen before measurements. Silicone gaskets (3 mm  $\times$  1 mm, GBL103250, Grace Bio-Labs) were rinsed sequentially with Milli-Q water, isopropanol and Milli-Q water, dried under a nitrogen stream, and placed on the PEGylated glass coverslips. For PEG-NTA surface, 15  $\mu$ l of 10 mM  $\text{NiCl}_2$  was loaded to the gasket well and incubated for 30 mins to activate the NTA group before a thorough buffer wash.

For attaching the  $^{BT}$  tris-NTA to the prepared PEG-biotin surface, 15  $\mu$ l of 50 nM of Streptavidin was first added to each gasket and immobilised on

the surface at room temperature for 30 mins. After washing with DPBS, 15  $\mu\text{l}$  of 1  $\mu\text{M}$  <sup>BT</sup>tris-NTA was then added to the same gasket and incubated for 30 mins. Before immobilising proteins on the surface, 10 mM  $\text{NiCl}_2$  was loaded to the gasket well and incubated for 30 mins to activate the NTA group before a thorough buffer wash. For protein elution, the surface was washed with 500 mM EDTA solution three times. Buffer was then added after the elution of protein before the TIRFM measurement.

### **Total Internal Reflection Microscopy**

TIRFM measurements were performed using a home-built micro-mirror total internal reflection microscopy as previously described (Figure 6.4).<sup>45</sup> In this setup, two small mirrors were used to couple illumination light in and out of the objective in an objective-type TIR arrangement, providing the microscope with a high level of background suppression, with a nanometer localisation precision at 6  $\mu\text{s}$  exposure time for 20 nm gold nanoparticles with a  $25 \times 25 \mu\text{m}^2$  field of view. Measurements in this chapter were all taken with a green laser (LDM-520-1000-C) as the illumination source. The input laser power was selected at 300 mV, which corresponded to  $\sim 0.9$  mW. The exposure time and frame rate were chosen at 90 ms and 10 Hz. Without temporal averaging and pixel binning, field of view was selected to be  $25 \times 25 \mu\text{m}^2$ , which had an effective pixel size of 51.7 nm.

After loading and incubating the protein on the functionalised surface for 30 mins, a buffer wash was performed before the TIRF measurement. After illuminating the protein-immobilised surface, a movie lasting 10 s was immediately recorded for individual measurement, resulting in a 100-frame .tdms file for each measurement. 5 replicates were taken for each sample by changing the location within the same gasket well. All TIRF data were acquired by a

setup-accompanied Labview software with the output movies in .tdms files without any pre-processing. The movies were then analysed by a home-written python code. The TIRF image was generated by averaging the total 100 frames in each movie. The total pixel intensity was a sum of all pixel intensities read out by all frames in each movie.

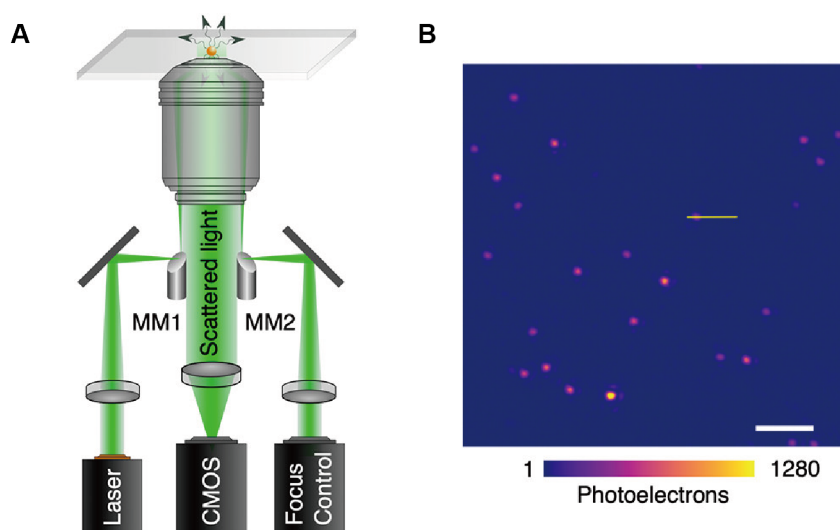


**Figure 6.4:** (A) Objective-type TIR using two micromirrors. (B) Respective image of 20 nm AuNPs immobilized on cover glass. Scale bar: 2  $\mu\text{m}$ . Adapted from Meng *et al.*, 2021.<sup>45</sup>

## Mass Photometry

All MP measurements were performed using the commercially available *One<sup>MP</sup>* mass photometer (Refeyn Ltd, Oxford, UK). Movies were recorded at 1 kHz for 2 minutes, with exposure times adjusted to maximise camera counts while avoiding saturation. Images were time averaged 5-fold and pixel binned 4 x 4 for an FOV at  $2.9 \times 10.8 \mu\text{m}^2$  before saving. Data acquisition was performed using Acquire MP (Refeyn Ltd, v1.1.3). All acquired MP movies were processed and analysed using Discover MP v2.4.0 (Refeyn Ltd). The analysis procedure involved two fitting parameters for identifying landing events: (i) Threshold 1 related to a given particle contrast amplitude relative to the background

and (ii) Threshold 2 related to the radial symmetry of the detected point spread function (PSF) of the same particle. The analysis parameters for MP measurements of transferrin on both glass and PEG surfaces are (i) Number of binned frames,  $n = 5$ , (ii) Threshold 1 = 1.5, and (iii) Threshold 2 = 0.25. Raw contrast values were converted to molecular mass using a standard mass calibration, and binding events combined in 5 kDa bin width. The ratiometric images of his-tagged MS1000 on PEG-NTA and PEG-NTA-Ni surfaces were also generated by Discover MP v2.4.0. The analysis parameters for MP measurements of streptavidin and anti-transferrin on biotin-PEG are (i) Number of binned frames,  $n = 8$ , (ii) Threshold 1 = 1.5, and (iii) Threshold 2 = 0.25.

## 6.3 Results and Discussion

### 6.3.1 PEG Passivation of Glass Coverslips

By adding 100 mg/ml PEG-SVA solution to APTES functionalised glass surface, successful PEG passivation was achieved. While over 2000 binding events were found for 50 nM transferrin landing on a regular glass surface (Figure 6.5A, C), very few binding events were noticed for transferrin even at much higher concentration up to 660 nM (Figure 6.5B, C). Besides, many of unbinding events were observed when measuring transferrin on a PEGylated surface (Figure 6.5B). These results together have shown a successful passivation on the glass surface by using the adopted protocol, with a significant reduction of non-specific protein binding to the PEGylated surface.

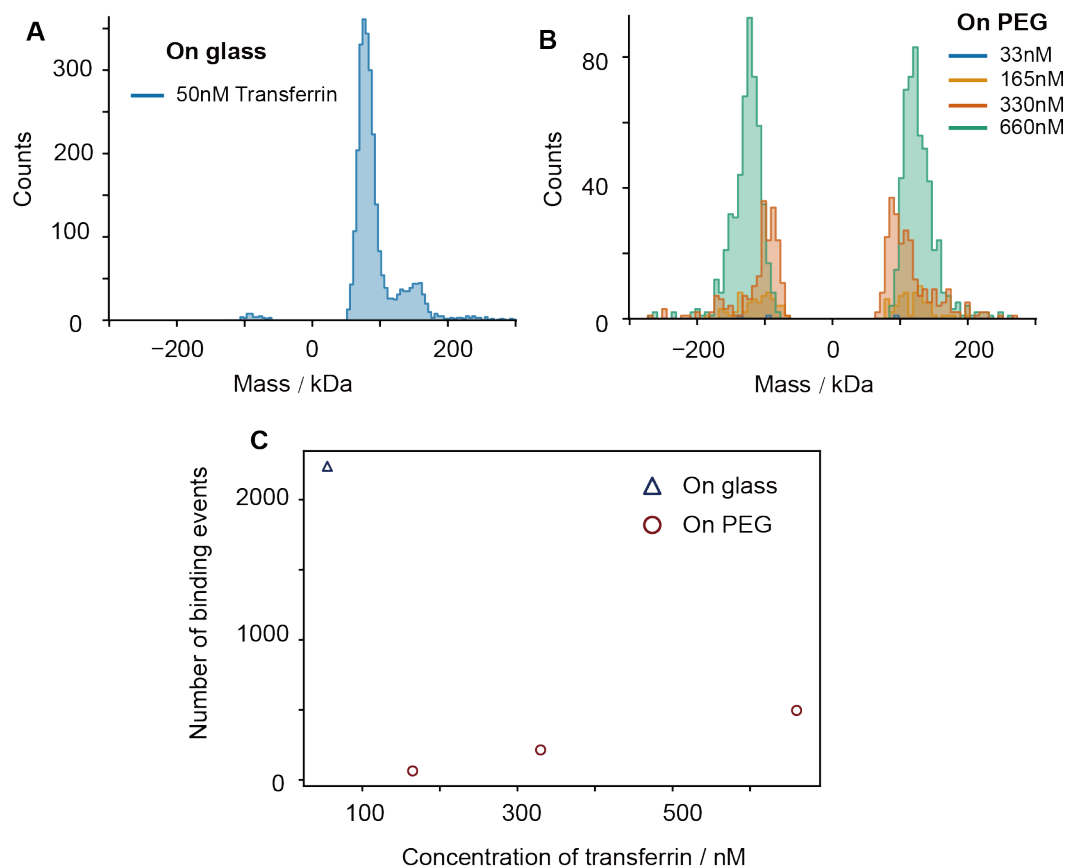


**Figure 6.5:** Successful PEG passivation largely reduces non-specific protein binding to the surface. (A) MP mass distribution of 50 nM transferrin measured on normal glass. (B) MP mass distributions of transferrin of different concentrations measured on PEGylated surfaces. (C) The number of binding events vs. concentration of transferrin on different surfaces.

### 6.3.2 Binding to 30% PEG-NTA Surfaces

Quantifying the his-tagged protein and the non-specific antibody immobilisation on 30% PEG-NTA surfaces, however, did not represent promising results for this particular conjugation strategy in MP measurements. Even though the passivation was successful and it largely reduced non-specific antibody binding as analysed by TIRFM (Figure 6.6B), specific binding of his-tagged MS1000 to NTA-Ni surfaces were not identified. In Figure 6.6A, no significant differences were found in his-tagged protein binding when comparing the binding events after loading Ni ion to the PEG-NTA surface with the ones found in the absence

of Ni ion.

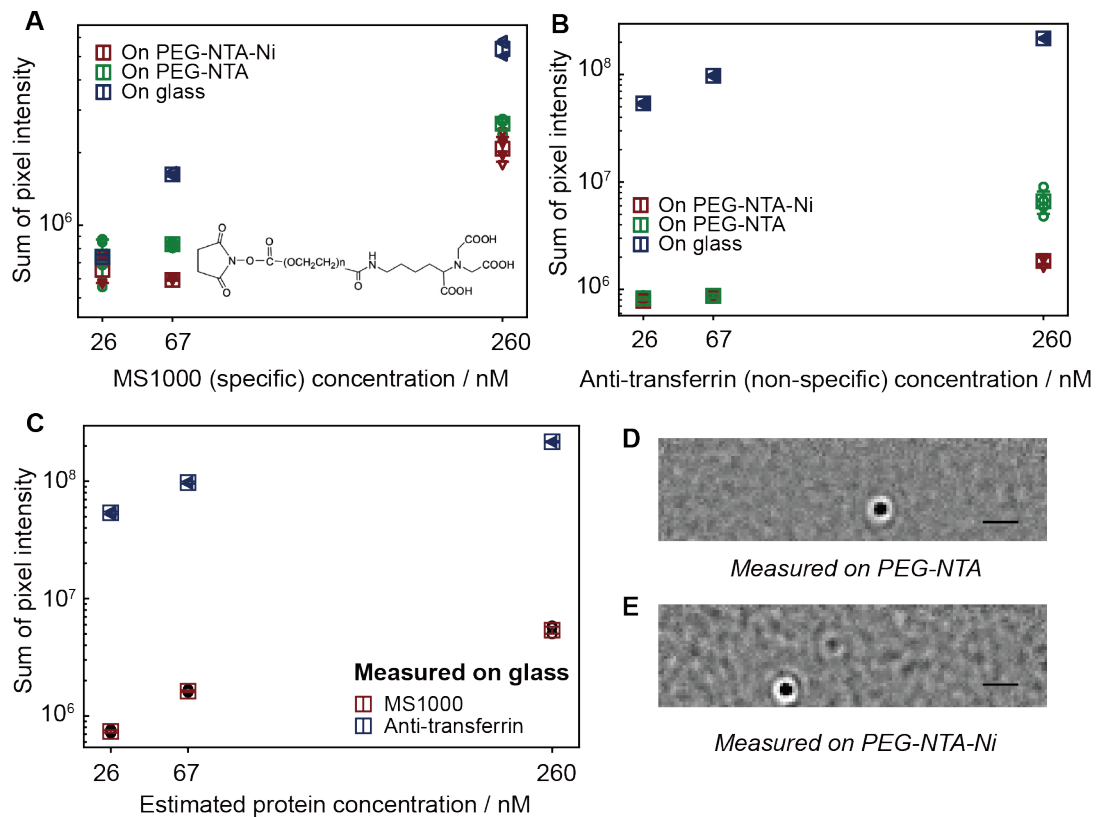


**Figure 6.6:** Quantifying protein immobilisation of his-tagged MS1000 (specific) and anti-transferrin (non-specific) on 30% PEG-NTA surfaces by TIRFM. **(A)** Pixel intensity shows the effectiveness of the immobilisation of his-tagged MS1000 on normal glass, PEG-NTA and PEG-NTA-Ni surfaces. The inset shows the molecular structure of the NHS-PEG-NTA used in the PEGylation process. **(B)** Pixel intensity show the effectiveness of the immobilisation of anti-transferrin on different surfaces. **(C)** Low labelling efficiency of the MS1000 resulted in much lower actual concentration when compared to labelled anti-transferrin. **(D)**, **(E)** Ratiometric images of his-tagged MS1000 on PEG-NTA and PEG-NTA-Ni surfaces. The slightly stronger binding of protein to the surface with  $\text{Ni}^{2+}$  is observed. Scale bars: 1  $\mu\text{m}$ .

Several reasons can be considered to explain ineffective specific binding. First of all, the NHS-PEG-NTA (Figure 6.6A inset) used in this PEGylation process had a much shorter half-life in water compared with the mPEG-SVA used for passivation. A much faster hydrolysis of the NHS-PEG-NTA during the second step of PEGylation procedure could lead to unsuccessful attachment of PEG-NTA to the glass surface. Secondly, the low labelling efficiency of the

MS1000 resulted in a much lower actual concentration than expected, as one could infer when comparing to the pixel intensities obtained by measuring the anti-transferrin labelled in the same way (Figure 6.6C). One of the most likely reason was the low affinity between mono-NTA and his-tags. As the previous literature has already suggested a low affinity ( $K_D \sim 10 \mu\text{M}$ ) for mono-NTA derivatives, it is difficult to immobilise his-tagged protein at nanomolar concentration to the PEG-NTA surface, especially in the case where the actual protein concentration was even smaller than the calculated one.

Despite the fact that TIRFM results showed almost no interaction between the NTA-Ni conjugation with the his-tagged protein, MP images could still provide information about the existence of the association between NTA-Ni group and histidine. When comparing the image of his-tagged MS1000 on PEG-NTA-Ni surface (Figure 6.6E) with the one on PEG-NTA surface without Ni (Figure 6.6D), the weak interaction of the protein with the surface in the presence of Ni ion was noticed. A slightly stronger interaction was detected on the PEG-NTA surface loaded with Ni ion. However, due to the low affinity, these signals still could not be quantified by MP. In any case, the affinity of mono-NTA with histidine is insufficient for current MP measurements, which are mostly performed in the nanomolar concentration range. NTA derivatives with higher multivalency should be used in the MP assays to achieve tight specific binding.

### 6.3.3 Robust Binding of Streptavidin to 10% Biotin-PEG Surfaces

Biotin-PEGylation, on the other hand, has proven to be a versatile biological assay with a robust interaction between biotin and streptavidin. Measuring streptavidin and anti-transferrin of different concentrations on both glass and PEG surfaces showed similar sums of pixel intensities among the two

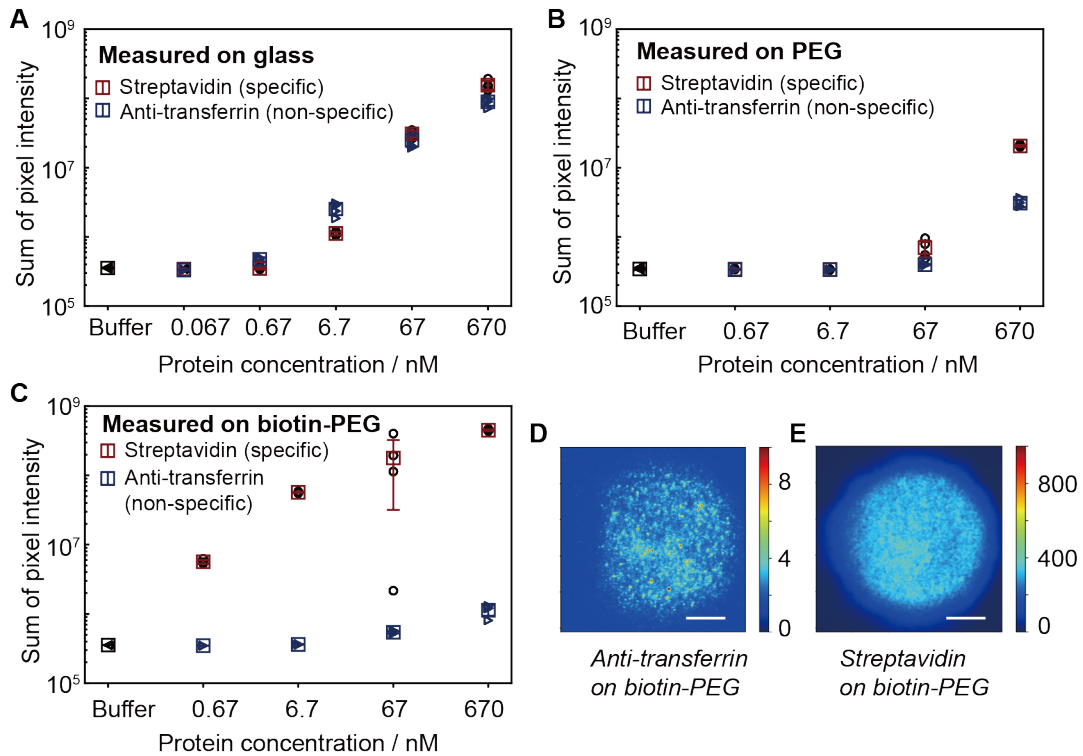


**Figure 6.7:** Robust specific binding of streptavidin to 10% biotin-PEG surfaces measured by TIRFM. (A), (B), (C) Streptavidin and anti-transferrin of different concentrations immobilised on normal glass, PEG surfaces and biotin-PEG surfaces. Pixel intensity shows the effectiveness of protein immobilisation. Streptavidin (specific) shows much higher binding affinity towards 10% biotin-PEG surfaces than anti-transferrin (non-specific). (D), (E) TIRFM images of 6.7 nM anti-transferrin and streptavidin measured on biotin-PEG surfaces. Streptavidin has 2 orders of magnitude higher affinity than that of anti-transferrin. Scale bars: 5  $\mu\text{m}$ .

proteins, with much fewer immobilised events on PEG surface compared with the ones on glass (Figure 6.7A, B). Whilst in the case of measuring proteins on biotin-PEG surfaces, a clear difference between the binding of streptavidin and the binding of anti-transferrin was observed (Figure 6.7C). While the sum of pixel intensity showed a slow increase when increasing the concentration of anti-transferrin, a significant enhancement in the intensity was found for streptavidin immobilisation on biotin-PEG surface. At 6.7 nM and 67 nM, streptavidin had much higher binding affinity than that of anti-transferrin, on the order of 2 orders of magnitude (Figure 6.7C, D, E). Also, tighter binding of streptavidin to biotin-PEG surface compared with regular glass was observed

(Figure 6.7A, C). The TIRFM results have established a good foundation for this conjugation strategy to be utilised in MP measurements, with a potential to measure a mixture of streptavidin with non-specific protein, even at a relative concentration ratio of 1:100.

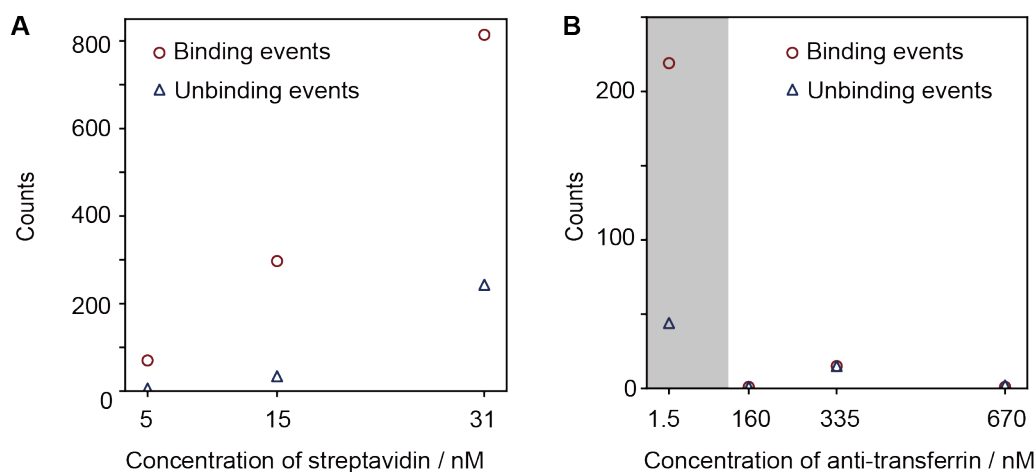


**Figure 6.8:** Specificity of 10% biotin-PEG surfaces measured by MP. **(A)** The number of binding and unbinding events of streptavidin at different concentrations on biotin-PEG surfaces. **(B)** The number of binding and unbinding events of anti-transferrin at different concentrations on both normal glass and biotin-PEG surfaces. The grey area shows the result of 1.5 nM of anti-transferrin measured on glass.

Quantifying the landing events of streptavidin and anti-transferrin on biotin-PEG surfaces by MP again proved the robust surface functionalisation for specificity. Less than 20 binding events of anti-transferrin were observed on biotin-PEG surfaces for concentrations as high as 670 nM in 2-minute movies, while measuring 50 nM anti-transferrin on glass resulted in more than 200 binding events (Figure 6.8B). Meanwhile, even at concentration as low as 5 nM, there were already 70 binding events of streptavidin on biotin-PEG surfaces (Figure 6.8A). The number of binding events of streptavidin on biotin-PEG surfaces quantified by MP have a linear dependency on the protein concentration, as expected for a single molecule experiment. However, there were also more unbinding events at high concentrations, which could be explained by surface saturation. The MP results prove the ability of the

10% biotin-PEG surface to identify rare protein which specifically binds to the surface even at a fairly low concentration in a mixture.

#### 6.3.4 Specific Binding by PEG-biotin-Streptavidin-<sup>BT</sup> tris-NTA

The low intrinsic affinity of the Ni-NTA complex to the his-tag demonstrated in Section 6.3.2 showed the need to include multiple NTA moieties in the conjugation system. Tris-NTA is mostly available as amino-groups or biotin conjugates. Because of the high-affinity, selective recognition of biotin by streptavidin, and the multivalent nature of streptavidin, we developed a sandwich-type assay via a biotin-streptavidin-biotin (BSB) bridge to adopt tris-NTA at the end of the surface, to achieve reversible binding of his-tagged protein with high affinity. By calculation, a gasket of 3 mm in diameter with 10 mg/ml 5000 Da biotin-PEG on the surface should comprise  $10^{11}$  biotin molecules, which should be able to bind approximately 50 nM of streptavidin in a 15  $\mu$ l solution. Thus, before loading the 1  $\mu$ M biotinylated tris-NTA to the surface, 50 nM of streptavidin was immobilised on the 10 % biotin-PEG surface to allow subsequent surface functionalisation via Ni ion activation.

Evidence given by TIRF measurements showed that the specificity for his-tagged protein might exist, whereas the differences in the affinities of his-tagged protein and non-tagged protein to the surfaces were relatively small. For 13 nM his-tagged MS1000 and 13 nM anti-transferrin measured on biotin-NTA-Ni surfaces, the sum of pixel intensity for MS1000 was only 3.4 times larger than that of the anti-transferrin (Figure 6.9A). However, it is worth noticing that even on the biotin-NTA surface without the loading of Ni ion, there were still variations between the binding of the two proteins. A slight increase in the intensity of MS1000 binding after adding Ni<sup>2+</sup> to the biotin-NTA surface was noticed (Figure 6.9A, D, E), but this increased behavior was not consistent

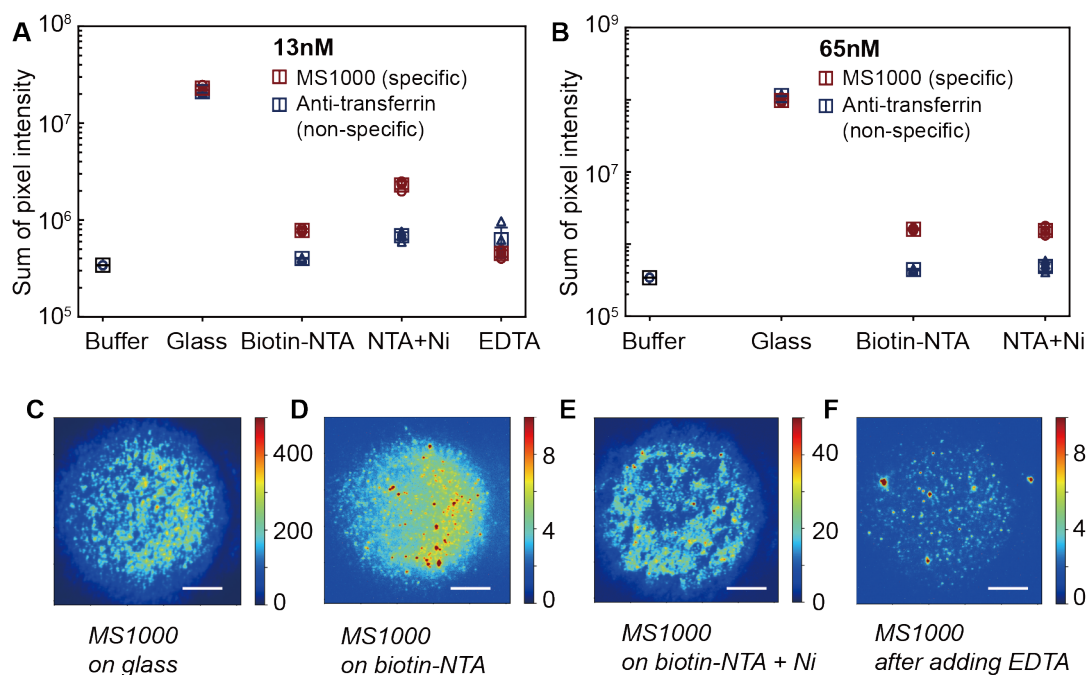


**Figure 6.9:** Specificity of PEG-biotin-Streptavidin-<sup>BT</sup> tris-NTA surfaces measured by TIRFM. (A), (B) Comparison of 13 nM and 65 nM his-tagged MS1000 (specific) and anti-transferrin (non-specific) immobilised on different surfaces, including unmodified glass, biotin-NTA surfaces, biotin-NTA-Ni surfaces and biotin-NTA-Ni surfaces after adding 500mM EDTA. (C), (D), (E), (F) TIRFM images of 13nM his-tagged MS1000 immobilised on different surfaces. Scale bars: 5  $\mu$ m.

when repeating the same process using 65 nM of MS1000 (Figure 6.9B). Adding 500 mM EDTA solution to the biotin-NTA-Ni conjugation successfully eluted the his-tagged protein from the surface via the removal of the nickel (Figure 6.9A, F), which, in other words, showed the successful association between tris-NTA and his-tags.

These results have shown the potential of this sandwich-type assay for specificity through the BSB bridge and tris-NTA group, yet further optimisation on the assay development should be explored to achieve higher affinity of his-tagged proteins with the functionalised surface.

## 6.4 Conclusion and Outlook

In this chapter, we introduced various PEG passivation strategies as tools for controlling specific binding while preventing the non-specific binding of biomolecules. By validation with MP and TIRFM, successful surface passivation with significant reduction of non-specific binding was obtained. For PEG-(mono)NTA surface, low affinity between mono-NTA and his tags led to poor immobilisation. In contrast, robust results showed the strong non-covalent binding of streptavidin and biotin, indicating the potential of this type of surface to be used to bind other biotin-tagged molecules. Conjugating the  $^{BT}$  tris-NTA to the PEG-biotin surface enabled the surface to specifically bind his-tagged protein to some extent. However, the difference in the affinity of tagged and untagged protein to the surface was too small to draw reliable conclusion that the functionalisation with  $^{BT}$  tris-NTA was successful.

To develop a suitable reversible landing assay for MP, further experiments should look into the optimisation of PEG-BSB-NTA surface, including the concentration of streptavidin immobilised on the biotin-PEG surface, the incubation time of each substrate, etc. Besides, one should continue to explore alternative routes to immobilising molecules on PEG surfaces. For example, tris-NTA amine can be linked to PEG through a maleimide reaction. Also, instead of employing NTA for reversible binding, recruiting antibodies on the surface could be another option to capture protein of interest.<sup>185,186</sup> Given the capability to measure low-abundance protein in a mixture, mass photometry can overcome its limitation on sample purity, and thus enable measurements of weakly-bound complexes which would have fallen apart during a regular purification.

Despite the advantage of adopting the PEG passivation to measure low-abundance biomolecules on the surface, the major drawback of the current

conjugation approach is the low binding affinities for specific proteins. Although applying other PEGylation protocols might ultimately achieve solid immobilisation of low-nanomolar proteins, the conjugation methods which require multiple steps and several-days' preparation would make MP measurements labour intensive. It is still desirable at the moment to maintain the valuable benefits that distinguish MP from other bioanalytical techniques, especially the requirement of minimal amounts of sample as well as the rapid and simple workflow. Therefore, this chapter was ended prematurely

Alternatively, combined with dynamic MP which successfully tracks proteins on lipid bilayers<sup>68</sup>, the NTA-Ni-histidine and streptavidin-biotin conjugations can be employed to develop pull-down assay on the bilayer instead of normal glass. As the bilayer surface is much denser than the PEGylated surface, it can immobilise protein at much higher concentration, with less concerns for low affinities. Given dynamic MP's capability to monitor individual complex for 10s of seconds at ms temporal resolution, coupled with the future pull down assay developed to bind specific species (tagged with his or biotin) for as long as 24 hours, one should be able to study one complex at a time to elucidate assembly and function of multimeric biological machine, such as cohesin and its interactions with DNA.

# Chapter 7

## Summary and Outlook

### 7.1 Summary

Until now, a major goal of the work using iSCAT and MP has been around the technical developments of the microscope, or its applications surrounding various proteins. This work, on the other hand, has proven single molecule mass photometry to be an extremely powerful tool for studying DNA as well as its interactions with proteins, also with the potential to be utilised in investigating the kinetics and dynamics beyond biomolecules.

Beginning with visualising the crystallisation events of the metal halide and metal-organic framework by a home-built iSCAT and a commercial mass photometer, we demonstrate the capability of iSCAT and MP to detect early stages of nucleation, to investigate thin film formation on glass surface and to study subsequent crystal growth.

Built on the solid understanding in the underlying mechanism and fundamental operation of iSCAT and MP, we then set out to investigate to which degree the capabilities of MP to proteins translate to DNA. Using a dsDNA ladder, we find a linear relationship between the number of bases per molecule and the associated imaging contrast for up to 1200 bp, enabling us to quantify dsDNA length with up to 2 bp accuracy. Also, The ability to count individual molecules directly measures relative concentrations in complex mixtures with-

out need for separation. In combination with similar capabilities for ssDNA and polypeptides, our results illustrate the potential of mass photometry to provide quantitative insights on DNA, and its interactions with proteins.

We next move to investigate MP's ability to quantify DNA-protein interactions and DNA-associated protein assemblies. By using mass photometry to quantify the key interactions responsible for cohesin assembly, DNA binding, and their modulations by ATP binding and hydrolysis, we identify two important DNA binding modules in cohesin, both associated with one HEAT subunit and one SMC head domain. The DNA affinities of these two modules (STAG1-head and NIPBL-head) are modulated by ATP hydrolysis, which points towards a mechanism for loop extrusion based on sequential hold and release of DNA mediated by STAG1 and NIPBL.

The increasing complexity of the biological system to be measured by MP has suggested the needs for employing surface functionalisation and surface passivation to control the binding and unbinding of biomolecules. While the low affinity between mono-NTA and his tags has led to poor immobilisation of specific proteins on the surface, robust results have showed the potential of the biotin-streptavidin conjugation to be used as a bridge to recruit <sup>BT</sup>tris-NTA for his-tagged protein bindings. Even though the current results have not provided sufficient evidence for successful conjugation, this work still suggests the potential for MP to explore new methods based on surface chemistry for studying biomolecules.

## 7.2 Outlook

Many questions remain to be answered in *chapter 3*. The consistency of surface structure should be determined by further experiments to understand whether they are crystalline or not. Improvements within the setup can be made to study

NPLIN from time zero. For future experiments on studying the crystallisation of (ZIF)-8 and (ZIF)-L, modifications of the glass surface, better control of the organic solvent, measurements with larger FOV and longer timescales might help to provide more detailed information during thin film formation and the latter stage of crystal growth.

In *chapter 4*, we focus here on small DNA molecules ( $< 1000$  bp), but there is extensive scope for expanding our approach towards much larger objects, such as DNA origami, and towards RNA as the other class of nucleic acids. Also, it is unclear at this stage to which extent the errors in basepair accuracy are real. This accuracy is generally subject to molecular polarisability, and thus factors such as the level of GC content, whether DNA is nicked, supercoiled, or circular, as well as effects due to variations in secondary structure could cause errors. In-depth study is required for encompassing a much broader set of samples. Still, we believe that this study will eventually become the original work in the context of quantitative single molecule nucleic acid science based on light scattering, and sets the stage for many exciting advances in the future including a universal approach to studying DNA-protein interactions, dynamic studies of nucleic acid-templated assembly or ultrasensitive analytical approaches more broadly.

To validate the proposed model for DNA loop extrusion by cohesin in *chapter 5*, further experiments on several aspects are needed. One should look into whether the DNA loading is consistent with different salt concentrations and different DNA shapes to prove topological DNA binding. Also, a more detailed analysis should be conducted to examine the interactions between each ATPase head domains as well as the hinge domain, and the HEAT subunits of STAG1 and NIPBL. Notwithstanding the open questions remaining to be answered, dynamic and kinetic information obtained by MP can be combined

together with previous biochemical and structural studies to provide fresh insights into the mechanism for loop extrusion by SMC complexes.

The work set out in *chapter 6* is only the first step of MP to employ surface passivation. A better optimisation of the NTA-his tags association via the biotin-streptavidin-biotin bridge will ultimately allow MP to measure low-abundance proteins of interest in a mixture without pre-purification, and even to quantify low-affinity interactions. Alternatively, combined with dynamic MP, one would be able to elucidate assembly and function of complex multimeric macro-machines.

The different aspects of DNA-related systems explored throughout this work demonstrate the potential of MP to be a universal tool to probe more biophysical systems. By overcoming the remaining challenges laid out in each chapter, one can probe the biophysics of DNA and its interactions with proteins at single molecule level with unprecedented resolution.

# References

- [1] D. Gordon, J. Huddleston, M. J. Chaisson, C. M. Hill, Z. N. Kronenberg, K. M. Munson, M. Malig, A. Raja, I. Fiddes, L. W. Hillier *et al.*, Long-read sequence assembly of the gorilla genome, *Science*, 2016, **352**, aae0344.
- [2] T. Ha, A. G. Kozlov and T. M. Lohman, Single-Molecule Views of Protein Movement on Single-Stranded DNA, *Annual Review of Biophysics*, 2012, **41**, 295–319.
- [3] G. Young, N. Hundt, D. Cole, A. Fineberg, J. Andrecka, A. Tyler, A. Olerinyova, A. Ansari, E. G. Marklund, M. P. Collier *et al.*, Quantitative mass imaging of single biological macromolecules, *Science*, 2018, **360**, 423–427.
- [4] F. Soltermann, E. D. Foley, V. Pagnoni, M. Galpin, J. L. Benesch, P. Kukura and W. B. Struwe, Quantifying protein–protein interactions by molecular counting with mass photometry, *Angewandte Chemie*, 2020, **132**, 10866–10871.
- [5] D. Wu and G. Piszczek, Measuring the affinity of protein-protein interactions on a single-molecule level by mass photometry, *Analytical biochemistry*, 2020, **592**, 113575.
- [6] D. Dulin, J. Lipfert, M. C. Moolman and N. H. Dekker, Studying ge-

- conomic processes at the single-molecule level: introducing the tools and applications, *Nature Reviews Genetics*, 2013, **14**, 9–22.
- [7] K. Frykholm, L. K. Nyberg and F. Westerlund, Exploring DNA–protein interactions on the single DNA molecule level using nanofluidic tools, *Integrative Biology*, 2017, **9**, 650–661.
- [8] A. Candelli, G. J. Wuite and E. J. Peterman, Combining optical trapping, fluorescence microscopy and micro-fluidics for single molecule studies of DNA–protein interactions, *Physical Chemistry Chemical Physics*, 2011, **13**, 7263–7272.
- [9] K. R. Chaurasiya, T. Paramanathan, M. J. McCauley and M. C. Williams, Biophysical characterization of DNA binding from single molecule force measurements, *Physics of life reviews*, 2010, **7**, 299–341.
- [10] E. Nordhoff, F. Kirpekar and P. Roepstorff, Mass spectrometry of nucleic acids, *Mass Spectrometry Reviews*, 1996, **15**, 67–138.
- [11] Y. L. Lyubchenko, A. A. Gall and L. S. Shlyakhtenko, in *Electron Microscopy*, Springer, 2014, pp. 367–384.
- [12] J. R. Moffitt, Y. R. Chemla, S. B. Smith and C. Bustamante, Recent advances in optical tweezers, *Annu. Rev. Biochem.*, 2008, **77**, 205–228.
- [13] J. TEISSIE, J.-F. TOCANNE and A. BAUDRAS, A Fluorescence Approach of the Determination of Translational Diffusion Coefficients of Lipids in Phospholipid Monolayer at the Air-Water Interface, *European Journal of Biochemistry*, 1978, **83**, 77–85.
- [14] A. I. Iliev, S. Ganesan, G. Bunt and F. S. Wouters, Removal of pattern-breaking sequences in microtubule binding repeats produces instantaneous

- 
- tau aggregation and toxicity, *Journal of Biological Chemistry*, 2006, **281**, 37195–37204.
- [15] J. O. Arroyo, J. Andrecka, Y. Takagi, J. R. Sellers and P. Kukura, Label-Free, All-Optical Detection, Imaging and Nanometric Tracking of Single Proteins, *Biophysical Journal*, 2014, **106**, 194a.
- [16] M. Piliarik and V. Sandoghdar, Direct optical sensing of single unlabelled proteins and super-resolution imaging of their binding sites, *Nature communications*, 2014, **5**, 1–8.
- [17] P. Kukura, H. Ewers, C. Müller, A. Renn, A. Helenius and V. Sandoghdar, High-speed nanoscopic tracking of the position and orientation of a single virus, *Nature methods*, 2009, **6**, 923–927.
- [18] G. Young and P. Kukura, Interferometric Scattering Microscopy, *Annual Review of Physical Chemistry*, 2019, **70**, 301–322.
- [19] D. Cole, G. Young, A. Weigel, A. Sebesta and P. Kukura, Label-free single-molecule imaging with numerical-aperture-shaped interferometric scattering microscopy, *ACS photonics*, 2017, **4**, 211–216.
- [20] G. G. Stokes, XXX. On the change of refrangibility of light, *Philosophical transactions of the Royal Society of London*, 1852, 463–562.
- [21] W. Fisher, W. Partridge Jr, C. Dees and E. Wachter, Simultaneous two-photon activation of type-I photodynamic therapy agents, *Photochemistry and photobiology*, 1997, **66**, 141–155.
- [22] S. Shashkova and M. C. Leake, Single-molecule fluorescence microscopy review: shedding new light on old problems, *Bioscience reports*, 2017, **37**, BSR20170031.

- [23] O. Heimstädt, Das fluoreszenzmikroskop, *Z Wiss Mikrosk*, 1911, **28**, 330–337.
- [24] H. Blom and J. Widengren, Stimulated emission depletion microscopy, *Chemical reviews*, 2017, **117**, 7377–7427.
- [25] H. Lehmann, *Das Luminszenz-Mikroskop: seine Grundlagen und seine Anwendungen*, 1913.
- [26] D. Axelrod, N. L. Thompson and T. P. Burghardt, Total internal reflection fluorescent microscopy, *Journal of microscopy*, 1983, **129**, 19–28.
- [27] K. N. Fish, Total internal reflection fluorescence (TIRF) microscopy, *Current protocols in cytometry*, 2009, **50**, 12–18.
- [28] N. A. Tanner, J. J. Loparo and A. M. van Oijen, Visualizing single-molecule DNA replication with fluorescence microscopy, *JoVE (Journal of Visualized Experiments)*, 2009, e1529.
- [29] A. J. Bonham, T. Neumann, M. Tirrell and N. O. Reich, Tracking transcription factor complexes on DNA using total internal reflectance fluorescence protein binding microarrays, *Nucleic acids research*, 2009, **37**, e94–e94.
- [30] C. D. Hughes, M. Simons, C. E. Mackenzie, B. Van Houten and N. M. Kad, Single molecule techniques in DNA repair: a primer, *DNA repair*, 2014, **20**, 2–13.
- [31] S. A. Hussain, An introduction to fluorescence resonance energy transfer (FRET), *arXiv preprint arXiv:0908.1815*, 2009.
- [32] T. Förster, Transfer mechanisms of electronic excitation energy, *Radiation Research Supplement*, 1960, 326–339.

- 
- [33] L. Stryer and R. P. Haugland, Energy transfer: a spectroscopic ruler., *Proceedings of the National Academy of Sciences of the United States of America*, 1967, **58**, 719.
- [34] J. A. Broussard, B. Rappaz, D. J. Webb and C. M. Brown, Fluorescence resonance energy transfer microscopy as demonstrated by measuring the activation of the serine/threonine kinase Akt, *Nature protocols*, 2013, **8**, 265.
- [35] M. Dyla, J. L. Andersen, M. Kjaergaard, V. Birkedal, D. S. Terry, R. B. Altman, S. C. Blanchard, P. Nissen and C. R. Knudsen, Engineering a prototypic P-type ATPase *Listeria monocytogenes* Ca<sup>2+</sup>-ATPase 1 for single-molecule FRET studies, *Bioconjugate chemistry*, 2016, **27**, 2176–2187.
- [36] C. Fijen, A. M. Silva, A. Hochkoeppler and J. Hohlbein, A single-molecule FRET sensor for monitoring DNA synthesis in real time, *Physical Chemistry Chemical Physics*, 2017, **19**, 4222–4230.
- [37] M. Renz, Fluorescence microscopy—A historical and technical perspective, *Cytometry Part A*, 2013, **83**, 767–779.
- [38] R. Alford, H. M. Simpson, J. Duberman, G. C. Hill, M. Ogawa, C. Regino, H. Kobayashi and P. L. Choyke, Toxicity of organic fluorophores used in molecular imaging: literature review, *Molecular imaging*, 2009, **8**, 7290–2009.
- [39] L. C. Zanetti-Domingues, C. J. Tynan, D. J. Rolfe, D. T. Clarke and M. Martin-Fernandez, Hydrophobic fluorescent probes introduce artifacts into single molecule tracking experiments due to non-specific binding, *PloS one*, 2013, **8**, e74200.

- [40] J. Ortega-Arroyo and P. Kukura, Interferometric scattering microscopy (iSCAT): new frontiers in ultrafast and ultrasensitive optical microscopy, *Physical Chemistry Chemical Physics*, 2012, **14**, 15625–15636.
- [41] A. A. Deniz, S. Mukhopadhyay and E. A. Lemke, Single-molecule biophysics: at the interface of biology, physics and chemistry, *Journal of the Royal Society Interface*, 2008, **5**, 15–45.
- [42] S. H. Gage, Modern dark-field microscopy and the history of its development, *Transactions of the American Microscopical Society*, 1920, **39**, 95–141.
- [43] P. Kukura, M. Celebrano, A. Renn and V. Sandoghdar, Imaging a single quantum dot when it is dark, *Nano letters*, 2009, **9**, 926–929.
- [44] M. Martin-Fernandez, C. Tynan and S. Webb, A ‘pocket guide’ to total internal reflection fluorescence, *Journal of microscopy*, 2013, **252**, 16–22.
- [45] X. Meng, A. Sonn-Segev, A. Schumacher, D. Cole, G. Young, S. Thorpe, R. W. Style, E. R. Dufresne and P. Kukura, Micromirror total internal reflection microscopy for high-performance single particle tracking at interfaces, *arXiv preprint arXiv:2103.09738*, 2021.
- [46] T. Wriedt, Mie theory: a review, *The Mie Theory*, 2012, 53–71.
- [47] P. Kulkarni, P. A. Baron and K. Willeke, *Aerosol measurement: principles, techniques, and applications*, John Wiley & Sons, 2011.
- [48] V. Amendola, R. Pilot, M. Frasconi, O. M. Marago and M. A. Iatì, Surface plasmon resonance in gold nanoparticles: a review, *Journal of Physics: Condensed Matter*, 2017, **29**, 203002.

- 
- [49] Y. Yang, S. Zhong, K. Wang and J. Huang, Gold nanoparticle based fluorescent oligonucleotide probes for imaging and therapy in living systems, *Analyst*, 2019, **144**, 1052–1072.
- [50] H. Ueno, S. Nishikawa, R. Iino, K. V. Tabata, S. Sakakihara, T. Yanagida and H. Noji, Simple dark-field microscopy with nanometer spatial precision and microsecond temporal resolution, *Biophysical journal*, 2010, **98**, 2014–2023.
- [51] C. P. Toseland, Fluorescent labeling and modification of proteins, *Journal of chemical biology*, 2013, **6**, 85–95.
- [52] L. Priest, J. S. Peters and P. Kukura, Scattering-based Light Microscopy: From Metal Nanoparticles to Single Proteins, *Chemical Reviews*, 2021, **121**, 11937–11970.
- [53] A. Curtis, The mechanism of adhesion of cells to glass A study by interference reflection microscopy, *Journal of Cell biology*, 1964, **20**, 199–215.
- [54] J. Ploem, Reflection-contrast microscopy as a tool for investigation of the attachment of living cells to a glass surface, *Mononuclear phagocytes in immunity, infection and pathology*, 1975, 405–421.
- [55] E. Atılgan and B. Övryn, Reflectivity and topography of cells grown on glass-coverslips measured with phase-shifted laser feedback interference microscopy, *Biomedical optics express*, 2011, **2**, 2417–2437.
- [56] G. Wiegand, K. R. Neumaier and E. Sackmann, Microinterferometry: three-dimensional reconstruction of surface microtopography for thin-film and wetting studies by reflection interference contrast microscopy (RICM), *Applied optics*, 1998, **37**, 6892–6905.

- [57] J. Rädler and E. Sackmann, Imaging optical thicknesses and separation distances of phospholipid vesicles at solid surfaces, *Journal de Physique II*, 1993, **3**, 727–748.
- [58] J. O. Arroyo, D. Cole and P. Kukura, Interferometric scattering microscopy and its combination with single-molecule fluorescence imaging, *Nature protocols*, 2016, **11**, 617–633.
- [59] M. A. Lieb, J. M. Zavislan and L. Novotny, Single-molecule orientations determined by direct emission pattern imaging, *JOSA B*, 2004, **21**, 1210–1215.
- [60] X. Brokmann, L. Coolen, J.-P. Hermier and M. Dahan, Emission properties of single CdSe/ZnS quantum dots close to a dielectric interface, *Chemical Physics*, 2005, **318**, 91–98.
- [61] A. Weigel, A. Sebesta and P. Kukura, Dark field microspectroscopy with single molecule fluorescence sensitivity, *ACS photonics*, 2014, **1**, 848–856.
- [62] A. Olerinyova, A. Sonn-Segev, J. Gault, C. Eichmann, J. Schimpf, A. H. Kopf, L. S. Rudden, D. Ashkinadze, R. Bomba, L. Frey *et al.*, Mass photometry of membrane proteins, *Chem*, 2021, **7**, 224–236.
- [63] M. A. Lebedeva, E. Palmieri, P. Kukura and S. P. Fletcher, Emergence and rearrangement of dynamic supramolecular aggregates visualized by interferometric scattering microscopy, *ACS nano*, 2020, **14**, 11160–11168.
- [64] A. Fineberg, T. Surrey and P. Kukura, Quantifying the Monomer–Dimer Equilibrium of Tubulin with Mass Photometry, *Journal of molecular biology*, 2020, **432**, 6168–6172.

- 
- [65] A. P. Torres-Ocampo, C. Özden, A. Hommer, A. Gardella, E. Lapinskas, A. Samkutty, E. Esposito, S. C. Garman and M. M. Stratton, Characterization of CaMKII $\alpha$  holoenzyme stability, *Protein Science*, 2020, **29**, 1524–1534.
- [66] A. R. Carvajal, I. Grishkovskaya, C. G. Diaz, A. Vogel, A. Sonn-Segev, M. S. Kushwah, K. Schodl, L. Deszcz, Z. Orban-Nemeth, S. Sakamoto *et al.*, The linear ubiquitin chain assembly complex (LUBAC) generates heterotypic ubiquitin chains, *Elife*, 2021, **10**, e60660.
- [67] R. F. Garmann, A. M. Goldfain and V. N. Manoharan, Measurements of the self-assembly kinetics of individual viral capsids around their RNA genome, *Proceedings of the National Academy of Sciences*, 2019, **116**, 22485–22490.
- [68] E. D. Foley, M. S. Kushwah, G. Young and P. Kukura, Mass photometry enables label-free tracking and mass measurement of single proteins on lipid bilayers, *Nature methods*, 2021, **18**, 1247–1252.
- [69] A. Sonn-Segev, K. Belacic, T. Bodrug, G. Young, R. T. VanderLinden, B. A. Schulman, J. Schimpf, T. Friedrich, P. V. Dip, T. U. Schwartz *et al.*, Quantifying the heterogeneity of macromolecular machines by mass photometry, *Nature communications*, 2020, **11**, 1–10.
- [70] K. Häußermann, G. Young, P. Kukura and H. Dietz, Dissecting FOXP2 oligomerization and DNA binding, *Angewandte Chemie*, 2019, **131**, 7744–7749.
- [71] A. B. Hickman, S. Kailasan, P. Genzor, A. D. Haase and F. Dyda, Casposase structure and the mechanistic link between DNA transposition and spacer acquisition by CRISPR-Cas, *Elife*, 2020, **9**, e50004.

- [72] J. Mullin, 8—Industrial techniques and equipment, *Crystallization, 4th ed.*; Mullin, JW, Ed.; Butterworth-Heinemann: Oxford, UK, 2001, 315–402.
- [73] P. R. ten Wolde and D. Frenkel, Enhancement of protein crystal nucleation by critical density fluctuations, *Science*, 1997, **277**, 1975–1978.
- [74] J. W. Mullin, *Crystallization*, Elsevier, 2001.
- [75] K. Fang, S. Arnold and B. Garetz, Nonphotochemical laser-induced nucleation in levitated supersaturated aqueous potassium chloride microdroplets, *Crystal Growth and Design*, 2014, **14**, 2685–2688.
- [76] B. Garetz, J. Aber, N. Goddard, R. Young and A. Myerson, Nonphotochemical, polarization-dependent, laser-induced nucleation in supersaturated aqueous urea solutions, *Physical review letters*, 1996, **77**, 3475.
- [77] A. K. E.-Z. El-Yafi and H. El-Zein, Technical crystallization for application in pharmaceutical material engineering, *asian journal of pharmaceutical sciences*, 2015, **10**, 283–291.
- [78] X. Sun, B. A. Garetz and A. S. Myerson, Polarization switching of crystal structure in the nonphotochemical laser-induced nucleation of supersaturated aqueous l-histidine, *Crystal Growth and Design*, 2008, **8**, 1720–1722.
- [79] I. S. Lee, J. M. Evans, D. Erdemir, A. Y. Lee, B. A. Garetz and A. S. Myerson, Nonphotochemical laser induced nucleation of hen egg white lysozyme crystals, *Crystal Growth and Design*, 2008, **8**, 4255–4261.
- [80] W. Li, A. Ikni, P. Scoufflaire, X. Shi, N. El Hassan, P. Gemeiner, J.-M. Gillet and A. Spasojevic-de Bire, Non-photochemical laser-induced

- nucleation of sulfathiazole in a water/ethanol mixture, *Crystal Growth & Design*, 2016, **16**, 2514–2526.
- [81] A. J. Alexander and P. J. Camp, Single pulse, single crystal laser-induced nucleation of potassium chloride, *Crystal Growth and Design*, 2009, **9**, 958–963.
- [82] M. R. Ward, G. W. Copeland and A. J. Alexander, Chiral hide-and-seek: Retention of enantiomorphism in laser-induced nucleation of molten sodium chlorate, *The Journal of chemical physics*, 2011, **135**, 114508.
- [83] M. R. Ward, S. McHugh and A. J. Alexander, Non-photochemical laser-induced nucleation of supercooled glacial acetic acid, *Physical Chemistry Chemical Physics*, 2012, **14**, 90–93.
- [84] M. R. Ward, I. Ballingall, M. L. Costen, K. G. McKendrick and A. J. Alexander, Nanosecond pulse width dependence of nonphotochemical laser-induced nucleation of potassium chloride, *Chemical Physics Letters*, 2009, **481**, 25–28.
- [85] H. Furukawa, K. E. Cordova, M. O’Keeffe and O. M. Yaghi, The chemistry and applications of metal-organic frameworks, *Science*, 2013, **341**, year.
- [86] V. Guillerm, D. Kim, J. F. Eubank, R. Luebke, X. Liu, K. Adil, M. S. Lah and M. Eddaoudi, A supermolecular building approach for the design and construction of metal–organic frameworks, *Chemical Society Reviews*, 2014, **43**, 6141–6172.
- [87] R. Chen, J. Yao, Q. Gu, S. Smeets, C. Baerlocher, H. Gu, D. Zhu, W. Morris, O. M. Yaghi and H. Wang, A two-dimensional zeolitic imidazolate framework with a cushion-shaped cavity for CO<sub>2</sub> adsorption, *Chemical Communications*, 2013, **49**, 9500–9502.

- [88] J. Cravillon, S. Munzer, S.-J. Lohmeier, A. Feldhoff, K. Huber and M. Wiebcke, Rapid room-temperature synthesis and characterization of nanocrystals of a prototypical zeolitic imidazolate framework, *Chemistry of Materials*, 2009, **21**, 1410–1412.
- [89] J. Cravillon, C. A. Schröder, R. Nayuk, J. Gummel, K. Huber and M. Wiebcke, Fast nucleation and growth of ZIF-8 nanocrystals monitored by time-resolved in situ small-angle and wide-angle X-ray scattering, *Angewandte Chemie International Edition*, 2011, **50**, 8067–8071.
- [90] H. H.-M. Yeung, A. F. Sapnik, F. Massingberd-Mundy, M. W. Gaultois, Y. Wu, D. A. Fraser, S. Henke, R. Pallach, N. Heidenreich, O. V. Magdysyuk *et al.*, Control of Metal–Organic Framework Crystallization by Metastable Intermediate Pre-equilibrium Species, *Angewandte Chemie International Edition*, 2019, **58**, 566–571.
- [91] H. P. Erickson, Size and shape of protein molecules at the nanometer level determined by sedimentation, gel filtration, and electron microscopy, *Biological procedures online*, 2009, **11**, 32–51.
- [92] P. Y. Moh, *Ph.D. thesis*, University of Manchester, 2012.
- [93] J. Cravillon, R. Nayuk, S. Springer, A. Feldhoff, K. Huber and M. Wiebcke, Controlling zeolitic imidazolate framework nano- and micro-crystal formation: insight into crystal growth by time-resolved in situ static light scattering, *Chemistry of Materials*, 2011, **23**, 2130–2141.
- [94] S. R. Venna, J. B. Jasinski and M. A. Carreon, Structural evolution of zeolitic imidazolate framework-8, *Journal of the American Chemical Society*, 2010, **132**, 18030–18033.

- 
- [95] Y. Li, W. B. Struwe and P. Kukura, Single molecule mass photometry of nucleic acids, *Nucleic Acids Research*, 2020, **48**, e97–e97.
- [96] J. W. Efcavitch and J. F. Thompson, Single-Molecule DNA Analysis, *Annual Review of Analytical Chemistry*, 2010, **3**, 109–128.
- [97] J. J. Kasianowicz, E. Brandin, D. Branton and D. W. Deamer, Characterization of individual polynucleotide molecules using a membrane channel, *Proceedings of the National Academy of Sciences*, 1996, **93**, 13770–13773.
- [98] O. Braha, B. Walker, S. Cheley, J. J. Kasianowicz, L. Song, J. E. Gouaux and H. Bayley, Designed protein pores as components for biosensors, *Chemistry & biology*, 1997, **4**, 497–505.
- [99] J. van Mameren, E. J. Peterman and G. J. Wuite, See me, feel me: methods to concurrently visualize and manipulate single DNA molecules and associated proteins, *Nucleic acids research*, 2008, **36**, 4381–4389.
- [100] M. D. Newton, B. J. Taylor, R. P. Driessen, L. Roos, N. Cvetesic, S. Allyjaun, B. Lenhard, M. E. Cuomo and D. S. Rueda, DNA stretching induces Cas9 off-target activity, *Nature structural & molecular biology*, 2019, **26**, 185–192.
- [101] C. E. Hall, Visualization of individual macromolecules with the electron microscope, *Proceedings of the National Academy of Sciences of the United States of America*, 1956, **42**, 801.
- [102] H. G. Hansma, K. Kasuya and E. Oroudjev, Atomic force microscopy imaging and pulling of nucleic acids, *Current opinion in structural biology*, 2004, **14**, 380–385.

- [103] Y. J. Wang, P. Rico-Lastres, A. Lezamiz, M. Mora, C. Solsona, G. Stirnermann and S. Garcia-Manyes, DNA binding induces a nanomechanical switch in the RRM1 domain of TDP-43, *The journal of physical chemistry letters*, 2018, **9**, 3800–3807.
- [104] S. Elhadj, G. Singh and R. F. Saraf, Optical properties of an immobilized DNA monolayer from 255 to 700 nm, *Langmuir*, 2004, **20**, 5539–5543.
- [105] L. Guemouri, J. Ogier and J. Ramsden, Optical properties of protein monolayers during assembly, *The Journal of chemical physics*, 1998, **109**, 3265–3268.
- [106] F. A. Engelhardt, F. Praetorius, C. H. Wachauf, G. Bruggenthies, F. Kohler, B. Kick, K. L. Kadletz, P. N. Pham, K. L. Behler, T. Gerling *et al.*, Custom-size, functional, and durable DNA origami with design-specific scaffolds, *ACS nano*, 2019, **13**, 5015–5027.
- [107] J. J. Schmied, M. Raab, C. Forthmann, E. Pibiri, B. Wünsch, T. Dammeyer and P. Tinnefeld, DNA origami-based standards for quantitative fluorescence microscopy, *Nature Protocols*, 2014, **9**, 1367–1391.
- [108] E. Stahl, T. G. Martin, F. Praetorius and H. Dietz, Facile and Scalable Preparation of Pure and Dense DNA Origami Solutions, *Angewandte Chemie International Edition*, 2014, **53**, 12735–12740.
- [109] M. P. Nicholas, L. Rao and A. Gennerich, in *Mitosis*, Springer, 2014, pp. 137–169.
- [110] L. Yang, R. Parton, G. Ball, Z. Qiu, A. H. Greenaway, I. Davis and W. Lu, An adaptive non-local means filter for denoising live-cell images and improving particle detection, *Journal of structural biology*, 2010, **172**, 233–243.

- 
- [111] G. L. Lukacs, P. Haggie, O. Seksek, D. Lechardeur, N. Freedman and A. Verkman, Size-dependent DNA mobility in cytoplasm and nucleus, *Journal of biological chemistry*, 2000, **275**, 1625–1629.
- [112] M. T. van Loenhout, M. De Grunt and C. Dekker, Dynamics of DNA supercoils, *Science*, 2012, **338**, 94–97.
- [113] V. V. Rybenkov, A. V. Vologodskii and N. R. Cozzarelli, The effect of ionic conditions on DNA helical repeat, effective diameter and free energy of supercoiling, *Nucleic acids research*, 1997, **25**, 1412–1418.
- [114] H. G. Hansma, I. Revenko, K. Kim and D. E. Laney, Atomic force microscopy of long and short double-stranded, single-stranded and triple-stranded nucleic acids, *Nucleic acids research*, 1996, **24**, 713–720.
- [115] J. Adamcik, D. V. Klinov, G. Witz, S. K. Sekatskii and G. Dietler, Observation of single-stranded DNA on mica and highly oriented pyrolytic graphite by atomic force microscopy, *FEBS letters*, 2006, **580**, 5671–5675.
- [116] E. Meshorer and T. Misteli, Chromatin in pluripotent embryonic stem cells and differentiation, *Nature reviews Molecular cell biology*, 2006, **7**, 540–546.
- [117] T. Kouzarides, Chromatin modifications and their function, *Cell*, 2007, **128**, 693–705.
- [118] K. Luger, A. W. Mäder, R. K. Richmond, D. F. Sargent and T. J. Richmond, Crystal structure of the nucleosome core particle at 2.8 Å resolution, *Nature*, 1997, **389**, 251–260.
- [119] R. D. Kornberg, Chromatin Structure: A Repeating Unit of Histones and

- DNA: Chromatin structure is based on a repeating unit of eight histone molecules and about 200 DNA base pairs., *Science*, 1974, **184**, 868–871.
- [120] E. P. Nora, B. R. Lajoie, E. G. Schulz, L. Giorgetti, I. Okamoto, N. Servant, T. Piolot, N. L. Van Berkum, J. Meisig, J. Sedat *et al.*, Spatial partitioning of the regulatory landscape of the X-inactivation centre, *Nature*, 2012, **485**, 381–385.
- [121] J. R. Dixon, S. Selvaraj, F. Yue, A. Kim, Y. Li, Y. Shen, M. Hu, J. S. Liu and B. Ren, Topological domains in mammalian genomes identified by analysis of chromatin interactions, *Nature*, 2012, **485**, 376–380.
- [122] Y. Zhang, X. Zhang, Z. Ba, Z. Liang, E. W. Dring, H. Hu, J. Lou, N. Kyritsis, J. Zurita, M. S. Shamim *et al.*, The fundamental role of chromatin loop extrusion in physiological V (D) J recombination, *Nature*, 2019, **573**, 600–604.
- [123] D. E. Anderson, A. Losada, H. P. Erickson and T. Hirano, Condensin and cohesin display different arm conformations with characteristic hinge angles, *The Journal of cell biology*, 2002, **156**, 419–424.
- [124] C. H. Haering, J. Löwe, A. Hochwagen and K. Nasmyth, Molecular architecture of SMC proteins and the yeast cohesin complex, *Molecular cell*, 2002, **9**, 773–788.
- [125] F. Uhlmann, SMC complexes: from DNA to chromosomes, *Nature reviews Molecular cell biology*, 2016, **17**, 399–412.
- [126] V. Guacci, D. Koshland and A. Strunnikov, A direct link between sister chromatid cohesion and chromosome condensation revealed through the analysis of MCD1 in *S. cerevisiae*, *Cell*, 1997, **91**, 47–57.

- 
- [127] C. Michaelis, R. Ciosk and K. Nasmyth, Cohesins: chromosomal proteins that prevent premature separation of sister chromatids, *Cell*, 1997, **91**, 35–45.
- [128] Y. Murayama, C. P. Samora, Y. Kurokawa, H. Iwasaki and F. Uhlmann, Establishment of DNA-DNA interactions by the cohesin ring, *Cell*, 2018, **172**, 465–477.
- [129] C. H. Haering, A.-M. Farcas, P. Arumugam, J. Metson and K. Nasmyth, The cohesin ring concatenates sister DNA molecules, *Nature*, 2008, **454**, 297–301.
- [130] I. F. Davidson, B. Bauer, D. Goetz, W. Tang, G. Wutz and J.-M. Peters, DNA loop extrusion by human cohesin, *Science*, 2019, **366**, 1338–1345.
- [131] Y. Kim, Z. Shi, H. Zhang, I. J. Finkelstein and H. Yu, Human cohesin compacts DNA by loop extrusion, *Science*, 2019, **366**, 1345–1349.
- [132] T. L. Higashi, P. Eickhoff, J. S. Sousa, J. Locke, A. Nans, H. R. Flynn, A. P. Snijders, G. Papageorgiou, N. O’reilly, Z. A. Chen *et al.*, A structure-based mechanism for DNA entry into the cohesin ring, *Molecular cell*, 2020, **79**, 917–933.
- [133] Y. Murayama and F. Uhlmann, DNA entry into and exit out of the cohesin ring by an interlocking gate mechanism, *Cell*, 2015, **163**, 1628–1640.
- [134] Y. Murayama and F. Uhlmann, Biochemical reconstitution of topological DNA binding by the cohesin ring, *Nature*, 2014, **505**, 367–371.
- [135] Z. Shi, H. Gao, X.-c. Bai and H. Yu, Cryo-EM structure of the human cohesin-NIPBL-DNA complex, *Science*, 2020, **368**, 1454–1459.

- [136] I. F. Davidson and J.-M. Peters, Genome folding through loop extrusion by SMC complexes, *Nature Reviews Molecular Cell Biology*, 2021, **22**, 445–464.
- [137] P. J. Huis in't Veld, F. Herzog, R. Ladurner, I. F. Davidson, S. Piric, E. Kreidl, V. Bhaskara, R. Aebersold and J.-M. Peters, Characterization of a DNA exit gate in the human cohesin ring, *Science*, 2014, **346**, 968–972.
- [138] M. T. Hons, P. J. Huis in't Veld, J. Kaesler, P. Rombaut, A. Schleiffer, F. Herzog, H. Stark and J.-M. Peters, Topology and structure of an engineered human cohesin complex bound to Pds5B, *Nature Communications*, 2016, **7**, 1–11.
- [139] F. Bürmann, B.-G. Lee, T. Than, L. Sinn, F. J. O'Reilly, S. Yatskevich, J. Rappsilber, B. Hu, K. Nasmyth and J. Löwe, A folded conformation of MukBEF and cohesin, *Nature structural & molecular biology*, 2019, **26**, 227–236.
- [140] B.-G. Lee, F. Merkel, M. Allegretti, M. Hassler, C. Cawood, L. Lecomte, F. J. O'Reilly, L. R. Sinn, P. Gutierrez-Escribano, M. Kschonsak *et al.*, Cryo-EM structures of holo condensin reveal a subunit flip-flop mechanism, *Nature structural & molecular biology*, 2020, **27**, 743–751.
- [141] T. L. Higashi and F. Uhlmann, SMC complexes: Lifting the lid on loop extrusion, *Current Opinion in Cell Biology*, 2022, **74**, 13–22.
- [142] G. Fudenberg, M. Imakaev, C. Lu, A. Goloborodko, N. Abdennur and L. A. Mirny, Formation of chromosomal domains by loop extrusion, *Cell reports*, 2016, **15**, 2038–2049.

- 
- [143] M. H. Nichols and V. G. Corces, A tethered-inchworm model of SMC DNA translocation, *Nature structural & molecular biology*, 2018, **25**, 906–910.
- [144] J.-S. Woo, J.-H. Lim, H.-C. Shin, M.-K. Suh, B. Ku, K.-H. Lee, K. Joo, H. Robinson, J. Lee, S.-Y. Park *et al.*, Structural studies of a bacterial condensin complex reveal ATP-dependent disruption of intersubunit interactions, *Cell*, 2009, **136**, 85–96.
- [145] A. Jo, S. Li, J. W. Shin, X. Zhao and Y. Cho, Structure basis for shaping the Nse4 protein by the Nse1 and Nse3 dimer within the Smc5/6 complex, *Journal of Molecular Biology*, 2021, **433**, 166910.
- [146] C. M. Farrell, A. T. Mackey, L. M. Klumpp and S. P. Gilbert, The role of ATP hydrolysis for kinesin processivity, *Journal of Biological Chemistry*, 2002, **277**, 17079–17087.
- [147] H. Schmidt, E. S. Gleave and A. P. Carter, Insights into dynein motor domain function from a 3.3-Å crystal structure, *Nature structural & molecular biology*, 2012, **19**, 492–497.
- [148] M. Ganji, I. A. Shaltiel, S. Bisht, E. Kim, A. Kalichava, C. H. Haering and C. Dekker, Real-time imaging of DNA loop extrusion by condensin, *Science*, 2018, **360**, 102–105.
- [149] H. L. Sweeney and E. L. Holzbaur, Motor proteins, *Cold Spring Harbor Perspectives in Biology*, 2018, **10**, a021931.
- [150] J.-K. Ryu, A. J. Katan, E. O. van der Sluis, T. Wisse, R. de Groot, C. H. Haering and C. Dekker, The condensin holocomplex cycles dynamically between open and collapsed states, *Nature Structural & Molecular Biology*, 2020, **27**, 1134–1141.

- [151] B. W. Bauer, I. F. Davidson, D. Canena, G. Wutz, W. Tang, G. Litos, S. Horn, P. Hinterdorfer and J.-M. Peters, Cohesin mediates DNA loop extrusion by a “swing and clamp” mechanism, *Cell*, 2021, **184**, 5448–5464.
- [152] T. L. Higashi, G. Pobegalov, M. Tang, M. I. Molodtsov and F. Uhlmann, A Brownian ratchet model for DNA loop extrusion by the cohesin complex, *Elife*, 2021, **10**, e67530.
- [153] P. Mayrhofer, M. Blaesen, M. Schleef and W. Jechlinger, Minicircle-DNA production by site specific recombination and protein–DNA interaction chromatography, *The Journal of Gene Medicine: A cross-disciplinary journal for research on the science of gene transfer and its clinical applications*, 2008, **10**, 1253–1269.
- [154] P. Mayrhofer, H. Jug, A. Štrancar, A. Di Paolo, L. Jost, A. Zimmermann and H. Redl, Coordinating the in vivo processes for minicircle production—a novel approach to large scale manufacturing, *bioRxiv*, 2018, 300236.
- [155] F. Weissmann and J.-M. Peters, in *Protein Complex Assembly*, Springer, 2018, pp. 329–343.
- [156] F. Weissmann, G. Petzold, R. VanderLinden, N. G. Brown, F. Lampert, S. Westermann, H. Stark, B. A. Schulman, J.-M. Peters *et al.*, biGBac enables rapid gene assembly for the expression of large multisubunit protein complexes, *Proceedings of the National Academy of Sciences*, 2016, **113**, E2564–E2569.
- [157] J. Lin, P. Countryman, H. Chen, H. Pan, Y. Fan, Y. Jiang, P. Kaur, W. Miao, G. Gurgel, C. You *et al.*, Functional interplay between SA1 and TRF1 in telomeric DNA binding and DNA–DNA pairing, *Nucleic acids research*, 2016, **44**, 6363–6376.

- 
- [158] Y. Kurokawa and Y. Murayama, DNA binding by the Mis4Scc2 loader promotes topological DNA entrapment by the cohesin ring, *Cell Reports*, 2020, **33**, 108357.
- [159] K. K. Bisht, Z. Daniloski and S. Smith, SA1 binds directly to DNA through its unique AT-hook to promote sister chromatid cohesion at telomeres, *Journal of cell science*, 2013, **126**, 3493–3503.
- [160] Y. Li, K. W. Muir, M. W. Bowler, J. Metz, C. H. Haering and D. Panne, Structural basis for Scc3-dependent cohesin recruitment to chromatin, *Elife*, 2018, **7**, e38356.
- [161] I. Rasnik, S. A. McKinney and T. Ha, Surfaces and orientations: much to FRET about?, *Accounts of chemical research*, 2005, **38**, 542–548.
- [162] R. Lamichhane, A. Solem, W. Black and D. Rueda, Single-molecule FRET of protein–nucleic acid and protein–protein complexes: surface passivation and immobilization, *Methods*, 2010, **52**, 192–200.
- [163] N. Di Fiori and A. Meller, Automated system for single molecule fluorescence measurements of surface-immobilized biomolecules, *JoVE (Journal of Visualized Experiments)*, 2009, e1542.
- [164] J. Helenius, G. Brouhard, Y. Kalaidzidis, S. Diez and J. Howard, The depolymerizing kinesin MCAK uses lattice diffusion to rapidly target microtubule ends, *Nature*, 2006, **441**, 115–119.
- [165] L. Shen, A. Guo and X. Zhu, Tween surfactants: adsorption, self-organization, and protein resistance, *Surface Science*, 2011, **605**, 494–499.
- [166] D. L. Elbert and J. A. Hubbell, Surface treatments of polymers for biocompatibility, *Annual Review of Materials Science*, 1996, **26**, 365–394.

- [167] I. J. Finkelstein and E. C. Greene, in *DNA Recombination*, Springer, 2011, pp. 447–461.
- [168] J. Groll and M. Moeller, Star polymer surface passivation for single-molecule detection, *Methods in enzymology*, 2010, **472**, 1–18.
- [169] J. Porath, J. Carlsson, I. Olsson and G. Belfrage, Metal chelate affinity chromatography, a new approach to protein fractionation, *Nature*, 1975, **258**, 598–599.
- [170] J. Nilsson, S. Ståhl, J. Lundeberg, M. Uhlén and P.-å. Nygren, Affinity fusion strategies for detection, purification, and immobilization of recombinant proteins, *Protein expression and purification*, 1997, **11**, 1–16.
- [171] S. Lata, M. Gavutis, R. Tampé and J. Piehler, Specific and stable fluorescence labeling of histidine-tagged proteins for dissecting multi-protein complex formation, *Journal of the American Chemical Society*, 2006, **128**, 2365–2372.
- [172] C. R. Goldsmith, J. Jaworski, M. Sheng and S. J. Lippard, Selective Labeling of Extracellular Proteins Containing Polyhistidine Sequences by a Fluorescein- Nitrilotriacetic Acid Conjugate, *Journal of the American Chemical Society*, 2006, **128**, 418–419.
- [173] F. Cheng, L. J. Gamble and D. G. Castner, XPS, TOF-SIMS, NEX-AFS, and SPR characterization of nitrilotriacetic acid-terminated self-assembled monolayers for controllable immobilization of proteins, *Analytical chemistry*, 2008, **80**, 2564–2573.
- [174] E. Kang, J.-W. Park, S. J. McClellan, J.-M. Kim, D. P. Holland, G. U. Lee, E. I. Franses, K. Park and D. H. Thompson, Specific adsorption

- of histidine-tagged proteins on silica surfaces modified with Ni<sup>2+</sup>/NTA-derivatized poly (ethylene glycol), *Langmuir*, 2007, **23**, 6281–6288.
- [175] S. Lata, A. Reichel, R. Brock, R. Tampé and J. Piehler, High-affinity adaptors for switchable recognition of histidine-tagged proteins, *Journal of the American Chemical Society*, 2005, **127**, 10205–10215.
- [176] Z. Huang, J. I. Park, D. S. Watson, P. Hwang and F. C. Szoka, Facile synthesis of multivalent nitrilotriacetic acid (NTA) and NTA conjugates for analytical and drug delivery applications, *Bioconjugate chemistry*, 2006, **17**, 1592–1600.
- [177] A. Reichel, D. Schaible, N. Al Furoukh, M. Cohen, G. Schreiber and J. Piehler, Noncovalent, site-specific biotinylation of histidine-tagged proteins, *Analytical chemistry*, 2007, **79**, 8590–8600.
- [178] Y. Li and H. Zhang, Binding of streptavidin to surface-attached biotin with different spacer thicknesses, *Journal of Wuhan University of Technology-Mater. Sci. Ed.*, 2015, **30**, 1304–1309.
- [179] N. George, H. Pick, H. Vogel, N. Johnsson and K. Johnsson, Specific labeling of cell surface proteins with chemically diverse compounds, *Journal of the American Chemical Society*, 2004, **126**, 8896–8897.
- [180] J. Yin, P. D. Straight, S. M. McLoughlin, Z. Zhou, A. J. Lin, D. E. Golan, N. L. Kelleher, R. Kolter and C. T. Walsh, Genetically encoded short peptide tag for versatile protein labeling by Sfp phosphopantetheinyl transferase, *Proceedings of the National Academy of Sciences*, 2005, **102**, 15815–15820.
- [181] A. Gust, A. Zander, A. Gietl, P. Holzmeister, S. Schulz, B. Lalkens, P. Tinnefeld and D. Grohmann, A starting point for fluorescence-based

- single-molecule measurements in biomolecular research, *Molecules*, 2014, **19**, 15824–15865.
- [182] Z. Zhang, S. R. Park, A. Pertsinidis and A. Revyakin, Cloud-point PEG glass surfaces for imaging of immobilized single molecules by total-internal-reflection microscopy, *Bio-protocol*, 2016, **6**, e1784–e1784.
- [183] T. Ha, I. Rasnik, W. Cheng, H. P. Babcock, G. H. Gauss, T. M. Lohman and S. Chu, Initiation and re-initiation of DNA unwinding by the Escherichia coli Rep helicase, *Nature*, 2002, **419**, 638–641.
- [184] S. D. Chandradoss, A. C. Haagsma, Y. K. Lee, J.-H. Hwang, J.-M. Nam and C. Joo, Surface passivation for single-molecule protein studies, *JoVE (Journal of Visualized Experiments)*, 2014, e50549.
- [185] A. Jain, R. Liu, Y. K. Xiang and T. Ha, Single-molecule pull-down for studying protein interactions, *Nature protocols*, 2012, **7**, 445–452.
- [186] A. Kenaan, K. Li, I. Barth, S. Johnson, J. Song and T. F. Krauss, Guided mode resonance sensor for the parallel detection of multiple protein biomarkers in human urine with high sensitivity, *Biosensors and Bioelectronics*, 2020, **153**, 112047.